Novel pneumatic circuit for the computational control of soft robots



Sihan Wang

St Edmund Hall

University of Oxford

A thesis submitted for the degree of

Doctor of Philosophy

Michaelmas 2023

Acknowledgements

In this section, I would like to express my sincere gratitude and appreciation to all the individuals who have contributed to the successful completion of my doctoral thesis: My supervisor Prof. Perla Maiolino, collaborators, colleagues, friends, and family. This journey would not have been so smooth and enjoyable without their unwavering support, guidance, and encouragement.

First and foremost, I extend my deepest appreciation to my supervisor, Prof. Perla Maiolino. I first met Perla during my PhD interview in the spring of 2020. She then offered me the excellent opportunity to come to Oxford for an exciting DPhil. Perla has always been a great lab leader, a wise mentor, a reliable collaborator, and a kind friend since then. The atmosphere in Perla's lab has always been supportive and heart-warming. The great diversity in research topics across the lab significantly widens my academic horizons. I'm particularly grateful to Perla for giving me the independence in choosing my research direction throughout the whole DPhil while still providing reliable support whenever needed to prevent me from losing the way. As a collaborator, Perla's dedication and rigour to academic work set me a great example and have been instrumental in shaping my work style. Lastly, as a friend, I would also thank Perla for supporting and encouraging me through those hard times.

During this DPhil journey, I've been having the fortune to collaborate with some of the best minds in the world. Their intellectual contributions, discussions, and feedback have greatly enhanced my research quality. I want to specifically thank Dr Alessandro Albini, Dr Liang He, and Dr Peizhi Zhang. It has always been a great pleasure and honour to work with them all.

I also would like to thank the friends that I have made in Oxford. I want to especially mention Wenye Ouyang, Oliver Shorthose, Jianeng Wang, Shaohong Zhong, Fengyu Zhong, Ningzhe Hou and Giammarco Caroleo, for all the help and support both in and out of the lab. I also want to thank my friends in the Oxford University Company of Archers, especially Yang Pei, Ecaterina Pogorenni, Callum Henfrey, Eleonore Cossade, Adam Bates and Samuel Walby, for all those great times we spent together in the archery range.

I would like to extend my deepest gratitude and heartfelt appreciation to my girlfriend, Chenying Liu, for being an unwavering source of support, love, and encouragement throughout my DPhil journey. I am deeply grateful for your

love, and I look forward to the adventures that lie ahead, hand in hand, as we continue to navigate life together.

My sincere gratitude goes to my family, especially my parents Xiaoming Wang and Xin Gao. Their unwavering support, understanding, and love have been a huge motivation for me. Their sacrifices and encouragement during this journey have been truly invaluable, and I am forever grateful for their presence in my life.

Finally, I acknowledge the funding source that made my research at Oxford possible: China Scholarship Council-University of Oxford Scholarships. Their support has not only eased the financial burden of my research but also allowed me to focus on my studies and pursue my academic goals without distraction.

Abstract

Soft robots are of significant research interest in recent decades due to their adaptability to unstructured environments and safe interaction with humans. Soft pneumatic robots, one of the most dominant subsets of soft robots, utilize the interaction between soft elastomeric materials and pressurized air to achieve desired functions. However, the systems currently used for signal computation and pneumatic regulation often make use of rigid valves, pumps, syringe drivers, microcontrollers et al. These bulky and non-integrable devices limit the performance of pneumatically-driven soft robots, carrying challenges for the robot to be miniaturized, untethered, and agile. This DPhil aims to develop pneumatic circuits that can be integrated into the soft robot bodies while performing both onboard computation and control.

This thesis presents our contributions towards the aforementioned objective step by step. Firstly, we designed a 3D-printable bistable valve with tunable behaviours for controlling soft pneumatic robots. As an integrable control device, the valve stores one bit of binary information without requiring a constant energy supply and correspondingly controls a pneumatic chamber. Secondly, in order to reduce the number of valves required to control multi-chamber soft robots, we introduced a modular approach to design multi-channel bistable valves based on the previous work. Thirdly, in order to achieve continuous pressure modulation with integrable devices, we designed a soft proportional valve, utilizing the continuous deformation of Magnetorheological Elastomer (MRE) under magnetic flux. Apart from the analogue activation manner, this design also ensures a fast response time, operating at a time scale of tens of milliseconds, much shorter than the mechanical response time of most soft pneumatic actuators. Fourthly, to achieve onboard proportional control of multi-chamber soft robots, we developed an MRE valve array with an embedded cooling chamber. Physical experiments showed that our MRE valve array ensured the independence and accuracy of each valve unit within it, with a significantly lowered temperature of 73.9 ^{o}C under 5 minutes of operation. Lastly, we developed an open-source software toolbox supporting the design of integrable pneumatic logic circuits to enhance their accessibility and performance. The toolbox comes with a graphical user interface (GUI) to take users' desired logic functions in the form of a truth table and a set of 2D space constraints related to the available

space onboard the robot. It then schedules the pneumatic circuit which performs the desired computation within the space constraints and produces a 3D-printable CAD file that can be fabricated and used directly.

The work presented in this thesis enables the community to simplify the process of integrating control devices into soft pneumatic robots, thereby paving the way for a new generation of fully untethered and autonomous soft robots.

Contents

List of Figures **ix**

List of Abbreviations **xvii**

1 Introduction **1**

1.1 Motivation 1
1.2 Objective and our contributions 2
1.3 Outline 5
1.4 Publications 8
1.4.1 Papers directly related to my DPhil topic 8
1.4.2 Other papers contributed 8

2 Literature Review **9**

2.1 Soft pneumatic robots 9
2.1.1 Soft pneumatic actuators 10
2.1.2 Traditional pneumatic control hardware 12
2.1.3 Applications 13
2.2 Integrating devices onboard soft robots for computation and control 15
2.2.1 Microfluidics 15
2.2.2 Silicone tube-kinking valves 17
2.2.3 3D printed fluidic circuitry 19
2.2.4 Handcrafted control devices for soft robots 21
2.2.5 Magnetorheological fluid valves 23
2.2.6 Fluidic control based on dielectric actuators 25
2.2.7 Approaches without mimicking electronics 26
2.2.8 Summary: a comparison between our work and the literature 28
2.3 Key enabling technologies 29
2.3.1 Polyjet Multi-material 3D printing 29
2.3.2 Magnetorheological Elastomer (MRE) 31

3 3D Printed Bistable Valve with Tunable Characteristics 33
3.1 Problem . . . 33
3.2 Objective . . . 34
3.3 Key contributions . . . 34
3.4 Summary of the results . . . 35
3.5 Contributed Paper . . . 35
3.6 Supporting Information . . . 44
3.6.1 Supporting Video . . . 44
3.6.2 CAD files . . . 44

4 Modular 3D-printed Multi-channel Valves 45
4.1 Problem . . . 45
4.2 Objective . . . 46
4.3 Key contributions . . . 46
4.4 Summary of results . . . 47
4.5 Contributed Paper . . . 47
4.6 Supporting Information . . . 56
4.6.1 Supporting Video . . . 56
4.6.2 CAD files . . . 56

5 Magnetorheological elastomer (MRE) based proportional valves 57
5.1 Problem . . . 57
5.2 Objective . . . 58
5.3 Key Contributions and Limitations . . . 58
5.4 Contributed Paper . . . 59
5.5 Supporting Information . . . 76
5.5.1 Some supporting videos . . . 76
5.5.2 Dimensions of the MRE valves. . . . 76
5.5.3 Dimensions of the four different MRE geometries investigated. 76

6 Magnetorheological-Elastomer-Based Valve Array 77
6.1 Problem . . . 77
6.2 Objective . . . 79
6.3 Methodology . . . 79
6.3.1 MRE valve unit and its scaling up . . . 79
6.3.2 Magnetic interference . . . 80
6.3.3 Heat Dissipation . . . 82
6.3.4 Design and fabrication of MRE valve array . . . 85
6.4 Results . . . 87
6.4.1 Magnetic interference . . . 87

6.4.2 Heat dissipation . . . 89
6.4.3 Demonstration . . . 91
6.5 Conclusions and future work . . . 93
6.6 Supporting Information . . . 93
6.6.1 Supporting Video . . . 93
6.6.2 Simulation settings when investigating magnetic interference 94
6.6.3 Simulation settings when investigating thermal dissipation . 95

7 A Design Automation Toolbox for Pneumatic Circuits 98
7.1 Problem . . . 98
7.2 Objective . . . 100
7.3 Methodology . . . 101
7.3.1 Modular design of the logic gates . . . 101
7.3.2 Design automation of the pneumatic computational circuit . 102
7.4 Results . . . 108
7.4.1 Validity of the design automation algorithm . . . 108
7.4.2 Validity of the physical output . . . 109
7.4.3 Reliability of the printed pneumatic circuit . . . 113
7.5 Conclusions and future work . . . 115
7.6 Supporting Information . . . 116
7.6.1 Supporting videos . . . 116
7.6.2 Installation of the toolbox software . . . 116
7.6.3 Userguide of the design automation toolbox . . . 117
7.6.4 Detailed setup when 3D-printing the pneumatic circuit . . . 118
7.6.5 Algorithm for finding the simplest circuit schematic . . . 119
7.6.6 Algorithm for finding all valid logic gate layout . . . 120

8 Conclusions 121

Appendices

A List of Supporting Videos 126

B Copyright Permissions 128
B.1 Permissions of IEEE papers . . . 129
B.2 Permissions of other papers . . . 130

C Theoretical Model for the Bistability of the 3D Printed Valve 131

D PID Controllers for MRE Valves 134

References 136

List of Figures

2.1 Different PneuNet actuators. **(A)** shows a classic bending actuator, reproduced from [3]. **(B)** shows a bellow bending actuator, reproduced from [16]. **(C)** shows a PneuNet extending actuator, reproduced from [17]. **(D)** shows the Honeycomb Pneumatic Networks, reproduced from [15]. 10

2.2 Different fibre-reinforced actuators. **(A)** shows a McKibben artificial muscle, reproduced from [15]. **(B)** shows a fibre-reinforced bending actuator, reproduced from [20]. **(C)** shows a set of fibre-reinforced actuators whose movements are controlled by fibre orientations, reproduced from [21]. 11

2.3 Traditional pneumatic control systems **(A)** shows a typical pump-tank-valve system, reproduced from [26]. **(B)** shows a typical syringe pump system, reproduced from [33]. 13

2.4 Octo-bot, controlled by an onboard microfluidic circuit, reproduced from [58]. **(A)** shows an overview of the body of Octo-bot, fabricated through a combination of soft lithography, moulding, and 3D printing. **(B)** shows the working principle of its limb movements. A microfluidic oscillator is used to periodically release the onboard monopropellant fuel into the reaction chambers. The fuel then decomposes, yielding pressurized gas which flows downstream to the pneumatic actuators and the vent orifices concurrently. 16

2.5 A microfluidics library for controlling soft robots, reproduced from [59]. In this example, the four fluid-driven actuators are controlled by a shift register and a de-multiplexer. 17

2.6 Silicone-casted valves based on tube-kinking mechanism, reproduced from [65]. **(A)** shows the basic structure of the silicone bistable valve. The silicone membrane in the middle is driven by the pressure difference between the two chambers P_M. The status of this membrane determines whether the top or the bottom tubes are kinked, therefore affecting the ON/OFF status of the air channels. **(B) - (D)** show the different configurations of the valves when being used as NOT, OR and AND gates, respectively. 18

2.7 3D printed fluidic circuitry for controlling soft robots, reproduced from [69]. **(A)** shows the basic structure and working principle of the 3D-printed pneumatic diode. When pressure is applied in the unfavoured direction, the piston will be lifted and sealed the air channel, preventing the airflow. **(B)** shows the basic structure and working principle of the 3D-printed normally "OFF" transistor. Without a gate pressure, the piston naturally seals the air channel under pressure, preventing airflow. Once sufficient gate pressure is applied, the membrane lifts the piston, allowing airflow. **(C)** shows the basic structure and working principle of the 3D-printed normally "ON" transistor. Without a gate pressure, the piston stays low and allows airflow. Once a sufficient gate pressure is engaged, the piston will be lifted and block the airflow. **(D)** presents a 3D-printed turtle with oscillatory movements controlled by the integrated pneumatic circuit. **(E)** presents a 3D-printed robotic hand pressing a game controller, also controlled by the integrated pneumatic circuit. . . . 20

2.8 Handcrafted pneumatic control devices for controlling soft robots. **(A)** shows the basic structure of the tube-balloon logic devices, reproduced from [73]. **(B)** shows their working principles. The input pneumatic signal is applied to a balloon. Once a HIGH signal is engaged, the balloon bends a bendable straw. The bent straw then kinks the tube and therefore blocks the airflow. Such a single unit behaves like a NOT gate. **(C)** shows the structure of the piston actuator developed by [74]. A piston (red) with a bistable TPU membrane (green) is driven by the input pneumatic signal, travelling in parallel with the external tube. **(D)** presents the structure of the pneumatic switch developed by [74]. Tubes are attached to a central rod (yellow) which travels along the axial direction within the external tube. The rod kinks and blocks the top or bottom air channel depending on its current position. Combining the piston actuator **(C)** and the pneumatic switch **(D)** brings a programmable pneumatic valve enabling signal computation. **(E)** presents a teleoperated soft robotic hand controlled by the programmable soft valves, reproduced from [74]. **(F)** presents a soft crawler with a gripper onboard, also controlled by the programmable soft valves, reproduced from [74]. . 22

2.9 Magnetorheological (MR) fluid-based flow control for soft robots, reproduced from [75]. **(A)** shows the working principle of the MR fluid regulation. Without the magnetic field, the iron particles in the water remain free and the MR fluid has its lowest viscosity. Once activated, the externally applied magnetic flux aligns the iron particles inside into long chains, therefore significantly increasing the fluidic resistance of the MR fluid. **(B)** shows the schematic when implementing proportional control on a soft actuator via MR fluid regulation. Constant pressure MR fluid is supplied to the upstream of the actuator, while the downstream of the actuator is connected to the atmosphere via an electro-permanent magnet regulating the MR fluids. The magnetic field strength generated by the EPM determines the downstream fluidic resistance, therefore controlling the fluidic pressure inside the actuator. **(C)** presents the experimental result, showing that the mechanism can achieve continuous pressure modulation of a soft actuator. 24

2.10 Integrable pneumatic control devices for soft robots without mimicking electronics. **(A)** shows a fluidic relaxation oscillator, reproduced by [80]. Three slits are cut on a soft hysteretic membrane, meeting at its apex. The membrane, therefore, blocks the airflow before the snap-through and allows the airflow after the snap-through. This allows the device to convert a continuous inflow into a pulsatile activation. **(B)** presents the concept of leveraging actuator mechanics, fluid dynamics, and structural bistability to control the actuation sequence of multiple soft actuators via a single pneumatic input, reproduced from [81]. The pneumatic actuators are all connected in series with slender tubes for an enhanced viscosity effect. Each actuator here comes with its structural bistability. With careful modelling, such a system can reach and maintain any desired state combination of the soft actuators through a single pneumatic input provided by the syringe pump. 27

2.11 Polyjet Multi-material 3D printing. **(A)** shows the working principle of this fabrication technique. This fabrication technique has been used to develop various soft robots, such as **(B)** a soft crawler [86], **(C)** a soft gripper [87], **(D)** a soft hand [88], and **(E)** a soft robotic arm [34]. 29

2.12 Magnetorheological Elastomer (MRE) and its applications in soft robotics. **(A)** shows the fabrication process of the majority of MRE, reproduced from [97]. **(B)** shows a microfluidic platform with pumps and mixers based on MRE, reproduced from [98]. **(C)** presents a soft actuator based on MRE, reproduced by [99]. **(D)** presents the structure and working principle of a soft grasper based on MRE, reproduced by [100]. 31

5.1 The detailed dimensions of the MRE valves are presented. h and w are the adjustable parameters investigated in this work. 76

5.2 The detailed dimensions of the four different MRE geometries investigated. 76

6.1 MRE valve single unit structure. **A** shows the photo of a single MRE-based proportional valve. An MRE membrane is located on top of an electromagnet embedded in silicone. The controlled air channel is located between the coil and the MRE membrane. **B** shows the cross-section view of the MRE valve. By applying an electric current to the electromagnet, a magnetic field whose strength is controllable can be generated. This magnetic field deforms the MRE membrane, therefore achieving a continuous flowrate or pressure modulation in the controlled air channel. 79

6.2 Simulation results of the magnetic field with different magnetic pole arrangements and MRE valve spacing. **(A)** shows the magnetic field distribution at the plane of the air channel with different valve spacing and pole arrangements. **(B)** shows the magnetic flux density along the air channel of the valve when the neighboring unit has the same pole arrangement. **(C)** shows the magnetic flux density along the air channel of the valve when the neighboring unit has the opposite pole arrangement. The benchmark (magnetic flux density of a single valve without interference) is shown in both **(B)** and **(C)** for ease of comparison. The enlargement views of the curve peaks are also given for clarity. 81

6.3 Thermal analysis on the MRE valve array. **(A)** shows the measured and simulated temperature curve of a single MRE valve under different amounts of electric current. The measured data was obtained by attaching a temperature sensor to the surface of a single MRE valve, while the simulated data was obtained when the convective heat transfer coefficient was set to 9.2 W/m^2K. **(B)** shows the simulated temperature distribution of the MRE valve array without a cooling system over a period of 1500s. **(C)** presents the simulated temperature-time curve at the center of the MRE valve units when the array is without a cooling system. **(D)** shows the simulated temperature distribution of the MRE valve array with a cooling system over a period of 1500s. **(E)** presents the simulated temperature-time curve at the center of the MRE valve units when the array comes with the proposed cooling system. 83

6.4 Design and fabrication of the MRE valve array and its cooling system. **(A)** shows a photo of the MRE valve array and its cooling system. The yellow block shows the MRE valve array consisting of four MRE valve units. The cooling chamber of the MRE valve array is connected in a loop with a micropump and a cooling device (a fan, a radiator, two Peltier plates, and a water tank). Cooling water is driven by the micropump, bringing the heat generated by the MRE valve array to the cooling device, so that it maintains the valve array at a safe temperature. **(B)** shows the top and cross-sectional view of the MRE valve array. **(C)** to **(E)** shows the fabrication process of the MRE valve array. Firstly, a cooling belt with a rectangular internal chamber was fabricated. It was then placed together with four coils into a mold as shown in **(C)**. Next, the silicone is poured into the mold and covers the coils and the cooling belt, as shown in **(D)**. Finally, the MRE membrane is fabricated on top, and silicone tubes are attached, as shown in **(E)**. 86

6.5 Experimental results about the magnetic interference of the MRE valve array. **(A)** shows the measured magnetic flux density in the middle of two MRE valve units under different amounts of electric current and different pole arrangements. The magnetic field shows good linearity along with the current. **(B)** shows the measured flowrate through the valve channel under different amounts of electric current and pole arrangement. 88

6.6 Experimental results about the heat dissipation of the MRE valve array with and without a cooling system. **(A)** shows the temperature distribution of the MRE array with a cooling system every 10 seconds during the working phase. **(B)** shows the temperature distribution of the MRE array without the cooling system every 10 seconds during the working phase. **(C)** shows the temperature distribution of the MRE array with a cooling system every 60 seconds during the cooling phase. **(D)** shows the temperature distribution of the MRE array without the cooling system every 60 seconds during the cooling phase. 90

6.7 A four-chamber soft robot controlled by the MRE valve array. The structure of the robot is shown in **(A)**. It consists of four silicone-made PneuNet soft actuators. Each actuator is connected to an MRE valve unit in the array as shown in **(B)**. By activating and deactivating the valves, the soft robot exhibits different configurations. **(C)**-**(J)** shows the different configurations of the soft robot controlled by the MRE valve array, together with the pressure within each pneumatic actuator. 92

7.1 The user interface of the toolbox in MATLAB. The operation procedure is ordered here for clarity. ① indicates the region where users define the number of inputs and outputs of their desired computation. ② refers to the editable table where users define the truth table. ③ refers to the editable map where users specify the 2D space constraints of the pneumatic circuits. ④ and ⑤ refer to the buttons for planning the pneumatic circuit and saving the 3D printable CAD files, respectively. 101

7.2 **A** shows the structure and the working principle of a pneumatic NOT gate. **B** shows the structure and the working principle of a pneumatic AND gate. **C** shows the structure and the working principle of a pneumatic OR gate. The design of these gates has been influenced by and adapted from a prior work.[69] **D-F** shows the pressure-time curve of the three logic gates at their inputs and outputs. The response time of each logic gate under pneumatic inputs with different amplitudes is presented in **G-I**. 103

7.3 An overview of the pneumatic computation circuit design toolbox that converts the desired computation functions into a 3D-printing-ready CAD model directly. The toolbox enables rapid design and manufacture of the computational pneumatic circuits for a wide range of soft robots, with minimum manual work involved. 104

7.4 The detailed hardware structure of the computational circuit. A connection hub is used to connect all logic gates into the circuit. It includes some attachment ports for fitting with the logic gates on top, air channels in the middle, and a set of input/output ports that connects to the input and output pneumatic signal of the entire computation circuit. 107
7.5 Pneumatic circuits under different space constraints scheduled by the toolbox to achieve an XOR computation. **A** presents the user-input truth table taken by the toolbox. **B - D** present the different pneumatic circuits scheduled by the toolbox under different space constraints provided by users. The available workspace is indicated in white while the unavailable workspace is in gray. The color of each air channel indicates which layer it should be placed within. The larger red dots and green dots represent the inputs and outputs of the entire computational circuit, respectively. 109
7.6 Pneumatic circuits under different space constraints scheduled by the toolbox to achieve a 1:4 DEMUX computation. **A** presents the user-input truth table taken by the toolbox. **B - D** present the different pneumatic circuits scheduled by the toolbox under different space constraints provided by users. The available workspace is indicated in white while the unavailable workspace is in gray. The color of each air channel indicates which layer it should be placed within. The larger red dots and green dots represent the inputs and outputs of the entire computational circuit, respectively. 110
7.7 **A-C** represent the three different fabricated pneumatic circuits to achieve XOR computation, scheduled by the toolbox as previously to suit different space constraints. **D-F** present the pressure-time curve of each pneumatic circuit at their inputs and outputs, showing the correct implementation of the desired truth table. **G** presents the response time of each of the fabricated circuits. **H** presents the duration of the undesired “glitch" observed in each circuit. **I** represents the pressure amplitude of the “glitch" observed in each circuit. 111
7.8 **A-C** represent the three different fabricated pneumatic circuits to achieve the 1:4 de-multiplexer, scheduled by the toolbox as previously to suit different space constraints. **D-F** present the pressure-time curve of each pneumatic circuit at their inputs and outputs, showing the correct implementation of the desired truth table. **G** presents the response time of the four outputs measured from the different pneumatic circuits. 112

7.9 Results of the fatigue tests. **A** and **B** represent the long-term computation accuracy of the XOR and 1:4 DEMUX circuit, respectively. The tests were performed with different input signal durations to investigate the circuits' durability under different computation frequencies. Each data point in the plots refers to the number of correct computations within 100 cycles. 114

B.1 Permissions from IEEE for reusing figures for thesis, ... 129
B.2 Permissions for other papers via RightsLink 130

List of Abbreviations

2D . . . . . Two dimensional

3D . . . . . Three dimensional

MRE . . . . . Magnetorheological elastomer

CAD . . . . . Computer-aided design

IEEE . . . . . Institute of Electrical and Electronics Engineers

DPhil . . . . . Doctor of Philosophy

PneuNet . . . Pneumatic networks

PAM . . . . . Pneumatic artificial muscle

SMA . . . . . Shape memory alloy

EAP . . . . . Electro-active polymer

VR . . . . . Virtual reality

CFR . . . . . Conductive fluid receptor

ED . . . . . Electrofluidic diode

PWM . . . . . Pulse width modulation

TBL . . . . . Tube-balloon logic

MR . . . . . Magnetorheological

MRE . . . . . Magnetorheological elastomer

MRF . . . . . Magnetorheological fluid

EPM . . . . . Electropermanent magnet

DOF . . . . . Degree of freedom

UV . . . . . Ultraviolet

RMSE . . . . . Root-mean-squared error

RA-L . . . . . Robotics and Automation Letters

ICRA . . . . . International Conference on Robotics and Automation

STD . . . . . Standard deviation

DCV . . . . . Directional control valve

FE . . . . . Finite-element

FEA . . . . . Finite element analysis

FEM . . . . . Finite-element method

ISO . . . . . International Organization for Standardization

DAC . . . . . Digital-analogue converter

SPA . . . . . Soft pneumatic actuator

CIP . . . . . Carbonyl iron powder

SEM . . . . . Scanning electron microscope

PID . . . . . Proportional-integral-differential

LPM . . . . . Litre per minute

GUI . . . . . Graphical user interface

SOP . . . . . Sum of product

DEMUX . . . De-multiplexer

CoM . . . . . Centre of mass

1 Introduction

Contents

1.1 Motivation **1**
1.2 Objective and our contributions **2**
1.3 Outline **5**
1.4 Publications **8**
1.4.1 Papers directly related to my DPhil topic 8
1.4.2 Other papers contributed 8

1.1 Motivation

Soft pneumatic robots are of interest to an increasing number of researchers due to their compatibility in highly unstructured and dynamic environments [1, 2]. Unlike traditional robots whose structures are made with rigid links and joints, these types of soft robots are actuated based on the interaction between regulated air and soft elastomeric materials with high compliance. The mechanism brings various advantages including (i) low cost; (ii) flexible manufacture choices such as silicone casting [3], 3D printing [4, 5], and blow film extrusion [6]; (iii) safe human-robot interaction; (iv) adaptability to unknown environments or objects; and (v) ease of being bio-compatible or biodegradable [7]. These characteristics lead to numerous diverse designs of soft pneumatic robots, incorporating various

structures, materials, design principles, and applications. However, while the vast majority of research interests focus on the soft robot bodies, much less attention has been paid to their pneumatic control devices that regulate the driving pressure inside. Most existing soft pneumatic robots still require a conventional pneumatic system including electronic controllers, displacement pumps, rigid valves, syringe drivers, etc., to control the pressure within the robot. Using these externally tethered control devices sacrifices many benefits obtained by using soft materials. The system compliance is severely reduced since these devices have Young's modulus more than 10^5 higher than that of soft materials. The size/weight miniaturization is also hindered since the total size/weight of battery, driver, and solenoid valves is often higher than the soft robot itself. All these facts limit the robots' adaptability in practical applications. The problem is becoming progressively more pronounced as newer soft robots, which often feature a greater number of pneumatic actuators and degrees of freedom (DoFs) to enhance functionality, require an increased quantity of valves and pumps for control. In many cases, the weight and size of the conventional pneumatic system are larger than those of the robot itself, posing a significant obstacle to designing a new generation of untethered autonomous soft robots.

1.2 Objective and our contributions

The objective of this DPhil research is to develop integrable pneumatic circuits that enable both (i) computation and (ii) hardware control directly onboard soft robots through multi-material 3D printing or casting of smart elastomeric materials. The term "computation" in this context refers to the manipulation of pneumatic signals to achieve essential robotic functions such as information storage, programmable reflexes, and gait control. The term "hardware control" refers to regulating flowrate or pressure of air channels or pneumatic chambers with hardware devices. Achieving this objective allows soft roboticists to replace the existing hard, bulky pneumatic control systems, which is crucial for realizing a new generation of fully autonomous and untethered soft robots. To achieve this

objective, multiple research questions were identified and resolved. Below are the specific research questions and our solutions.

Q1. How can we integrate valves into the body of soft robots while ensuring energy efficiency and storing binary information?

Valves, as devices used to regulate airflow, are the most essential components for achieving onboard hardware control for soft robots. Embedding structural bistability into valves provides a feasible solution to the research question stated above. The bistability enables the valve to store one bit of binary information even after a power reset. It also helps the valve to more securely and efficiently regulate the air flow. These motivate researchers to develop a silicone-casted bistable valve for soft robots [8], though the complex and time-consuming fabrication process limits its broader application. Therefore, the first step of this DPhil is to develop an easy-to-manufacture bistable valve that can be seamlessly integrated into the soft robots. To address this research question, we developed a 3D-printed bistable valve whose characteristics can be accurately tuned by adjusting several design dimensions to suit different needs. The 3D-printed nature ensures the valve can be integrated into any 3D-printed soft robot with ease. Details of this work can be found in Chapter 3.

Q2. How can we decrease the number of valves required when controlling soft pneumatic robots with more DOF?

One limitation of our previous work, the 3D-printed bistable valve, is that one valve unit is only capable of controlling one air channel. This brings a highly bulky system when controlling soft pneumatic robots with multiple DOF since a large number of valves are required. To address this issue, we modified the previous design and introduced a set of modular 3D-printed multi-channel valves (3/2, 4/2, and 5/2 way valves) which retain the advantages of our previous work but can simultaneously control multiple pneumatic actuators. The multi-channel compatibility significantly decreases the number of units required for onboard pneumatic control, therefore reducing the system size, weight, response time, and energy consumption. Details of this work can be found in Chapter 4.

Q3. How can we use integrable hardware to achieve continuous pressure modulation on soft pneumatic robots?

The valves introduced by our previous works control soft pneumatic actuators in a digital ON/OFF manner due to their bistable structure. However, the ability to continuously alter the pressure or flowrate in an analogue manner provides advantages in various applications including human-robot interaction [9], adaptive grasping [10], soft pneumatic arm control [11] and so on. To answer this research question, we developed a novel proportional valve that exploits magnetorheological elastomer (MRE) to achieve proportional pressure/flowrate control, soft robot integrability, high durability and low cost. Details of this work can be found in Chapter 5. We further expanded the scope of the work by investigating how the MRE-based proportional valves can be packed into an array efficiently for controlling soft robots with multiple pneumatic actuators. The details about this MRE valve array can be found in Chapter 6.

Q4. How to achieve the migration from individual pneumatic devices to computational pneumatic circuits that can be directly used on soft robots?

Previous works conducted in this DPhil mainly focus on developing individual devices for onboard control of soft robots, while onboard computation still remains challenging. To provide a soft robot with an onboard pneumatic circuit for desired computation, one must first design the correct circuit schematic, identifying the minimally required components and their connections. The spatial layout of the circuit then needs to be carefully designed to fit within the limited space onboard the robot. Finally, manual piping is needed to physically join all the components together. This entire process heavily relies on human expertise, experience, and labour. It also introduces additional problems, such as redundant tubing and unreliable fittings, leading to unnecessary system delays and energy consumption. To address this problem, we leveraged the knowledge gained from the development of 3D-printed bistable valves and created an open-source software toolbox for the design automation of pneumatic circuits used in soft robots. By inputting a truth table and constrained workspace, the toolbox generates a 3D-printing-ready CAD

file of a pneumatic circuit with an optimized channel and logic gate layout. By replacing the extensive manual work involved, the toolbox enhances the accessibility of pneumatic circuits in soft robots and enables soft roboticists to create, test, and optimize untethered intelligent soft robots with less effort. Further details about this design automation toolbox can be found in Chapter 7.

1.3 Outline

This thesis is divided into eight chapters, including an introduction, a literature review, five main chapters presenting our scientific contributions, and a conclusion. The five main chapters are written in a hybrid format. Chapters 3,4 and 5 are written in the integrated format since each of the chapters corresponds to a published paper. In each of these chapters, we first present the target research questions and the objectives, followed by a summary of the key contributions of our work. Lastly, we attached the published paper, describing the technical details of the work. Chapters 6 and 7 are written in the conventional format since the corresponding papers are currently under review, and have not been published yet. In these two chapters, we use the conventional structure including the introduction, methodology, results and conclusion.

Chapter 1: Introduction

The motivation of the thesis is stated followed by a list of research questions identified and our contributions toward them. A publication list is attached as well.

Chapter 2: Literature Study

A detailed description of the state-of-art works in the following aspects: (1) soft pneumatic robots and their traditional pneumatic control hardware; (2) previous research works on developing integrable pneumatic devices for onboard computation and control of soft robots and; (3) two enabling technologies which are essential for the methodologies deployed in this DPhil: multi-material 3D printing and soft magnetic materials.

Chapter 3: 3D Printed Bistable Valve with Tunable Characteristics

Here we present a journal paper titled "Design and characterization of a 3D-printed pneumatically-driven bistable valve with tunable characteristics" published in *IEEE Robotics and Automation Letters (RA-L)*. The work is the first bistable valve (pneumatic memory device) in the community that exploits multi-material 3D printing technology and therefore significantly simplifies the fabrication and increases the design flexibility. The work has been presented in an oral session at the IEEE International Conference on Robotics and Automation in 2023, in London, UK.

Chapter 4: Modular 3D-printed Multi-channel Valves

Here we present a journal paper titled "A Modular Approach to Design Multi-channel Bistable Valves for Integrated Pneumatically-driven Soft Robots via 3D-printing" published in *IEEE Robotics and Automation Letters (RA-L)*. By introducing multi-channel compatibility into the 3D-printed bistable valve, the number of units required when controlling multi-chamber soft robots is significantly decreased. This lowers the system size/weight while reducing the energy consumed by the circuit. The work has been presented in an oral session at the IEEE International Conference on Robotics and Automation in 2022, in Philadelphia, USA.

Chapter 5: Magnetorheological elastomer (MRE) based proportional valves

Here we present a journal paper titled "A Magnetorheological Elastomer-Based Proportional Valve for Soft Pneumatic Actuators" published in *Advanced Intelligent Systems*. The work introduces a novel soft proportional valve design that applies MRE in controlling soft actuators, achieving continuous pressure modulation with high accuracy (mean error of 0.05 kPa) and fast response (<0.02s). The compliant nature of the MRE enables the valve to be easily integrated into any silicone-based soft robots.

Chapter 6: Magnetorheological-Elastomer-Based Valve Array

In this chapter, we discuss methods for packing multiple MRE-based proportional valves into a compact array, to broaden its application with multi-chamber soft robots. The two major challenges encountered are magnetic interference between valves and heat dissipation. Multiphysics FE simulations were used to find out the optimal valve spacing without interference and aid the design of an internal cooling channel. The resultant valve array design enables multiple valve units to work steadily without magnetic interference or overheating even under long-duration operation with high electric currents. The work is currently under review by the *Soft Robotics* journal.

Chapter 7: A Design Automation Toolbox for Pneumatic Circuits

This chapter describes our software toolbox for the design automation of pneumatic computation circuits, aiming to simplify the manual design, fabrication and assembly processes when applying them to controlling soft robots. Firstly, the hardware foundation of the pneumatic circuits, including three different logic gates, is presented. The detailed algorithms of the design automation toolbox are then discussed. The versatility of the design automation algorithm over different application scenarios has been physically tested with two different truth tables and six different workspaces. Finally, to demonstrate its capability, we utilised the toolbox to design a computational circuit that governs the movements of a soft robotic hand with four pneumatic actuators.

Chapter 8: Conclusions

In this chapter, we summarize the contributions made to the community, the lessons learned, and possible directions for future research.

1.4 Publications

1.4.1 Papers directly related to my DPhil topic

- Wang, S., He, L. and Maiolino, P., 2021. Design and characterization of a 3D-printed pneumatically-driven bistable valve with tunable characteristics. *IEEE Robotics and Automation Letters, 7*(1), pp.112-119.

- Wang, S., He, L. and Maiolino, P., 2022. A Modular Approach to Design Multi-channel Bistable Valves for Integrated Pneumatically-driven Soft Robots via 3D-printing. *IEEE Robotics and Automation Letters, 7*(2), pp.3412-3418.

- Wang, S., He, L., Albini, A., Zhang, P. and Maiolino, P., 2023. A Magnetorheological Elastomer-Based Proportional Valve for Soft Pneumatic Actuators. *Advanced Intelligent Systems, 5*(1), p.2200238.

- Wang, S., Zhang, P., He, L. and Maiolino, P., 2023. Towards Onboard Proportional Control of Multi-chamber Soft Pneumatic Robots: A Magnetorheological Elastomer (MRE) Valve Array. *Soft Robotics* (under review).

- Wang, S., He, L., Yao, Y., Liu, C. and Maiolino, P., 2023. A Toolbox for Designing 3D-printing-ready Pneumatic Circuits for Controlling Soft Robots. *Advanced Intelligent Systems* (under review).

1.4.2 Other papers contributed

- He, L., Wang, S. and Maiolino, P., 2023. Rubber-like Soft Lattice Structure for Anti-ballooning in Fluidic Elastic Soft Robots. *Advanced Engineering Materials*

- Liu, C., He, L., Wang, S., Williams, A., You, Z. and Maiolino, P., 2023. Exploring Kinematic Bifurcations for Dexterous in-hand Manipulation: a Gripper Inspired by Thick-panel Waterbomb Origami. *Advanced Intelligent Systems* (under review)

2
Literature Review

The literature review chapter is divided into three sections. The first section presents an overview of soft pneumatic robots and highlights the limitations imposed by traditional pneumatic control systems. This emphasizes the motivation and significance of the work conducted in this DPhil. The second section presents the state-of-the-art in the field that my DPhil directly contributes to, discussing each previous work on developing integrable devices for onboard computation and control of soft robots. The third section introduces the two key enabling technologies whose recent advancements facilitate the methodologies employed in this DPhil: multi-material 3D printing and soft magnetic materials.

2.1 Soft pneumatic robots

Soft pneumatic robots, defined as robots whose body is made with soft materials and driven by air pressure, offer greater embodied safety and adaptability compared with traditional rigid robots [12, 13]. This section provides an overview of the soft pneumatic actuators used by these robots, highlights the limitations imposed by the traditional pneumatic control hardware, and summarizes their applications in different fields.

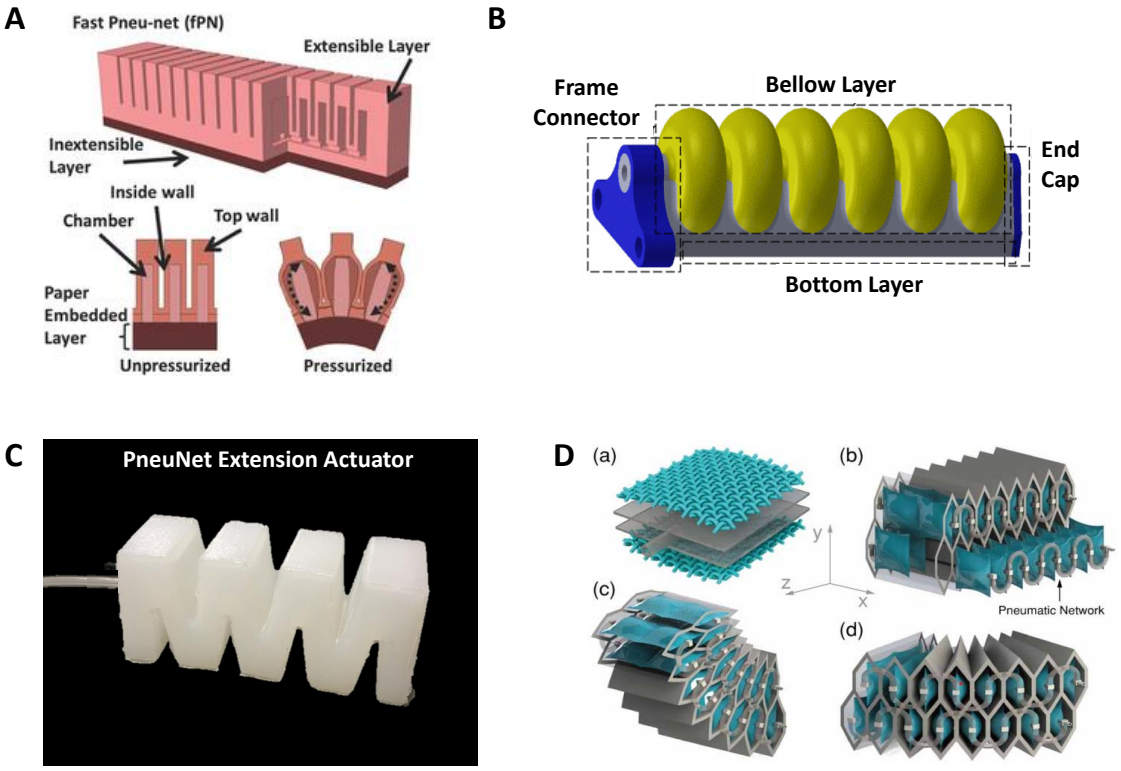


Figure 2.1: Different PneuNet actuators. **(A)** shows a classic bending actuator, reproduced from [3]. **(B)** shows a bellow bending actuator, reproduced from [16]. **(C)** shows a PneuNet extending actuator, reproduced from [17]. **(D)** shows the Honeycomb Pneumatic Networks, reproduced from [15].

2.1.1 Soft pneumatic actuators

Numerous different designs of soft pneumatic actuators have been developed in recent years [14], exploiting various structures, materials, and fabrication techniques, resulting in diverse applications. Most of these actuators can be classified into two main types: (1) pneumatic network (PneuNet) actuators, and (2) fibre-reinforced actuators [15].

PneuNet actuators, as shown in Figure 2.1(A), consist of pneumatic networks with small chambers and channels embedded in elastomeric materials [3]. Due to their low cost, fast response, high tunability, and ease of control, the concept of PneuNet has garnered considerable attention, leading to multiple variants with different geometries, motion types, structures, and fabrication techniques. For instance, as shown in Figure 2.1(B), replacing sharp-edged pleated chambers with bellow-shaped convolutions allows the actuators to retain overall movements while

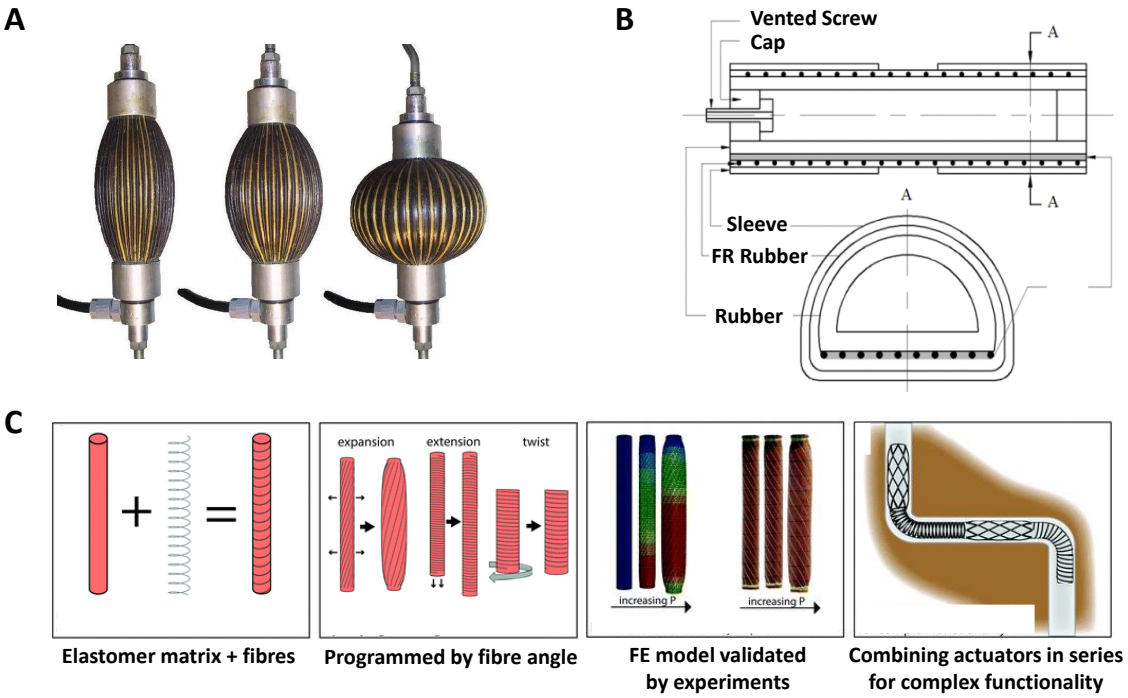


Figure 2.2: Different fibre-reinforced actuators. **(A)** shows a McKibben artificial muscle, reproduced from [15]. **(B)** shows a fibre-reinforced bending actuator, reproduced from [20]. **(C)** shows a set of fibre-reinforced actuators whose movements are controlled by fibre orientations, reproduced from [21].

reducing local material elongation [16]. Moreover, as represented in Figure 2.1(C), removing the strain-limiting layer and adjusting the air channel layouts switches the motion type of the actuators from bending to linear extending [17]. A new structure called Honeycomb Pneumatic Networks, as shown in Figure 2.1(D), has been deployed to increase the movement capability and torsional resistance of these actuators [18]. 3D printing technology has also been applied to reduce labour costs and enhance design flexibility during fabrication [19].

Fibre-reinforced actuators (see Figure 2.2), on the other hand, utilize soft elastic cavities reinforced by cuffed or embedded fibres, fabrics, or other fibre-like materials [15]. One of the most typical fibre-reinforced actuators is the pneumatic artificial muscle (PAM), originally developed by Joseph McKibben in the 1950s [22]. By placing a hollow rubber tube inside a coaxial woven sheath, the PAM can mimic the contraction of a human muscle when actuated by compressed air. Due to their lightweight, compliant, power-dense, and user-friendly nature, researchers have

modified PAMs with different chamber shapes and fibre orientations to achieve various movement types, including extension, bending, and rotation [20, 21].

To utilize these soft pneumatic actuators effectively in practical applications, precise control of the pressure inside their chambers is essential. The next subsection describes the traditional pneumatic control systems used by soft robots.

2.1.2 Traditional pneumatic control hardware

The most commonly used pneumatic control system in the field of soft robotics is the traditional pump-tank-valve system [23–27], as presented in Figure 2.3(A). In this system, the air is initially pumped into a tank as a pressure reservoir, which is usually shared by multiple valves distributing pressurized air into various chambers in the robots. Depending on the application, these valves can range from basic solenoid valves, providing digital ON/OFF control to pneumatic chambers, to more advanced proportional valves. Solenoid valves use electromagnets to regulate the flow channel, enabling operation at only two given set points [28]. While this is acceptable in many applications due to the adaptability of soft pneumatic actuators to unknown environments, their sizes (typically 32 mm $\times$ 16 mm $\times$ 10 mm, 10 grams) and capabilities should be considered case by case [29]. One should note that smaller models have lower flow rate capability and threshold pressure, limiting the soft robot's speed and strength, respectively. For applications requiring more precise control, proportional valves are used [30]. These valves modulate the airflow proportionally to applied electrical signals, enabling precise pressure control. Due to their complex structure, proportional valves are generally larger, heavier, and more expensive than solenoid valves (typically 85 mm $\times$ 60 mm $\times$ 18 mm, 70 grams, over \$500) [29]. Both solenoid and proportional valves are highly rigid due to the materials used, typically stainless steel or industrial plastic, with Young's modulus several orders larger than that of soft elastomer materials. Additionally, using these valves requires the use of a microcontroller with drivers.

Another typical pneumatic system worth mentioning is the syringe pump system [31–33], as presented in Figure 2.3(B). This system utilizes a linear stepper motor

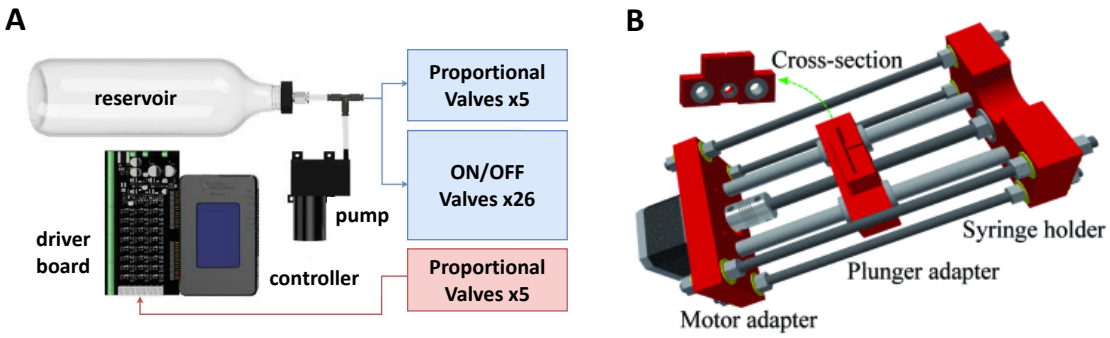


Figure 2.3: Traditional pneumatic control systems **(A)** shows a typical pump-tank-valve system, reproduced from [26]. **(B)** shows a typical syringe pump system, reproduced from [33].

to control the position of a syringe piston, thus regulating the pressure in a specific pneumatic chamber. While this approach offers a low-cost solution for precise pressure control, it comes with several limitations. Firstly, the syringe must have sufficient volume to reach high pressure, resulting in a larger size and weight. Moreover, the system's response time is limited by the linear motor's travelling speed (typically less than 10 mm/s). Finally, the system is highly sensitive to air leakage, as even a small leakage can hinder proper functioning due to the syringe's limited stroke length. Consequently, the syringe pump system is mainly suitable for applications that require precise control without the need for mobility, such as soft robotic manipulators [34].

Both the pump-tank-valve system and the syringe pump system are highly rigid. Moreover, in real soft robotic applications, they are often much heavier and bulkier than the soft robots themselves. These traditional pneumatic control systems can hardly be integrated into the soft robot structures, thus imposing significant limitations including difficulties in achieving untethered operation, compromising the benefits of using soft materials, reducing compliance, slowing down reactions, hindering miniaturization, and limiting adaptability in practical applications.

2.1.3 Applications

Pneumatic actuation is the most popular approach for grasping and manipulating objects with unknown shapes, sizes, and weights [35]. Compared with other approaches

such as cable driven [36], shape-memory-alloy (SMA) driven [37], or electro-active-polymer (EAP) driven [38], soft pneumatic actuators offer higher adaptability and safety, allowing them to interact safely with humans and environments, conform better to unknown objects, and achieve more robust grasping with a simpler control strategy. The most famous soft pneumatic grippers and manipulators are the ones developed by Soft Robotics Inc [39] and Festo [40]. The research community has also developed various soft pneumatic grippers [41–43] and manipulators [44–46] tailored to different applications. However, due to the heavy and rigid pneumatic control system, the applications of these soft robots are limited within factories or labs where being tethered is not a problem. Applying them in more challenging applications, such as mobile robots and wearable devices, remains a challenge.

Various locomotive robots are also built using soft pneumatic actuators. Different gaits, including walking [47], crawling [48, 49], and swimming [30, 50], have been achieved with these actuators. The embodied intelligence brought about by their structural compliance significantly simplifies the control strategy, especially when navigating through unknown or dynamic terrains. However, due to the contradiction between the lack of load capability of soft pneumatic actuators and the bulkiness of the pneumatic control hardware, most of these robots have to be externally tethered. The works that attempt to move the traditional pneumatic control hardware onboard suffer from limitations in operational range, movement speed, or load capability.

Finally, soft pneumatic actuators have found widespread use in wearable devices [51], mainly due to their inherently safe human-robot interaction. Companies like HaptX [52] and Meta [53] have developed pneumatically-driven gloves for virtual reality (VR) and teleoperation, featuring more than 100 micro pneumatic chambers onboard to deliver high-resolution pneumotactile feedback. Additionally, pneumatically-driven rehabilitation devices have been developed to assist patients in regaining hand or limb functions [54, 55]. The field of exoskeletons has also seen a surge of interest in soft pneumatic actuators, as they easily deform and adapt to complexly shaped bodies [56, 57]. However, a key challenge faced by these wearable devices is their limited portability. To control the pneumatic chambers on these

devices, the user either needs to carry a heavy pneumatic preparation backpack or be tethered to a fixed station, hindering their broader adoption.

2.2 Integrating devices onboard soft robots for computation and control

The previous discussion has highlighted how traditional control hardware is limiting the performance of soft pneumatic robots in numerous application scenarios. Motivated by these limitations, researchers have been working on developing novel pneumatic devices that can be integrated into the structure of soft robots while providing onboard computation or control. This section discusses some typical works on this topic.

2.2.1 Microfluidics

Microfluidic circuits provide a solution for embedding a fluidic control system within soft materials [60]. These circuits transport, mix, separate, and process small amounts of fluids in microchannels, leading to various analogues of electronic devices, from digital[61] to analogue[62] computing. An exemplary case is the Octobot [58], as presented in Figure 2.4(A). As the first entirely soft and untethered autonomous robot, this work demonstrates the feasibility of achieving intelligent behaviours, such as cyclic movements of eight pneumatic actuators, without relying on traditional control hardware. The robot is fabricated through a combination of soft lithography [63], moulding, and 3D printing. Figure 2.4 (B) illustrates the working principle of the Octobot. The cyclic movement of its limbs is controlled by a microfluidic oscillator, which periodically releases the onboard monopropellant fuel into the reaction chambers. Upon entering the chambers, catalytic decomposition occurs, driving the soft pneumatic actuators by the pressurized gas generated from the decomposed fuel. More recently, researchers have created a library of microfluidic circuits for soft robot control with unified materials and fabrication methods, paving the way for achieving more diverse computation functions [59]. As a demonstration, the work (see Figure 2.5) successfully reproduced the shift

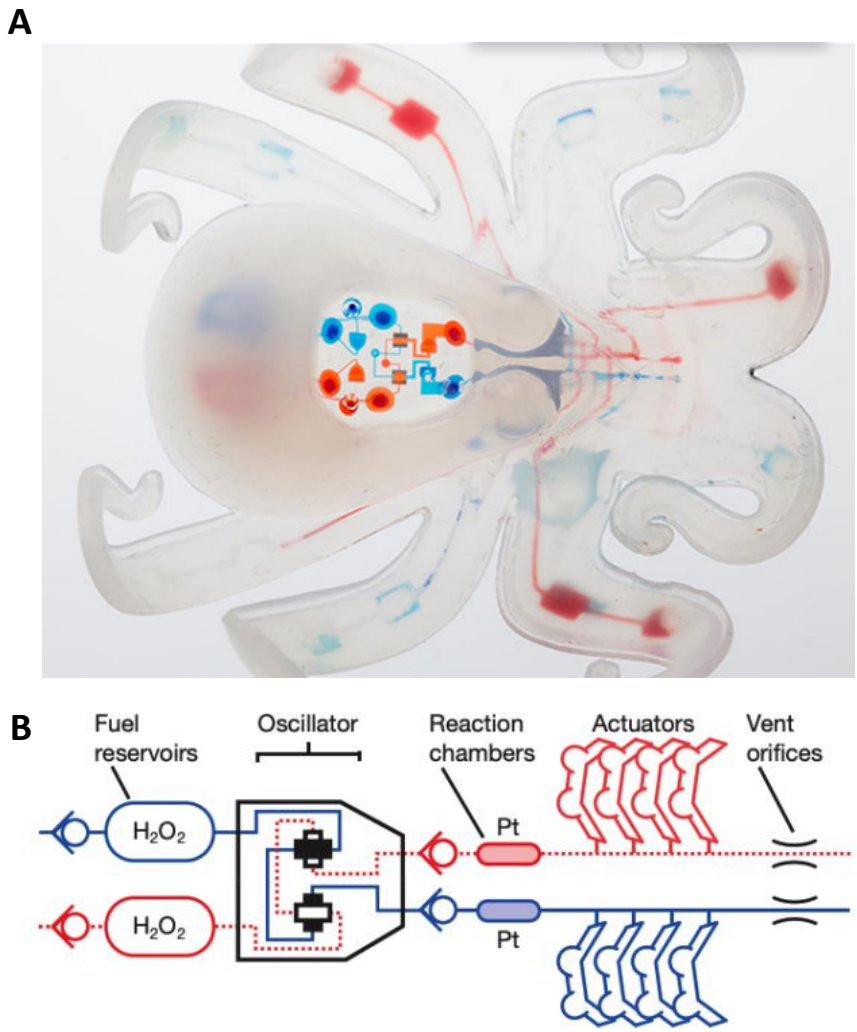


Figure 2.4: Octo-bot, controlled by an onboard microfluidic circuit, reproduced from [58]. **(A)** shows an overview of the body of Octo-bot, fabricated through a combination of soft lithography, moulding, and 3D printing. **(B)** shows the working principle of its limb movements. A microfluidic oscillator is used to periodically release the onboard monopropellant fuel into the reaction chambers. The fuel then decomposes, yielding pressurized gas which flows downstream to the pneumatic actuators and the vent orifices concurrently.

register and demultiplexer based on microfluidic circuits, thereby controlling the movement of four small-size fluid-driven actuators.

However, one common problem of applying microfluidics to soft pneumatic robots is the lack of flow rate, pressure, and consequently, power of the robots. The typical power of a microfluidic channel is on the order of 10^{-4} W. Simply scaling up the size of the microfluidic channels does not work in many cases since many of the microfluidic mechanisms depend on viscosity, and an increase in channel size

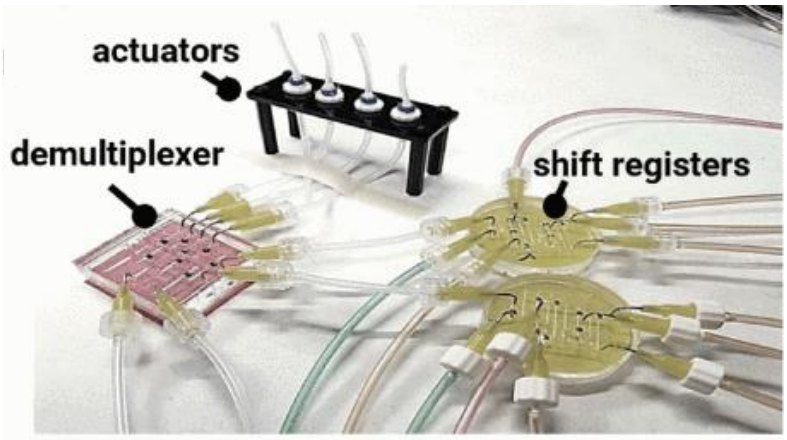


Figure 2.5: A microfluidics library for controlling soft robots, reproduced from [59]. In this example, the four fluid-driven actuators are controlled by a shift register and a de-multiplexer.

inevitably decreases that viscous effect [64]. Additionally, applying microfluidics for controlling soft pneumatic robots means that the catalytic decomposition from liquid to gas is mandatory, bringing additional design constraints. In contrast, all the works conducted in this DPhil come with a much higher flowrate (around one litre per minute) and pressure capability (more than 40 kPa).

2.2.2 Silicone tube-kinking valves

The kinking of soft tubes, as a structural instability, offers a good paradigm in the design of integrable pneumatic control devices, as this mechanism converts a small linear displacement into a secure clutch for an air channel purely based on soft materials [66]. In 2018, researchers combined the kinking tube mechanism with a pneumatically-driven semi-spherical silicone membrane, introducing an entirely soft bistable valve (see Figure 2.6 (A)) used for controlling soft pneumatic robots [8]. The bistable membrane has two stable states due to the two local minima on their strain energy curve. The state of the membrane is switched by pneumatic signals applied on both sides of the membrane. Each stable state can either "block" or "release" the flow, with the help of the kinking tube mechanisms. The valve successfully achieves flow regulation based on soft materials without requiring a continuous energy supply. As shown in Figure 2.6 (B)-(D), this kinking-tube

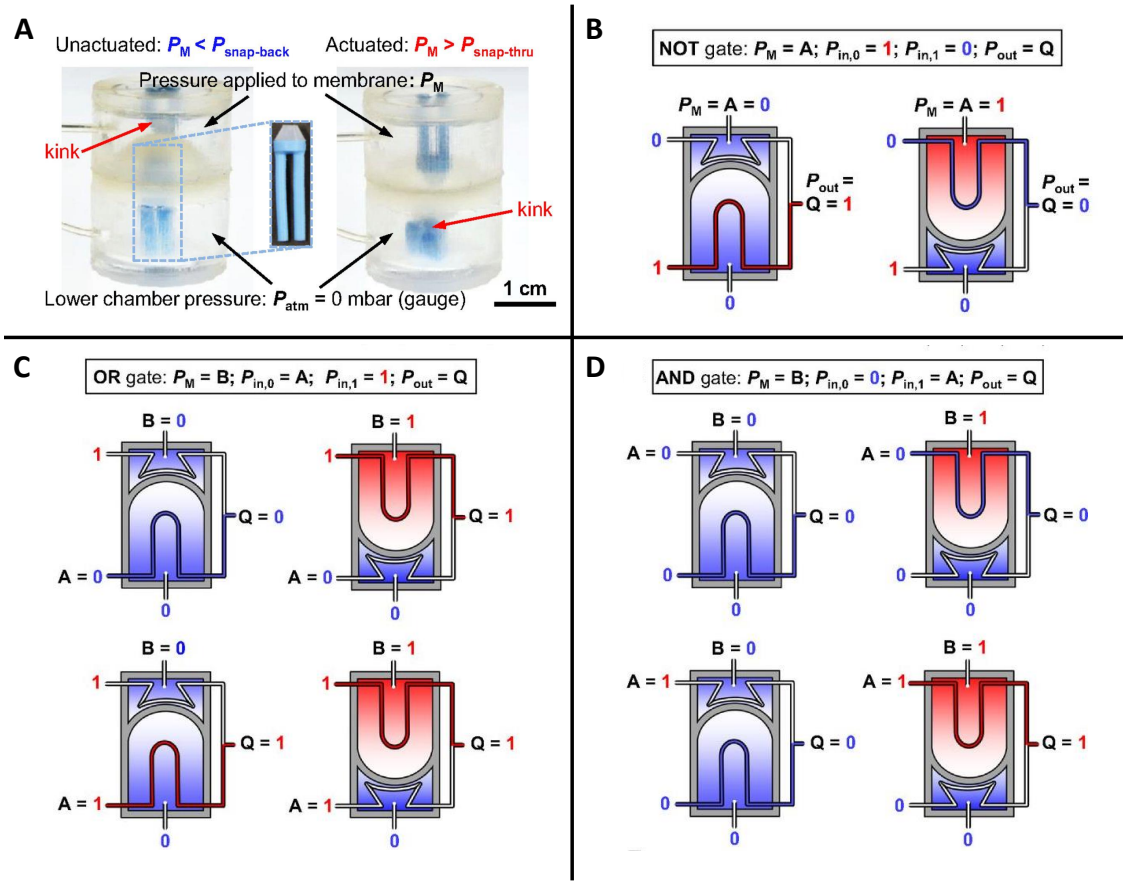


Figure 2.6: Silicone-casted valves based on tube-kinking mechanism, reproduced from [65]. **(A)** shows the basic structure of the silicone bistable valve. The silicone membrane in the middle is driven by the pressure difference between the two chambers P_M. The status of this membrane determines whether the top or the bottom tubes are kinked, therefore affecting the ON/OFF status of the air channels. **(B) - (D)** show the different configurations of the valves when being used as NOT, OR and AND gates, respectively.

valve can be rearranged into different configurations to perform different logic gate computations including NOT, OR and AND gates [65]. These logic gates can be further combined to achieve more advanced functions, including set-reset latch, shift register, leading-edge detector, digital-to-analogue converter, and ring oscillator [65]. Due to the structural bistability, the state of the valve remains stable without requiring continuous power input, making it highly suitable for use as a non-volatile memory [67]. Moreover, researchers used a pneumatic circuit composed of these silicone valves to control the bio-inspired walking of a soft, untethered quadruped robot [68]. The pneumatic circuit generates oscillatory signals, which are directly used to drive the pneumatic actuators and enable the locomotion of the legged robots.

The pneumatic signal computation capability of these valves also enables the robot to react to human control input or autonomously avoid obstacles via simple logic.

It should be noted that the fabrication of such a bistable valve is highly complex and requires expertise. Each valve is composed of 11 individual components, and each of them needs to be silicone cast and manually assembled. This results in a total manual fabrication time of at least 2 hours. The model repeatability can be affected by the manual work involved. The repeatability problem becomes more concerning when the system complexity increases with more computation units. Lastly, the threshold pressure that can be withstood by the kinking-tube mechanism is around 40 kPa, prohibiting its applications with high-pressure soft pneumatic robots. In the work conducted in this DPhil, these limitations are overcome by exploiting the multi-material 3D printing technique to simplify the fabrication and enhance design flexibility. Details of our 3D-printed works are described in Chapters 3, 4 and 7.

2.2.3 3D printed fluidic circuitry

The complex casting process of kinking-tube valves hinders their widespread use in soft robots, motivating researchers to explore solutions with simpler fabrication procedures. Multi-material 3D printing technology has rapidly grown and is now being applied to fabricate various soft pneumatic robots [70, 71]. This fabrication technique is also being employed for developing integrable pneumatic control devices [69, 72]. By leveraging its capability to simultaneously print materials with different hardness, researchers have developed a set of pneumatic circuit elements, including a diode (Figure 2.7(A)), a normally "ON" transistor (Figure 2.7(B)), and a normally "OFF" transistor (Figure 2.7(C)). The pneumatic circuitry consisting of these devices can be integrated into and fabricated together with the soft pneumatic robot in one single print. Relying on these devices, researchers achieved (i) a soft robotic turtle that performs periodic, out-of-phase gaits for its soft limbs under constant-flow input; (ii) a soft robotic turtle that leverages embedded fluidic

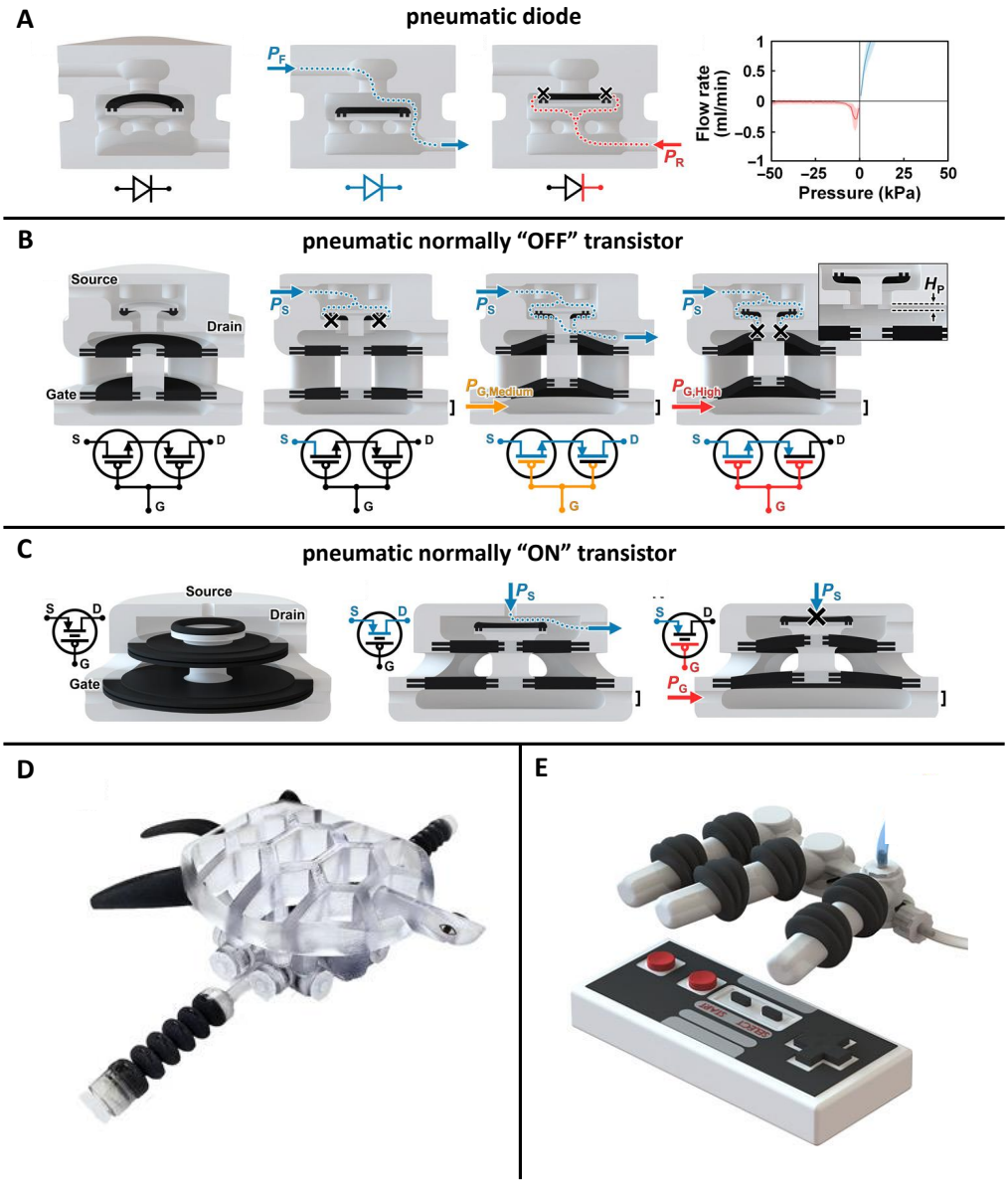


Figure 2.7: 3D printed fluidic circuitry for controlling soft robots, reproduced from [69]. **(A)** shows the basic structure and working principle of the 3D-printed pneumatic diode. When pressure is applied in the unfavoured direction, the piston will be lifted and sealed the air channel, preventing the airflow. **(B)** shows the basic structure and working principle of the 3D-printed normally "OFF" transistor. Without a gate pressure, the piston naturally seals the air channel under pressure, preventing airflow. Once sufficient gate pressure is applied, the membrane lifts the piston, allowing airflow. **(C)** shows the basic structure and working principle of the 3D-printed normally "ON" transistor. Without a gate pressure, the piston stays low and allows airflow. Once a sufficient gate pressure is engaged, the piston will be lifted and block the airflow. **(D)** presents a 3D-printed turtle with oscillatory movements controlled by the integrated pneumatic circuit. **(E)** presents a 3D-printed robotic hand pressing a game controller, also controlled by the integrated pneumatic circuit.

transistors with distinct pressure-gain properties to generate periodic swimming-inspired motions under sinusoidal pneumatic input; and (iii) a soft robotic hand capable of manipulating a video game controller.

The major benefit of this 3D printed approach is the elimination of manual fabrication, integration, and assembly procedures associated with soft robotic actuators and pneumatic circuits. This significantly enhances the repeatability of the work and eliminates leakages or other performance losses due to human error. However, the work mainly focuses on the development of these individual pneumatic devices, while it is still challenging to combine these devices into circuits with desired computation functions. To achieve a functional pneumatic circuit embedded in soft robots, one needs to consider the circuit schematic, the spatial placements of all components within the robot body, and the piping layout. These become increasingly tedious and difficult when designing circuits for more complex computations. In the work conducted in this DPhil, we designed a design automation software that automates the manual design, fabrication and assembly of pneumatic circuits for soft robots. Relevant works are described in Chapter 7.

2.2.4 Handcrafted control devices for soft robots

Another approach to simplify the fabrication of integrable control devices is by modifying their mechanical design so that the devices can be handcrafted using everyday objects (see Figure 2.8). A pioneering example of this approach is the Tube-Balloon Logic (TBL) devices [73]. TBL is a soft, pneumatic logic device that can be assembled from simple materials like tubing, balloons, and straws in under 5 minutes (as shown in Figure 2.8(A). A single TBL unit computes the pneumatic signals in a digital NOT gate manner, and the detailed working principle is described in Figure 2.8(B). Through different configurations of TBL devices, various digital computations, including NOT, NAND, and NOR gates, can be achieved. Researchers have also developed a ring oscillator that operates at high pressures (200 kPa) and high oscillation frequencies (15 Hz) to control a soft vibrating sieve, effectively separating granular media. As the first design in this field purely based on

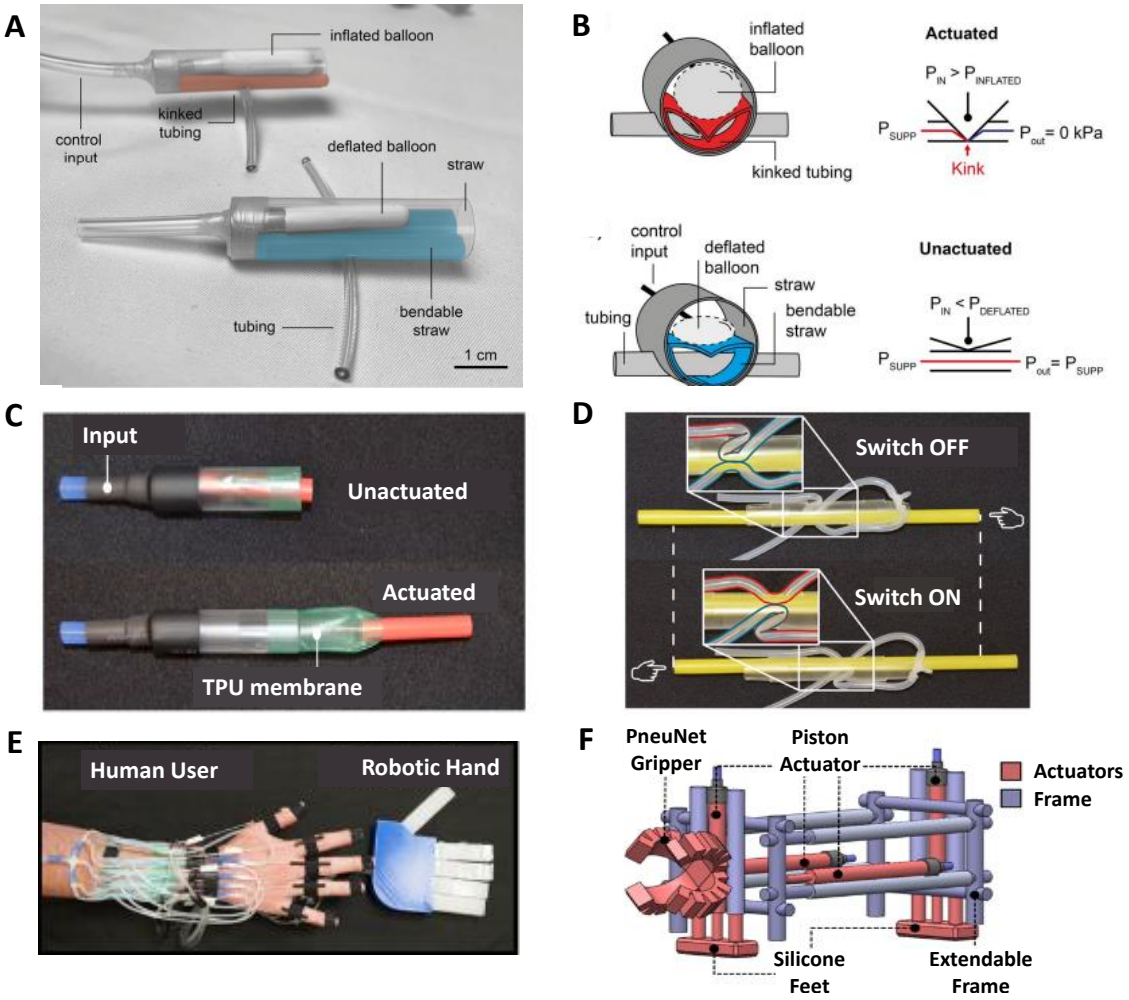


Figure 2.8: Handcrafted pneumatic control devices for controlling soft robots. **(A)** shows the basic structure of the tube-balloon logic devices, reproduced from [73]. **(B)** shows their working principles. The input pneumatic signal is applied to a balloon. Once a HIGH signal is engaged, the balloon bends a bendable straw. The bent straw then kinks the tube and therefore blocks the airflow. Such a single unit behaves like a NOT gate. **(C)** shows the structure of the piston actuator developed by [74]. A piston (red) with a bistable TPU membrane (green) is driven by the input pneumatic signal, travelling in parallel with the external tube. **(D)** presents the structure of the pneumatic switch developed by [74]. Tubes are attached to a central rod (yellow) which travels along the axial direction within the external tube. The rod kinks and blocks the top or bottom air channel depending on its current position. Combining the piston actuator **(C)** and the pneumatic switch **(D)** brings a programmable pneumatic valve enabling signal computation. **(E)** presents a teleoperated soft robotic hand controlled by the programmable soft valves, reproduced from [74]. **(F)** presents a soft crawler with a gripper onboard, also controlled by the programmable soft valves, reproduced from [74].

everyday objects, TBL devices provide an inexpensive and straightforward method to achieve onboard pneumatic control of soft robots. Despite the remarkable potential, these devices face challenges in size miniaturization, behaviour repeatability, and computation versatility. However, this innovative idea sets the stage for future advancements based on this approach.

A recent study has expanded the computational capabilities of handcrafted pneumatic control devices, transitioning from digital computation to analogue computation [74]. In this research, two modular soft components were developed using everyday objects: a piston actuator (see Figure 2.8(C)) and a bistable pneumatic switch (see Figure 2.8(D)). By combining these modules, programmable valves were created, enabling a wide range of computations, such as analogue pressure regulation, simplified digital logic, controlled oscillation, nonvolatile memory storage, and linear actuation. These capabilities were demonstrated by utilizing the system to control various soft pneumatic robots, including (1) a teleoperated soft robotic hand that mimics human hand gestures through a soft robotic glove, shown in Figure 2.8(E); (2) a pneumatic cushion matrix controlled by human input with programmable logic and; (3) an untethered autonomous locomotive robot with an onboard gripper controlled by a counter, shown in Figure 2.8(F). In addition to its comprehensive computation capabilities and ease of fabrication, the study offers other advantages, such as a high threshold pressure of 80 kPa, a fast response time of 0.3 seconds, a low cost of less than $ 5, and ease of reconfiguration and repair. However, a significant limitation of the work arises from the inconsistency caused by the manual fabrication process. This limitation becomes more problematic when multiple valves are combined into complex circuits. Moreover, the devices' handcrafted nature results in a relatively large size.

2.2.5 Magnetorheological fluid valves

Another significant approach for providing onboard control to soft robots involves regulating Magnetorheological (MR) fluid. Instead of using air to pressurize soft actuators, MR fluid serves as the actuation medium. MR fluid is a mixture of

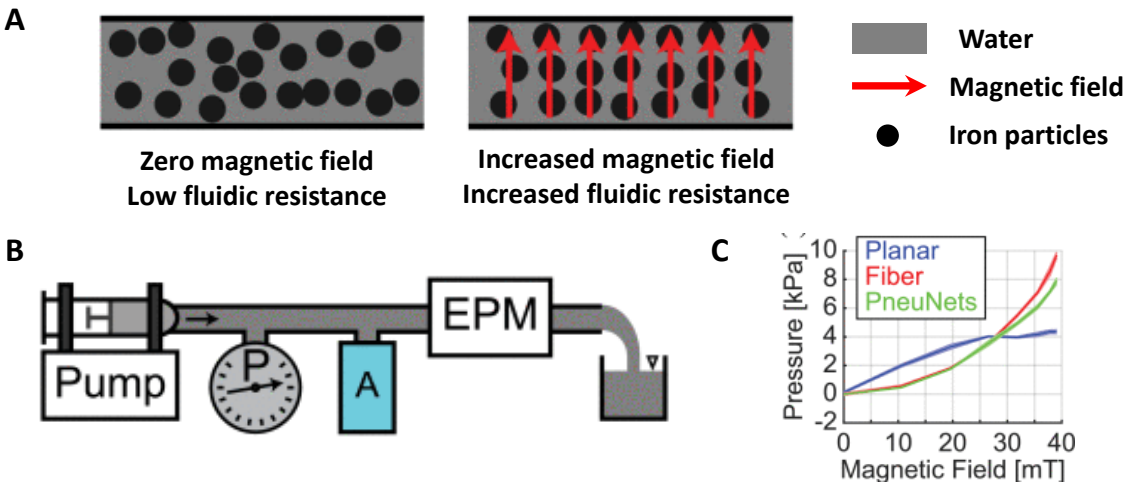


Figure 2.9: Magnetorheological (MR) fluid-based flow control for soft robots, reproduced from [75]. **(A)** shows the working principle of the MR fluid regulation. Without the magnetic field, the iron particles in the water remain free and the MR fluid has its lowest viscosity. Once activated, the externally applied magnetic flux aligns the iron particles inside into long chains, therefore significantly increasing the fluidic resistance of the MR fluid. **(B)** shows the schematic when implementing proportional control on a soft actuator via MR fluid regulation. Constant pressure MR fluid is supplied to the upstream of the actuator, while the downstream of the actuator is connected to the atmosphere via an electro-permanent magnet regulating the MR fluids. The magnetic field strength generated by the EPM determines the downstream fluidic resistance, therefore controlling the fluidic pressure inside the actuator. **(C)** presents the experimental result, showing that the mechanism can achieve continuous pressure modulation of a soft actuator.

carrier fluid, suspended ferrous particles, and stabilizing additives. As shown in Figure 2.9(A), when an external magnetic field is applied, the ferrous particles inside align into chains along the field direction. This alignment significantly alters the fluidic resistance at that position, thereby changing the fluidic pressure inside the actuator. Initially, researchers derived and validated a predictive model of this MR fluid regulation mechanism, enabling them to control a multi-chamber soft robot [76]. Electropermanent magnets (EPMs) are then used to control the jamming of MR fluids [77]. The EPM can retain the magnetization without requiring an energy supply, therefore significantly reducing the power consumption. In more recent work, continuous modulation of fluidic pressure, also known as proportional control, is achieved based on this mechanism [75]. The schematic is shown in Figure 2.9(B). By precisely controlling the magnetization of EPM, the researchers were able to precisely control the pressure within various soft actuators, as shown

in Figure 2.9(C). This fully modulated actuation of soft fluidic actuators enables precise control of their deformation or generated force.

However, some challenges still exist. The trade-off between response time and the operational pressure range of the robot is non-linear and influenced by numerous factors, including channel dimensions, actuator mechanics, and EPM properties. Adapting these MR fluid valves to different applications requires a certain level of expertise. Moreover, using MR fluids as the actuation medium makes the system highly sensitive to any leakage and increases the overall weight of the system. In the work conducted in this DPhil (see Chapter 5 and 6), we exploited MR elastomer instead of MR fluids to develop soft proportional valves for soft robots. These devices retain the advantages of magnetorheological effect and can regulate various actuation mediums including air and water, therefore greatly broadening their applications.

2.2.6 Fluidic control based on dielectric actuators

Dielectric actuators (DEAs) are a type of soft robotic actuator that operates based on dielectric elastomer materials, which exhibit changes in shape or size when subjected to electrical stimulation. Their compliant nature, fast response, and high energy density make them good candidates for integrable pneumatic control hardware.

Initially, researchers developed a soft proportional valve based on DEAs [78]. The valve consists of a set of DEAs with an indenter attached to their ends. A soft air channel is located beneath the indenter, allowing the channel to be blocked or released by the indenter as required. The valve enables effective pneumatic control of up to 51 kPa of pressure and a 40 mL/min flow rate, with a response time of less than 0.1 s. Deploying a similar working principle, researchers developed a peristaltic pump based on DEAs more recently [79]. The pump comprises an array of high-power-density DEAs, each weighing 1.7 grams, operating in a programmed pattern. The pump can generate pressure waves in a fluidic channel with a maximum pressure of 12.5 kPa, a run-out flow rate of 0.039 L/min, and a response time of less than 0.1 seconds.

The major limitation of these DEA-based devices is the high operating voltage required (at least 1700 V). Additional devices must be introduced into the robot to provide the driving voltage, increasing the system complexity. Moreover, both the DEA-based valve and pump require a rigid mechanical frame to work properly. This significantly reduces the structure compliance and prevents a homogeneous integration with the soft robots.

2.2.7 Approaches without mimicking electronics

Most of the approaches mentioned above, aimed at achieving integrable control of soft robots, are designed based on similar principles used in electronics. In other words, these devices can often be considered as the pneumatic counterparts of electronic components, such as transistors, logic gates, and oscillators. This allows those well-established electronic design principles to be readily adapted to aid the development of pneumatic circuits, especially in highly complex situations. However, there are also several works that do not rely on mimicking electronics, shown in Figure 2.10. Although these approaches usually lack versatility, have limited functions, and are suitable only for specific scenarios, they demonstrate promising performance when applied. This section highlights several works of this kind.

Converting a constant fluid flow or pressure into an oscillatory flow is one of the keys to enabling untethered fully autonomous locomotive robots. In approaches that mimic electronics, this is typically done using a ring oscillator consisting of an odd number of NOT gates (at least three) connected in a loop. In 2022, researchers designed a soft fluidic relaxation oscillator that provides the oscillatory signal with a much simpler structure [80]. The key mechanism within the oscillator is a curved membrane with three slits meeting at its apex (see Figure 2.10(A)). These slits enable fluid flow when snapped through but prevent the flow when snapped back. As the pressure required to snap through and snap back the membrane is different, mechanical hysteresis is translated into fluidic hysteresis, effectively converting a constant fluid flow into an oscillatory flow. This integrable oscillator has been demonstrated in the application of a soft worm robot.

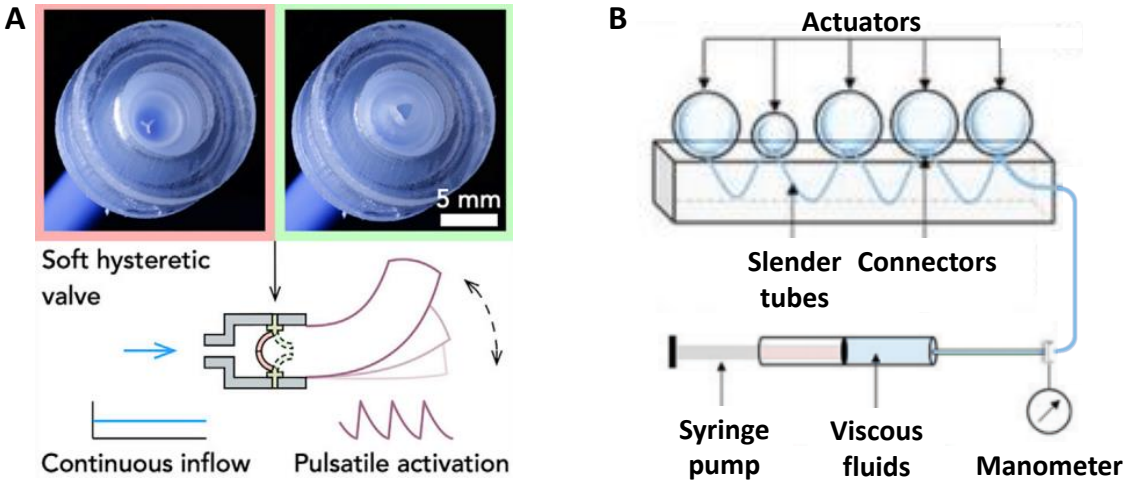


Figure 2.10: Integrable pneumatic control devices for soft robots without mimicking electronics. **(A)** shows a fluidic relaxation oscillator, reproduced by [80]. Three slits are cut on a soft hysteretic membrane, meeting at its apex. The membrane, therefore, blocks the airflow before the snap-through and allows the airflow after the snap-through. This allows the device to convert a continuous inflow into a pulsatile activation. **(B)** presents the concept of leveraging actuator mechanics, fluid dynamics, and structural bistability to control the actuation sequence of multiple soft actuators via a single pneumatic input, reproduced from [81]. The pneumatic actuators are all connected in series with slender tubes for an enhanced viscosity effect. Each actuator here comes with its structural bistability. With careful modelling, such a system can reach and maintain any desired state combination of the soft actuators through a single pneumatic input provided by the syringe pump.

Another interesting work that doesn't mimic electronics focuses on the actuation sequencing of multiple pneumatic actuators through mechanical intelligence [82]. Multiple actuators are connected to the same pressure supply, and their actuation sequence is programmed through the interaction between nonlinear actuators and passive flow restrictions. A model is discussed to predict the sequencing of multiple actuators, and its feasibility is validated on an 8 DOF walking robot, where each limb comprises actuators with a sequence embedded in their mechanical properties. The significant advantage of this approach is that it doesn't require any active or passive valves; the programmable actuation sequence is solely based on the nonlinear mechanics of the soft actuators and the fluid dynamics of the airflow inside. As a result, the soft robots have fewer components, are lighter in weight, and have simpler structures. However, it also imposes additional restrictions on the actuator design (dimensions, stiffness, shapes, etc.), which limits design flexibility.

A more recent study also focuses on controlling multiple actuators simultaneously with a single pressure input. In addition to exploiting actuator mechanics and fluid dynamics, the work introduces bistability into the system [81]. As shown in Figure 2.10(B), by controlling the single flow rate input, the system achieves an irreversible sequence of transitions that can reach and maintain any desired state combination of all soft actuators. This method allows for bypassing the complexity of individually controlling each actuator with separate inputs, offering the promising potential for developing minimal-control soft actuators suitable for soft robotics. However, it also introduces additional constraints on the actuator design, which may pose challenges in real applications.

2.2.8 Summary: a comparison between our work and the literature

This subsection presents Table 2.1, summarizing the key performance of our work alongside several existing works in the literature.

Table 2.1: Performance comparison between our work and the state of the art.

Work	Pressure (kPa)	Flowrate (lpm)	Size (mm)	Actuation	Fabrication	Digital/ Analog
Our 3D-printed valves [83, 84]	180	7	8*8*30	Pneumatic	3D printing	Digital
Our MRE valves [85]	41	1	30*30*12	Electric 12 V	Casting	Analog
Microfluidics [58]	10	10^{-3}	10*10*2	Fluidic	Soft lithography and moulding	Digital
Silicone bistable valve [8]	40	10	15*15*30	Pneumatic	Casting	Digital
3D printed transistor [69]	60	5	18*18*15	Pneumatic	3D printing	Digital
MR Fluids regulation [75]	15	unknown	15*15*15	EPM	Manual	Analog
DEA [79]	51	0.04	25*15*15	Electric 1700 V	Manual	Analog
Programmable soft valves [74]	70	unknown	80*15*15	Pneumatic	Manual	Digital

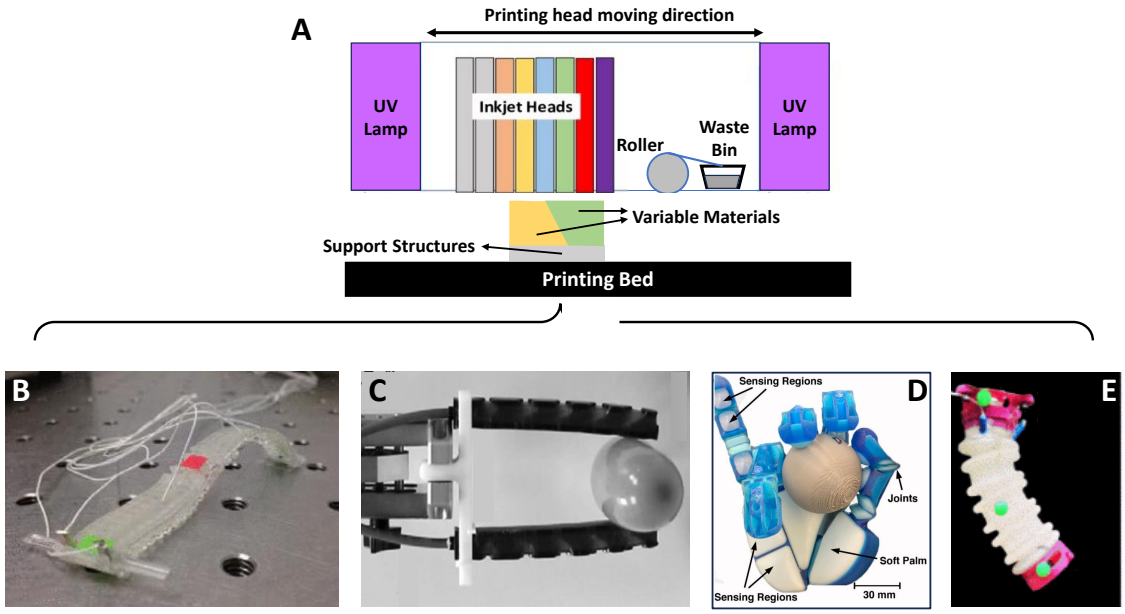


Figure 2.11: Polyjet Multi-material 3D printing. **(A)** shows the working principle of this fabrication technique. This fabrication technique has been used to develop various soft robots, such as **(B)** a soft crawler [86], **(C)** a soft gripper [87], **(D)** a soft hand [88], and **(E)** a soft robotic arm [34].

2.3 Key enabling technologies

This section discusses the two key technologies that enable the methodology deployed in this DPhil, which are Polyjet multi-material 3D printing and soft magnetic materials.

2.3.1 Polyjet Multi-material 3D printing

PolyJet multi-material 3D printing (see Figure 2.11(A)) is an innovative additive manufacturing technology that enables the creation of complex objects using multiple materials in a single print [89–91]. In this process, photopolymer materials are jetted through the printing head and then UV-cured layer by layer to build the final 3D model. This allows each layer to be composed of different materials with varying mechanical and optical properties, resulting in highly functional and intricate objects. Importantly, the properties of the materials can be continuously adjusted by varying the combination ratio of the uncured photopolymer resin [92].

This technology offers numerous advantages when utilized for fabricating integrable pneumatic circuits. Particularly noteworthy is its ability to print with multiple materials, allowing for the effortless creation of inhomogeneous structures with adjustable hardness levels. This, in turn, creates opportunities to manufacture intricate valve structures in a single process and to finely adjust the mechanical behaviour of pneumatic circuits suiting specific applications. As shown in Figure 2.11(B)-(D) respectively, the multi-material capability of this fabrication method has been exploited by many soft roboticists to program the embodied intelligence of their soft robotic devices, including a soft crawler [86], a soft gripper [87], a humanoid hand [88], and a soft robotic arm [34]. Furthermore, the capability to print dissolvable support structures is crucial for developing pneumatic circuits that usually come with complex chambers and channels. This enhances design flexibility and simplifies post-processing procedures. Moreover, the high precision of these printers is advantageous for miniaturizing pneumatic circuits, enabling the achievement of more intricate computations within the confined space of soft robots. The automated nature of 3D printing also unlocks the potential for programmable manufacturing and design automation. Additional advantages of PolyJet multi-material 3D printing encompass excellent manufacturing repeatability, user-friendliness, and rapid printing times.

However, being a relatively new manufacturing technique, several challenges must be addressed. The working principle of the printer demands that the photopolymer resins used must cure under the same UV strength and duration [93]. This constraint limits the available material choices and leads to materials with significant ageing properties. The mechanical and optical properties of the materials change relatively quickly due to exposure to environmental UV radiation, introducing inconsistency and unpredictability in the behaviour of the pneumatic circuit [94, 95]. Additionally, materials compatible with this printing technique often exhibit relatively high viscoelasticity [96], limiting the computation speed of the pneumatic circuits and increasing the energy dissipated during computation.

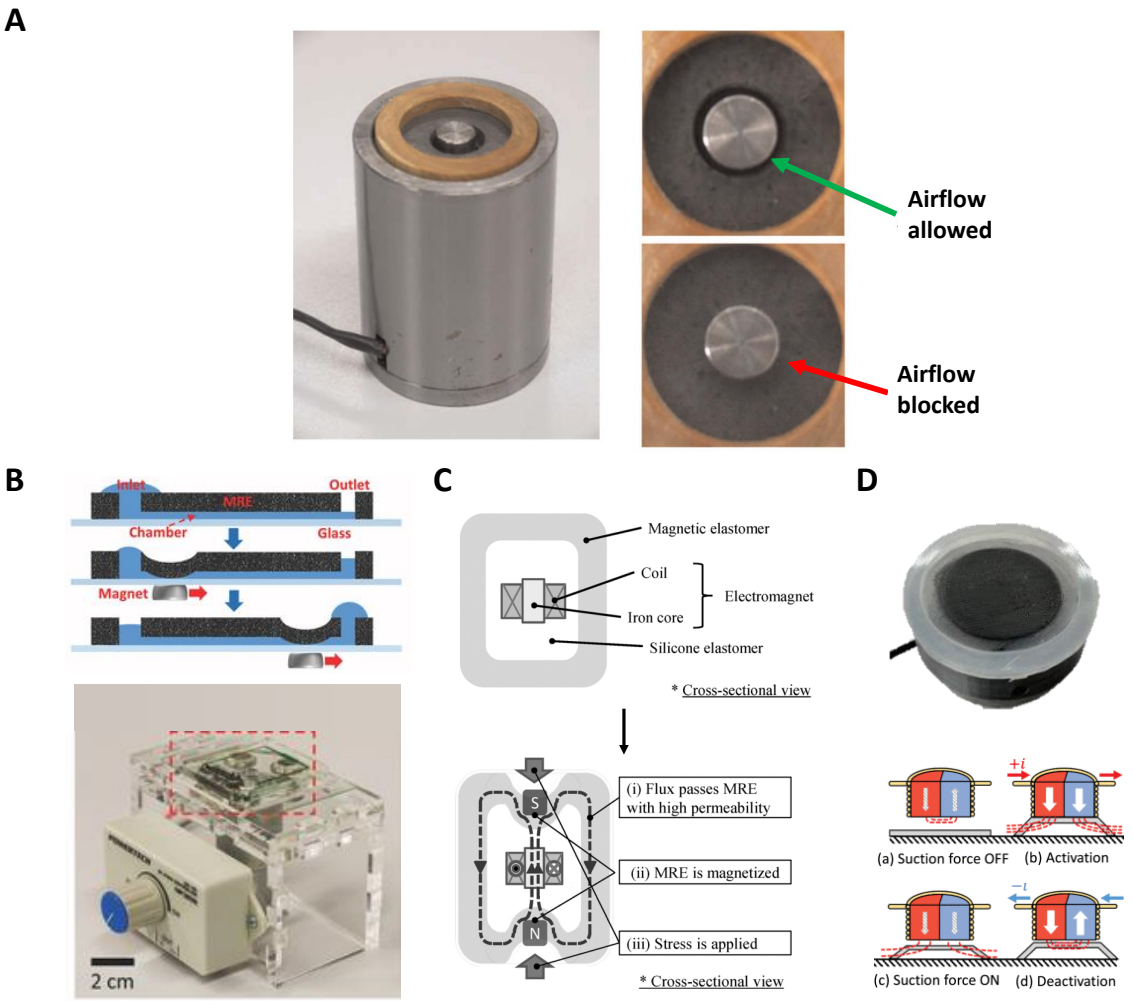


Figure 2.12: Magnetorheological Elastomer (MRE) and its applications in soft robotics. **(A)** shows the fabrication process of the majority of MRE, reproduced from [97]. **(B)** shows a microfluidic platform with pumps and mixers based on MRE, reproduced from [98]. **(C)** presents a soft actuator based on MRE, reproduced by [99]. **(D)** presents the structure and working principle of a soft grasper based on MRE, reproduced by [100].

2.3.2 Magnetorheological Elastomer (MRE)

Magnetorheological elastomers (see Figure 2.12) are a family of smart materials first developed in the 1990s [101]. They are composite materials comprising magnetic particles dispersed in an elastomeric matrix. These magnetic particles, typically micron-sized iron particles or magnetite, interact with an external magnetic field, leading to a rearrangement of the particles within the elastomer matrix. As a result, the material's mechanical properties can be altered in real-time, providing tunable and controllable behaviour [102]. These remarkable characteristics make

MREs highly promising for a wide range of engineering applications, including vibration control [103], adaptive structures [104], and soft robotics [105]. This section introduces the different properties of MRE and discusses their potential to be used for developing integrable valves controlling soft pneumatic actuators.

One of the initially exploited properties of Magnetorheological Elastomers (MREs) is their ability to change stiffness when exposed to a magnetic flux. When a magnetic field is applied, the magnetic particles within the elastomer align themselves with the field lines, resulting in a significant increase in the shear modulus. This percentage increase in stiffness exceeds 100% under a magnetic field of no more than 0.5 T [106], putting MRE into various industrial applications, especially vibration absorbers. This stiffening effect of MRE is also highly beneficial when developing integrable valves for controlling soft pneumatic robots. The increased stiffness under magnetic flux brings reduced structural deformation of the air channel, even when subjected to high pneumatic pressure. This, in turn, facilitates more reliable airflow regulation and raises the threshold pressure of the valve based on MRE.

Another important property of MRE that is highly useful when developing valves or other pneumatic devices is its magnetic-induced deformation. Due to the magnetization of the particles inside and the compliant nature of the elastomer matrix, the MRE deforms swiftly along the exposed magnetic field with a response time in the order of a few milliseconds [107]. Moreover, the deformation increases relatively linearly with the magnetic field strength. Based on this property, researchers developed a rigid valve exploiting MRE as the core actuator [108], achieving fast and secure regulation of airflow (see Figure 2.12(A)). Although this valve design is still bulky and rigid, it shows that MRE has great potential to be used for developing integrable proportional valves used by soft robots. Other soft robotic applications of MRE exploiting its magnetic-induced deformation are shown in Figure 2.12(B)-(D), including microfluidic pumps [98], soft contraction actuators [99], and soft grippers [100].

3

3D Printed Bistable Valve with Tunable Characteristics

Contents

3.1 Problem 33
3.2 Objective 34
3.3 Key contributions 34
3.4 Summary of the results 35
3.5 Contributed Paper 35
3.6 Supporting Information 44
3.6.1 Supporting Video 44
3.6.2 CAD files 44

3.1 Problem

As described in Chapters 1 and 2, the objective of this DPhil is to develop integrable pneumatic circuits to achieve both onboard signal computation and pneumatic control of soft robots. Regarding control, soft robots require valves that can be integrated within their soft body while regulating airflow with sufficient pressure and flowrate tolerance. Regarding computation, a noteworthy requirement is the development of a pneumatic memory device capable of storing binary information without needing a continuous energy supply. This is crucial for computation as it

provides soft robots with "memory" of the pneumatic signal, even after a power reset. To address the requirements from both computation and control aspects, researchers have developed a silicone-casted bistable valve [8], the details of which are discussed in Section 2.2.2. However, a significant issue with this device is its silicone-casted nature, which makes the fabrication process highly time-consuming and labour-intensive. Furthermore, the key design dimensions are less flexible to adjust. Lastly, the repeatability and consistency of this design are not guaranteed.

3.2 Objective

The objective of this study is to develop a 3D-printed, pneumatically-driven bistable valve, addressing the issues encountered in the previous research [8]. Leveraging multi-material 3D printing techniques (discussed in Section 2.3.1), the fabrication process is notably streamlined, leading to enhanced manufacturing repeatability and consistency. Additionally, this approach improves design flexibility, making the valve ready for immediate inclusion in various soft robotic systems.

3.3 Key contributions

The contributions of our 3D-printed bistable valve with tunable behaviours are as follows:

- The work is the first bistable valve (pneumatic memory device) in the community which exploits multi-material 3D printing technology and therefore significantly simplifies the fabrication and increases the design flexibility.
- A theoretical model which accurately predicts the bistable behaviour of the valve.
- A comprehensive characterization of the valve behaviour against three different design parameters.
- Improved model consistency and design flexibility compared with previous work [67].

3.4 Summary of the results

The work introduces a 3D-printed bistable pneumatic valve with a method to tune the critical pressure with predefined design parameters. A theoretical model based on beam theory and the Rayleigh-Ritz method was derived, successfully validating the bistability of the valve. The model also predicted the snap-through behaviour of the valve with an RMSE of 7.68 kPa in the switching pressure. According to the experimental results, the critical switching pressure of the valve can be tuned over a wide range from 15.3 kPa to 65.2 kPa by adjusting the thickness, the slope angle, and the material hardness of the conical shells. The response time of the valve is around 1.8 seconds, which is considerably slower than the silicone casted bistable valves ($\tilde{0}$.4 seconds). The effects of different support removal techniques were also investigated experimentally. Compared with water-jetting, the chemical bathing technique decreases the critical pressure by 20.4 % and reduces the response time by 31.2 %. It also brings better durability over the fatigue tests. The samples post-processed with water-jetting failed after only 32 cycles while the samples post-processed with chemical bathing survived the fatigue tests of 500 cycles.

3.5 Contributed Paper

The work has been published as a journal paper in IEEE Robotics and Automation Letters (RA-L), and presented in an oral session at ICRA 2023 in London, UK. The paper is attached on the following pages.

Design and Characterization of a 3D-printed Pneumatically-driven Bistable Valve with Tunable Characteristics

Sihan Wang[1], Liang He[1*] and Perla Maiolino[1]

***Abstract*—Although research studies in pneumatic soft robots develop rapidly, most pneumatic actuators are still controlled by rigid valves and conventional electronics. The existence of these rigid, electronic components sacrifices the compliance and adaptability of soft robots. Current electronics-free valve designs based on soft materials are facing challenges in behaviour consistency, design flexibility, and fabrication complexity. Taking advantages of soft material 3D printing, this paper presents a new design of a bi-stable pneumatic valve, which utilises two soft, pneumatically-driven, and symmetrically-oriented conical shells with structural bistability to stabilise and regulate the airflow. The critical pressure required to operate the valve can be adjusted by changing the design features of the soft bi-stable structure. Multi-material printing simplifies the valve fabrication, enhances the flexibility in design feature optimisations, and improves the system repeatability. In this work, both a theoretical model and physical experiments are introduced to examine the relationships between the critical operating pressure and the key design features. Results with valve characteristic tuning via material stiffness changing show better effectiveness compared to the change of geometry design features (demonstrated largest tunable critical pressure range from 15.3 to 65.2 kPa and fastest response time $\leq 1.8s$).**

***Index Terms*—Soft Robot Applications, Additive Manufacturing, Hydraulic/Pneumatic Actuators**

I. Introduction

PNEUMATIC soft robots are of interest to an increasing number of researchers due to their compatibility in highly unstructured and dynamic environments [1]. Most soft pneumatic robots are based on the interaction between regulated air and soft elastomeric materials with high adaptability and compliance. This mechanism brings various advantages including (i) low cost; (ii) flexible manufacture choices such as silicone casting, 3D printing, and blow film extrusion; (iii) safe human-robot interaction; and (iv) adaptability to environments or objects with unknown kinematics or dynamics. These valuable characteristics lead to the development of various pneumatic actuators with different structures, action types, pressure ranges, and fabrication methods [2]. However, most soft pneumatic actuators still require conventional electronic controllers and hard valves to regulate the internal fluid and control the actuation, sacrificing some benefits of being soft [3, 4, 5]. The existence of these tethered external rigid pressure systems severely limits the mobility and application fields of soft robots. This is particularly challenging in the design of soft robots for extreme environment operations (e.g., nuclear plant exploration with high-radiation, tissue interaction during metal-free scenarios in magnetic resonance imaging). Although rigid electronic controllers allow multimodal sensor integration into the system [6], the conversion of sensory information into an electrical signal before being processed to pneumatic signal control brings additional system complexity and limits the application in extreme conditions.

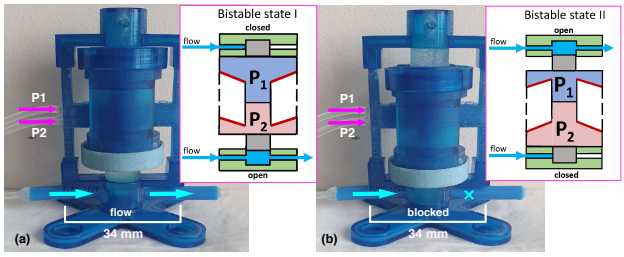


Fig. 1. Pneumatically-driven bistable valve at each bistable state **(a)** and **(b)**. P_1 and P_2 represent the two pressures that are used to switch the state of the valve.

A potential solution is to replace the rigid pneumatic power transmission with soft computational elements, where the adaptability and usability of the soft robotic system can be improved. The challenge for designing an ideal computational system for soft pneumatic robots is how to store information in the physical structure without a continuous external energy supply while receiving/processing pneumatic signals via soft interfaces. For instance, a soft robot with integrated soft computation elements should perform on-board computation without converting the pneumatic information to electronic signals. The properties and behaviours of the transmission devices should also come with high design flexibility so that the individual control element can be adapted into different applications. The development of electronic-free valves is a critical contribution to the future of fully soft robots required in extreme environments.

A bi-stable structure allows the electronic valve to be operated without a continuous energy supply. Each stable state can be used as either "blocking" or "releasing" the flow. The use of the semi-spherical bistable structure in soft-

Manuscript received: June, 08, 2021; Revised September, 09, 2021r; Accepted September, 30, 2021.

This paper was recommended for publication by Editor Kyu-Jin Cho upon evaluation of the Associate Editor and Reviewers' comments. This work was supported by the Engineering and Physical Sciences Research Council (EPSRC) Grant EP/V000748/1; S. Wang was supported by the CSC-PAG Oxford Scholarship for his DPhil study.)

[1]Authors are with the Oxford Robotics Institute, University of Oxford, UK sihan.wang/liang.he/perla.maiolino@eng.ox.ac.uk

*Corresponding Author: Liang He

Digital Object Identifier (DOI): see top of this page.

matter computing has previously been demonstrated in [7]. A passive bi-stable membrane driven by external pressure is used to press and make the internal tubing buckle, therefore regulating the flow based on the input pneumatic signal. The valve successfully achieves the flow regulation based on soft materials without requiring continuous energy supply. However, the silicone casting process makes the fabrication time-consuming, while the key design dimensions are less flexible to adjust. The system repeatability is also low as it requires a large amount of manual work during fabrication. [8] used pneumatic circuits composed of a similar semi-spherical bistable structure to control the basic walking gaits of a soft legged robot without electronics. These circuits generate oscillatory signals, which are directly used to drive the pneumatic actuators, therefore successfully controlling the locomotion of the legged robots. The idea of buckling a soft tube as a mechanical "switch" to block the airflow is easy for soft robot integration [9]. However, the behaviour consistency during operation is normally of concern when the system complexity increases with more transmission units. The kinking of the tube also brings large local stress in the elastomer, which reduces the durability of the structure and decreases the maximum controllable pressure.

A different approach for electronics-free pneumatic control is developed by [10], where the interaction between three different pneumatic actuators in a soft crawler is controlled by three soft switch-valves adhered to the skins of the robot. The dominant advantage of this work is that, the parameters of these valves can be adjusted from the exterior of the robot through simple geometrical changes. However, these valves work with only pneumatic actuators with large working stroke, as it requires sufficient deformation to kink the elastomeric tubes and block the flow. Soft material 3D printing technique [11, 4] provided another possible approach to create bi-stable structures with enhanced model repeatability, increased design flexibility, and ease in fabrication. Compared with silicone casting, 3D printing of thin bi-stable membrane brings reliable consistency in each batch of fabrication, which guarantees the repeatability of the snap-through behaviour. High design flexibility is also introduced to the valve development since the material stiffness and membrane geometry can be effectively tuned to change the required control conditions.

Thus, this work presents the novel design of a 3D printed electronic-free valve which takes pneumatic signal as input to regulate the airflow in specific air channels. The valve design consists of two soft, pneumatically-driven, and symmetrically-oriented conical shells with structural bistability and soft pistons to achieve stable regulation of the airflow. The paper discusses how the valve behaviour (critical switching pressure and response time) can be altered by changing several key design dimensions (material stiffness, structure geometry) so that it is ready for immediate inclusion in a wide range of pneumatic systems. This work also investigates how different support removal techniques affect the valve behaviour and durability.

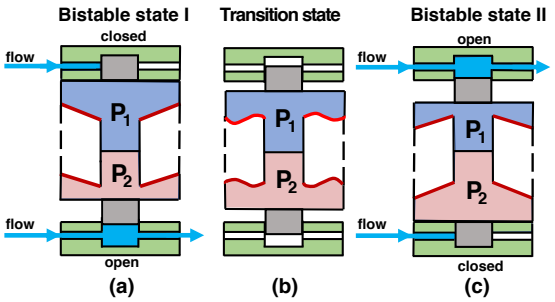


Fig. 2. Schematics of the bistable valve. The valve consists of two symmetrical compliant bistable conical shells (shown by red lines), switching in the opposite state (one "expanded" and one "contracted"). The internal pressures in each shell (P_1, P_2) indicate the valve control signal. **(a)** Bistable state I: the top chamber is "expanded" while the bottom chamber is "contracted." This means the top air channel is closed while the bottom air channel is opened. **(b)** An unstable transition state located between the two stable states. **(c)** Bistable state II: the top chamber is "contracted" while the bottom chamber is "expanded." This means the bottom air channel is closed while the top air channel is opened.

II. Design and Fabrication of the Bistable Valve with Tunable Characteristics

A. Working principle of the bistable valve

The operation of the valve makes use of a bistable structure with two internal chambers to get rid of the requirement of a continuous power supply. The bistable structure has two stable states and can be switched from one state to another by applying a pneumatic signal (positive pressure) to one of the chambers. The state of the bistable structure is used to decide whether or not the controlled air channel should be blocked. The blocking is achieved by two pistons attached to the bistable structure. When any of the pistons is pressed into the piston cylinder, the air cannot go through the corresponding air channel any more as the piston is physically in its way. The high accuracy of the Polyjet 3D printer used in this work enables optimal fit between the piston and the cylinder to prevent leakage.

One typical switching stroke for the valve is shown as followed. (i) the valve remains stable in the state shown in Fig. 2(a). In this case, the top control channel is blocked while the bottom channel is released. (ii) Once sufficient positive pressure is applied to the bottom shell, the bottom shell will be switched to an "expanded" state. Due to the restricted length of the tether (black dashed line in Fig. 2(a)), only one shell can be in the "expanded" state at one time, which means the top shell will be pulled to its "contracted" state. The top controlled air channel is then unblocked, while the bottom controlled channel is blocked as shown in Fig. 2(b). (iii) The driving pressure in the bottom shell is then removed. The state of both control channel will not change thanks to the bistability of the structure.

The snap-through process of the soft bistable structure determines the switching behaviour of the valve. This means by adjusting the design of those bistable conical shells, the critical pressure required to switch the state of the valve can be altered to fit the users' needs.

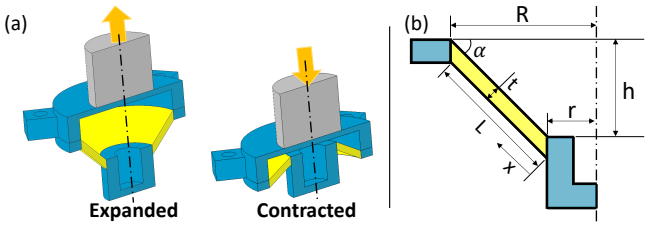


Fig. 3. **(a)** Cross-sectional view of one bistable shell under both "expanded" and "contracted" state. The blue part is printed with Stratasys Vero, the grey piston at each end is printed with Stratasys Agilus 30, while the yellow part is printed with digital material which is a combination of Stratasys Vero and Agilus 30. **(b)** Annotated cross-sectional view of the bistable structure used in the valve (yellow region). R is the outer radius of the soft conical shell. r is the inner radius of the soft conical shell. h is the height of the conical shell (the vertical displacement between the outer and inner edge). t is the thickness of the conical shell, x is the distance along the cone slant counting from the inner edge, and α is the slope angle of the conical shell.

B. Fabrication

The use of a multi-material 3D printer (J735, Stratasys Ltd, USA) allows the stiffness of the bistable valve to be digitally tuned in the design stage with precision control of the mechanical property. The J735 uses Polyjet technology, which deposits multiple droplets of uncured material, rolls them to combine and then UV cures the blend. By combining VeroWhite (a rigid plastic-like material with a quoted tensile strength of 50-65MPa and Shore hardness of 83-86D) and Agilus30 (a soft and rubber-like material with a quoted tensile strength of 2.1-2.6MPa and Shore hardness of 30A), a finite set of digital materials with variable stiffness can be printed (40, 50, 60, and 70 shore hardness). The digital material creation is made with the "digital material" function in the GrabCAD Print slicer (Stratasys, Ltd. USA) by selecting the shore hardness, while the repeatability has been well characterized by several previous works [12, 13]. These digital materials with tunable hardness are used to print the compliant conical shell (shown in red in Fig. 2). The piston is printed by pure Agilus 30, so its compliance ensures reliable sealing. Two different support removal techniques (physical removal and chemical bathing) are investigated and their effect on the valves are compared and discussed. Physical removal is achieved by using a water-jetting machine (GEMINI Cleaning ECO-400) while chemical removal is achieved by placing the valve in a tank (GEMINI SSR-550) filled with chemical support removal solution (0.02 kg/L Sodium Hydroxide and 0.01 kg/L Sodium Metasilicate).

III. Theoretical Model

Fig. 3(a) shows the cross-sectional view of one bistable shell under both "expanded" and "contracted" state. The state can be switched by the internal pressure as it exerts a uniformly distributed load to the entire internal surface of the shell, therefore expanding or shrinking the internal volume. The volume change are mostly contributed by the deformation of the conical shell (shown in yellow in Fig. 3) as it is printed with more flexible material combined with Agilus30 and VeroWhite. When the structure deforms from one state to another, the height of the cone h decreases to zero and then increases on the opposite direction, therefore the length of the cone slant L decreases and then increases again due to the Pythagoras' theorem. This shortening process compresses and buckles the conical shell and therefore brings bistability to the structure.

To further investigate the feasibility and snap-through behaviour of this pneumatically driven bi-stable structure, a theoretical model is built and investigated. The relationship between the elastic strain energy curve stored in the conical shell and the structural deformation (in terms of the height of the cone h) is of specific interest, as the local minimum points on the strain energy curve tell the possible stable states and how much deformation is required to reach those states. After locating each stable state, by equating the mechanical work done by the compressed air in the chamber and the elastic strain energy stored in the structure, the relationship between the driving pressure and the structure deformation can be derived. The obtained pressure-displacement relationship can then be analysed to obtain the critical pressure required to switch the structure from one state to another.

For model simplification, the conical shell is sliced into infinitely small sector with central angle $\delta\theta$ (see Fig. 3), where the slant surface in each slice are treated as a beam with varying cross-sectional area. Several assumptions are made during the consideration of this model: (i) Only the deformation in slant surface is considered. All other parts contribute zero internal volume change and store zero elastic strain energy; (ii) The material follows a linear and homogeneous model; (iii) The deformation process is treated as quasi-static.

Based on to the assumptions listed above, the slant undergoes an axial compression when the bistable state is switched. The amount of that compression can be derived from the Pythagoras' theorem:

$$\Delta l = L - \sqrt{(R-r)^2 + h^2} \tag{1}$$

where Δl is the amount of compression in this beam, L is the original slant length of the conical shell, R is the radius of the outer ring, r is the radius of the inner ring and h is the vertical displacement between the two rings.

When the amount of compression is not large enough to buckle the slant, there's only deformation due to the negative axial extension. The elastic energy due to this axial extension is given by [14]:

$$U_{axial} = \int_0^L \frac{F^2}{2EA(x)} dx \tag{2}$$

$$A(x) = \int_0^{2\pi} (r + x \cdot cos\alpha) t \cdot d\theta \tag{3}$$

where U_{axial} is the elastic energy stored due to the axial extension, x is the distance along the slant beam starting from the inner end, E is the Young's modulus of the material, $A(x)$ is the cross-sectional area of the slant beam, α is the slant angle made with the horizontal line, t is the shell thickness and F is the axial compressive force within the slant beam.

The relationship between this compressive force F and beam overall compression Δl is:

$$\Delta l = \int_0^L \frac{F}{EA(x)} dx \tag{4}$$

As the displacement of the structure keeps increasing, the amount of compression will eventually reach a certain point where buckling occurs. To find the exact amount of displacement required for triggering the buckling, Rayleigh-Ritz [14] method is used. Rayleigh-Ritz method is a energy-based method, stating that the critical point for buckling occurs when the mechanical work done by the compressive force equals the strain energy stored in the structure due to bending just after the buckling. The details about this statement are represented by Equation 5.

$$\int_0^L \frac{1}{2} EI(x) (\frac{d^2 w}{dx^2})^2 dx = F_c \times \Delta l \tag{5}$$

$$I(x) = \int_0^{2\pi} \frac{1}{12} (r + x \cdot cos\alpha) t^3 d\theta \tag{6}$$

where $I(x)$ is the second moment of area of the slant beam, w is the local deflection of the beam under bending and F_c is the critical compressive force within the beam at the point of buckling.

In order to apply Equation 5 into use, it is required to assume a buckling field $w(x)$. Our design comes with two thin-panel hinges located at both ends of the slant, these hinges undergo large rotation without causing too much bending moment. Therefore, the slant can be treated as a pin-ended structure, which has the following buckling shape:

$$w(x) = C[sin(\frac{\pi x}{L})] \tag{7}$$

This buckling shape is chosen as it brings zero bending moment at both ends. The C value in equation 7 as a function of the overall beam compression δl can be found by solving Equation 8. Equation 8 is derived by considering Pythagoras' theorem at each infinitely small segment of the beam and integrate the incremental axial extension over the entire beam length.

$$\Delta l = \int_0^L \frac{1}{2} (\frac{dw}{dx})^2 dx \tag{8}$$

By substituting Equation 8 into Equation 5, the buckling load can be found by the following equation:

$$F_c = \frac{\int_0^L \frac{1}{2} EI(x) (\frac{d^2 w}{dx^2})^2 dx}{\int_0^L \frac{1}{2} (\frac{dw}{dx})^2 dx} \tag{9}$$

After obtaining the critical axial load in the slant at the point of buckling, the corresponding deformation can then be obtained by:

$$\Delta l_c = \int_0^L \epsilon_c(x) dx = \int_0^L \frac{F_c}{EA(x)} dx \tag{10}$$

where Δl_c is the amount of compression exhibited by the beam at the critical point of buckling. By substituting Δl_c into equation 1, the critical vertical displacement at the point of buckling h_c can be obtained.

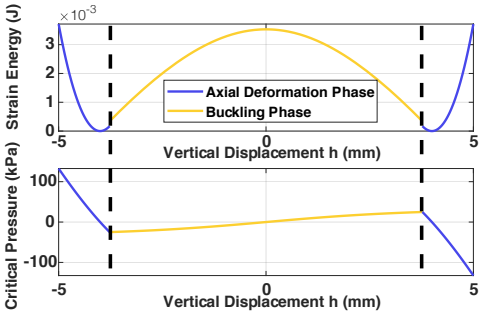


Fig. 4. The elastic strain energy stored $U(h)$ and the corresponding driving pressure $p(h)$ over structural deformation. The deformation is represented by the vertical displacement between the outer and inner edge of the conical shell, shown as h in Fig. 3. In this figure, the membrane material is chosen as 50A shore hardness. The membrane thickness is 1mm and the slope angle is 45^o. The Young's modulus used for this digital material is 1.65 MPa.

The elastic energy stored in slant after the buckling is due to the bending caused by the buckling shape. The amount of that elastic energy is obtained by Equation 5.

All equations stated above are sent into Matlab Symbolic Toolbox, and the relationship between the elastic strain energy and the structural deformation $U(h)$ can be obtained. When the structure is out of the calculated buckling range, the strain energy depends on the axial energy expressed in Equation 2. When the structure is within its buckling range (the amount of compression in the slant is larger than the threshold value), the strain energy is the sum of the energy due to bending (see Equation 5) and the accumulated axial elastic energy during the axial compression stage before buckling (the value of U_{axial} in Equation 2 when $F = F_c$). It is assumed that the tether connecting the two bistable shells have no deformation. This means the two shells come with the same elastic strain energy during the operation of the valve. Therefore, the total elastic strain energy is obtained by doubling the elastic strain energy of one single shell.

The relationship between driving pressure and structural deformation $p(h)$ is obtained based on the conservation of energy.That means the work done by the compressed air in the chamber equals the elastic strain energy stored in the structure, which leads to:

$$\int p(h) dV = U(h) \tag{11}$$

where $V(h)$ is the volume within the shell and $p(h)$ is the driving pressure required for different structure displacement. By taking differentiation of both sides in Equation 11, we have:

$$p(h) = \frac{\frac{dU(h)}{dh}}{\frac{dV(h)}{dh}} \tag{12}$$

Fig. 4 shows a typical strain energy curve and pressure-displacement curve. Two local minimum points are located on the strain energy curve, while each of them contribute to one possible bistable state. The critical pressure required to switch from one state to another is determined by the largest pressure value observed on the pressure-displacement curve within those two bi-stable states.

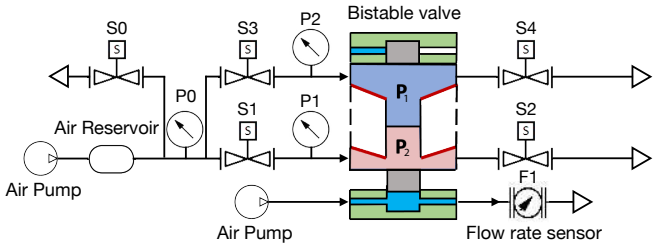


Fig. 5. Schematics of the pneumatic system used for characterization. P0, P1 and P2 stand for pressure sensor 0,1 and 2. S0,S1,S2,S3,S4 stand for solenoid valve 0,1,2,3 and 4. F1 represents the flowrate sensor. For valve activation, the two chambers of the bistable valve (P_1,P_2) are independently connected to the pressure system to achieve rapid pressure engagement and venting. To detect whether the air channel is blocked or not by the bistable valve, the controlled air channel (located at the bottom of the bistable valve) is connected with an air pump and a flow rate sensor.

IV. Experimental Setup and Protocols

In this study, critical switching pressure is evaluated to reflect the tunable characteristic of the bi-stable valve. The critical switching pressure is defined as the minimum pressure difference between two valve chambers required to switch the valve state. The valve response time is also measured as the time taken for the valve to complete the state switching process. The goal of the experimental characterization is to find out the critical pressure and response time of the valves under different design parameters, including the shell material hardness, the conical shell thickness, and the shell slope angle.

A. Experimental Setup and Basic Procedure

The setup of the conventional pump-valve system to perform the characterization is shown in Fig. 5. Two displacement pumps (SIMILK, mini air pump, rated airflow of 2 L/min) are used. One is used to set up the required driving pressure to either chamber of the valve, while the other pump is used to apply constant air flow to the controlled air channel. The driving pressure here is defined as the pressure applied to one of the valve chambers during our experiments. While as we stated before, the critical pressure is the minimum driving pressure required to switch the state of the valve. To achieve rapid pressure settling in the pressure chamber, smooth out fluctuation and avoid overshoots, a reservoir (rigid plastic, with the volume of 250 ml) is used. Multiple solenoid valves (VDW10AA, SMC) are used to engage and vent the driving pressure of each chamber. A volume flowrate sensor (MEMS D6F-P Flow Sensor, OMRON) connected in series with the controlled air channel is used to reflect whether the air channel is successfully blocked by the pneumatic signal. Three independent pressure sensors ($\pm$100 kPa, PSE 543-R06, SMC Corporation, Japan)) are used to monitor the pressure in the reservoir and the two valve chambers respectively. Control signals were generated, and data were captured using a data acquisition device (USB-6341, National Instruments) at 10kHz sampling rate.

For sample preparation, five batches of valve samples were fabricated. The sample key dimensions and post-processing technique are presented in Table I.

TABLE I
Experimental Sample Preparation

Batch (Quantity)	Design parameters			Support Removal
	S_A	t(mm)	$\alpha(^o)$	
A (5)	30, 40, 50, 60, 70	1	45	Chemical
B (7)	50	0.7, 0.8, 0.9, 1.0, 1.1, 1.2, 1.3	45	Chemical
C (7)	50	1	30, 35, 40, 45, 50, 55, 60	Chemical
D (6)	50	0.8	45	3x Chemical 3x Physical
E (2)	50	0.8	45	1x Chemical 1x Physical

*S_A refers to the ASTM D2240 type A hardness, t refers to the thickness of the conical shell. α refers to the slope angle of the conical shell. Chemical support removal refers to chemical bathing. Physical support removal refers to water-jetting. For all samples, the radius of the conical shell outer ring R is 8 mm, and the inner ring radius r is 4mm.

Algorithm 1: Procedure for measuring the critical pressure of a valve.

Result: 10kHz sampling data of pressure in reservoir ($P_{reservoir}$), pressure in both valve chambers (P_1, P_2) and volume flowrate in the controlled air channel ($Q_{controlled}$).

$P_{target} \leftarrow$ 1 kPa;
$\delta p \leftarrow$ 1 kPa for Batch A,B and C;
$\delta p \leftarrow$ 0.2 kPa for Batch D and E;
while $P_{critical}$ *not found yet* **do**
  Valve S1 to 5 $\leftarrow$ OFF;
  set $P_{reservoir}$ to P_{target} via a PID controller;
  Valve S4 $\leftarrow$ ON ;
  Valve S2 $\leftarrow$ ON ;
  Pause for 10 seconds;
  Valve S2 $\leftarrow$ OFF Valve S1 $\leftarrow$ ON ;
  Pause for 5 seconds;
  if $Q_{controlled} \leq$ *5 mL/min* **then**
    $P_{critical} \leftarrow P_{target}$;
  else
    $P_{target} = P_{target} + \delta p$;
  Valve S1 and 4 $\leftarrow$ ON; Pause for 5 seconds;
  Valve S1 and 4 $\leftarrow$ OFF;
Save $P_{reservoir}$,P_1, P_2 and $Q_{controlled}$

Batch A,B and C aims to find how the valve behaviour (critical pressure and response time) is affected by the three key design dimensions (shell material hardness, shell thickness, shell slope angle) respectively. Batch D aims to investigate the effect of different support-removal techniques on the valve behaviour. It also aims to investigate the consistency between each fabricated valve with the same dimensions. Batch E is used for fatigue tests aiming to examine the durability of the valve.

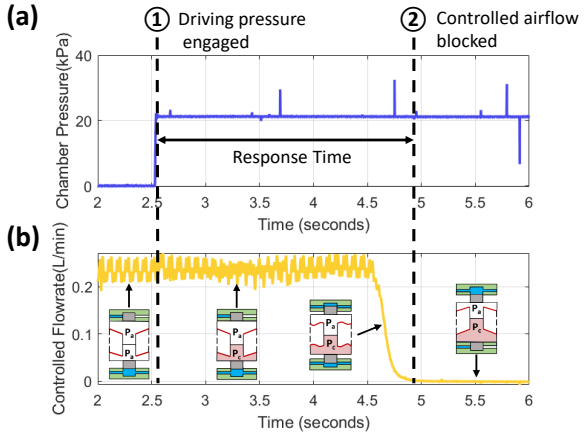


Fig. 6. This demonstrates how the response time is obtained from the time-series data. (a) shows the pressure in the chamber of the valve and (b) shows the volume flow rate of the controlled air channel. P_a refers to the atmosphere pressure while P_c refers to the critical pressure of the valve. "Driving pressure engaged" is defined when the pressure in the valve chamber reaches and stabilises at the desired level. "Controlled airflow blocked" is defined when the flow rate controlled reaches and stabilises at a level which is lower than 5mL/min. The response time is obtained by calculating the time difference between these two time stamps.

B. Experimental protocol of the critical pressure and response time characterization

For each sample in batch A,B,C and D, the critical pressure and response time were measured. The measurements were taken repeatedly (3 times for batch A,B and C; 5 times for batch D) with 0.5 hrs relaxation between each trial to ensure data reliability. The critical pressure is found empirically by applying a specific driving pressure (P_{target} in Algorithm 1) to one of the valve chambers and observing whether the valve state is successfully switched. Starting from a randomized initial value which is insufficient to switch the state of the valve, the driving pressure P_{target} is incrementally increased with a small step until the valve state is successfully switched. Note that the pressure in the valve chamber is reset to the atmosphere pressure after each trial to get rid of any hysteresis effect. As the valve comes with a completely symmetrical structure, the switching pressure at both switching direction are assumed to be the same, so the switching direction used during measurement is randomly chosen. The detailed procedure is shown in Algorithm 1.

The response time of the valve is defined as the total time required by the valve to shut down the controlled air flow after the engagement of that critical switching pressure. This is obtained by post-processing the time-series data obtained from the experiment. Fig. 6 shows how the response time is obtained from the raw time-series data.

C. Experimental protocol of the fatigue test

For each sample in batch E, fatigue tests are performed to examine the durability of the valves. The fatigue tests are preformed by repeatedly switch the valve state from one to another (shown in Algorithm 2) for 500 working cycles. To further challenge the reliability of the valves, the driving pressure used in fatigue test is set to 35 kPa, which is larger than the critical switching pressure. The response time during each working cycle is recorded. Meanwhile, the critical pressure before and after these fatigue tests are measured and recorded.

Algorithm 2: Procedure for fatigue tests.

Result: 10kHz sampling data of pressure in reservoir ($P_{reservoir}$), pressure in both valve chambers (P_1, P_2) and volume flowrate in the controlled air channel ($Q_{controlled}$).

$P_{target} \leftarrow$ 35 kPa;
for *trial number* $\leftarrow$ *1 to N* **do**
  Valve S1 to 5 $\leftarrow$ OFF;
  set $P_{reservoir}$ to P_{target} via PID;
  Valve S2 $\leftarrow$ ON ;
  Pause for 10 seconds;
  Valve S2 $\leftarrow$ OFF Valve S1 $\leftarrow$ ON ;
  Pause for 5 seconds;
  Valve S1 $\leftarrow$ OFF ;
  set $P_{reservoir}$ to P_{target} via PID;
  Valve S5 $\leftarrow$ ON ;
  Pause for 10 seconds;
  Valve S5 $\leftarrow$ OFF Valve S4 $\leftarrow$ ON ;
  Pause for 5 seconds;
  Valve S4 $\leftarrow$ OFF ;
  Save $P_{reservoir}$,P_1, P_2 and $Q_{controlled}$

V. Experimental Results

A. Results on Valve Behaviour over different design parameters

The effects of the design features on the critical pressure and response times are shown in Fig. 7. Overall, the experiment results show a similar trend with the theoretical model for material hardness, membrane thickness, and slope angle with an RMSE of 9.66, 7.68 kPa and 15.2 kPa, respectively. The Young's modulus of each digital material used in the theoretical modelling is obtained from [13, 15]. The theoretical model tends to underestimate the critical pressure when the critical pressure is relatively low, which may be caused by the frictional force exerted on the moving piston. Changing the material shore hardness achieves the largest adjustable critical pressure range (from 15.3 to 65.2 kPa with a maximum-minimum ratio of 4.26) among the three features. In contrast, changing the shell thickness can adjust the critical pressure from 18.6 to 48.5 kPa (a maximum-minimum ratio of 2.61) and hanging the slope angle can adjust the critical pressure from 19.8 to 38.3 kPa (a maximum-minimum ratio of 1.93).

Fig. 7(d) indicates that the response time decreases as the material Young's Modulus increases. When tuning the shell thickness, the response time reaches its minimum value at around 1mm. No clear trend was found between the response time and the slope angle. Although all three design dimensions successfully adjusted the critical switching pressure, they come with different performance in terms of consistency. Changing the slope angle brings a large RMSE (15.2 kPa) between the predicted and experimental results. It also brings a large standard deviation (0.752 s) on response time (shown in Fig. 7 (d),(e),(f)) compared to an average of 0.404 s STD for material

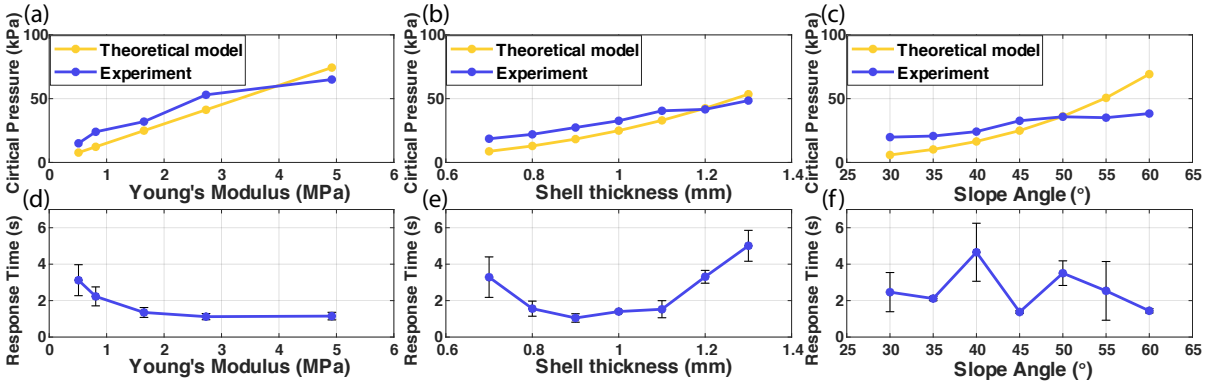


Fig. 7. The measured critical pressure of the valves with different shell Young's Modulus **(a)**, shell thickness **(b)**, and shell slope angle values **(c)**. The prediction given by the theoretical model is plotted in the same graph for comparison. The measured response time of the valves with different shell material Young's Modulus **(d)**, shell thickness **(e)**, and shell slope angle values **(f)**. The error bar indicates the standard deviation over three repeated trials of the same valve. The switching direction during measurement is randomly chosen.

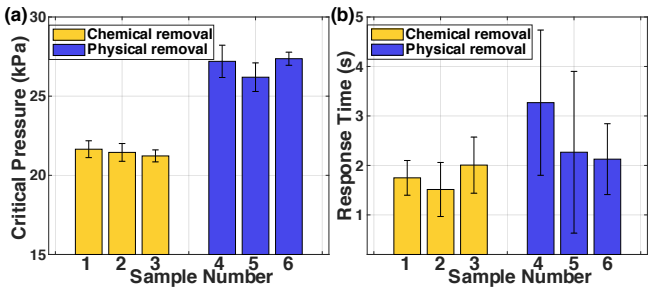


Fig. 8. The repeatability test of multiple valve samples with identical design parameters. Sample 1-3 are post-processed through 12 hrs chemical bathing, while sample 4-6 are post-processed through water-jetting. The **(a)** critical pressure and (**b**) response time of all six samples are presented. The error bar indicates the standard deviation of each sample over five trials. The switching direction during measurement is randomly chosen.

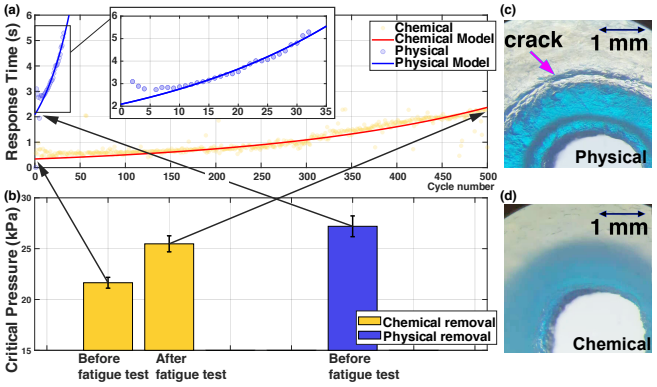


Fig. 9. Fatigue tests for valves whose support materials were removed by chemical bathing or physical method. **(a)** Measured response times at each trial. Note that the response time here is measured when the driving pressure is 35 kPa. Exponential models are used to fit the empirical data. (**b**) Measured critical switching pressure and corresponding response time before and after the fatigue tests. The error bar indicates the standard deviation of each sample over five trials. After five cycles of fatigue test, small cracks on the sample post-processed with physical support removal can be observed in comparison to the sample post-processed with chemical bathing, shown in **c** and **d**, respectively. Both figures were captured using an optical microscope.

stiffness change and 0.499 s STD for membrane thickness change. Part of the reasons for its poor consistency is that changing the slope angle brings significant change to the overall geometry and size of the valve. We recommend using material hardness to adjust the critical pressure to suit different needs, as they bring a smaller RMSE between the theoretical model and the experiment results. Tuning the material hardness can also reduce the valve response time, while Fig. 7(d) shows the fastest average response time ($\leq 1.8s$). The response time of the valve is considerably larger than the response time of the silicone cast soft fluidic valve (0.4 s) [7] or conventional solenoid valve (30-200 ms).

B. Results on Valve Behaviour and Consistency over different post-processing method

The repeatability test shows a significant performance difference between valves with chemical and physical post-processing methods. As shown in Fig. 8, removing the support with chemical bathing decreased the critical switching pressure by 20.36% and reduced response time by 31.23%. The decrease in critical pressure after chemical support removal is due to some material property changes brought by the bathing process. It is also found that the samples with physical support removal technique come with poorer model consistency, especially in terms of the response time. The inconsistency is mainly caused by the tiny cracks on the surface of the compliant conical shells brought by the high pressure water jets. The generation of these cracks are highly unpredictable and irregular, therefore bringing a large inconsistency between different samples. The size of these cracks may also keep growing during each measurement, therefore bringing inconsistency between different trials even for the same sample. The large deviation in response time of these valves could bring design constraints and problems when controlling the soft robots which require constant-frequency periodic actuation or fast response to the environment.

C. Results on Fatigue Tests over different post-processing method

The critical pressure increases with the increase of trial numbers during the fatigue test. Better performance of samples post-processed with chemical bathing is found with less critical pressure change and a pass of the fatigue test. The sample post-processed with physical support material removal

failed earlier after 32 complete cycles. This shorter life cycle is caused by the tiny cracks generated by the high-pressure water jets on the surface of the compliant conical shell (see Fig. 9(c) and (d)). These cracks gradually increase their size during the loading cycles and eventually breaks the shell and results in a leakage.

An exponential model trained from the experiment data is used to further characterize the fatigue behaviour of the valve, as shown in Fig. 9. For the valve which uses chemical support-removal technique and physical support-removal technique, the fitted model are:

$$T = 0.341 \times e^{0.00388 \cdot n} \tag{13}$$

and

$$T = 2.09 \times e^{0.0280 \cdot n} \tag{14}$$

where T is the response time and n is the number of working cycles undertaken by the valve.

VI. Conclusion

This paper presents a 3D printed bistable pneumatic valve design with a method to tune the critical pressure with predefined design parameters. Inspired by the structural buckling of two conical bistable shells, the design utilizes multi-material 3D printing technology to create an electronics-free valve that embeds a pneumatic signal as input to control the state of connected air channels. A theoretical model was included to investigate the bistability and snap-through behaviour of the valve. The two local valleys observed on the strain energy curve reflect the bi-stable nature of the structure. The bistability of the valve ensures that no constant energy supply is required to maintain the state of the valve. Meanwhile, the pressure-displacement curve predicted the critical switching pressure required to switch the valve state.

The experiment characterization further verifies the theoretical modelling results, showing that the critical switching pressure of the valve can be easily tuned within the range from 15.3 kPa to 65.2 kPa by adjusting the thickness, the slope angle and the material hardness of the conical shell in the valve design. This design flexibility and fast fabrication solution with 3D printing indicate the valve can be used as a digital valve that takes digital pneumatic signal as input and a comparator that deals with analogue pneumatic signal computation. The light-weight and electronics-free nature of the valve allows it to be embedded in untethered soft robots, even in challenging environments where a conventional electronic system cannot be used. Thanks to the advantages of soft material 3D printing, the valve requires minimal manual work during its fabrication and component integration. The valve can be used to build logical gates, analogue-to-digital converters, and digital memory in future work. Although the critical switching pressure of the valve is characterized and presented by the design dimensions, the response time of the valve still requires more investigation. Compared with traditional mechanical valves, the 3D printed soft membrane (Agilus30) used in this work introduces higher viscous losses, increasing the response time. The valve also exhibits performance change after a large number of working cycles. In future studies, solutions that can increase the durability and reduce the response time of the valve will also be investigated.

References

[1] Chiwon Lee et al. “Soft robot review”. In: *International Journal of Control, Automation and Systems* 15.1 (2017), pp. 3–15.

[2] James Walker et al. “Soft robotics: a review of recent developments of pneumatic soft actuators”. In: *Actuators*. Vol. 9. 1. Multidisciplinary Digital Publishing Institute. 2020, p. 3.

[3] Hiroaki Tanaka, Tsung-Yuan Chen, and Koh Hosoda. “Dynamic turning of a soft quadruped robot by changing phase difference”. In: *Frontiers in Robotics and AI* 8 (2021), p. 93.

[4] Liang He et al. “A method to 3D print a programmable continuum actuator with single material using internal constraint”. In: *Sensors and Actuators A: Physical* 324 (2021), p. 112674.

[5] Yichao Tang et al. “Leveraging elastic instabilities for amplified performance: Spine-inspired high-speed and high-force soft robots”. In: *Science Advances* 6.19 (2020), eaaz6912.

[6] Liang He et al. “Soft fingertips with tactile sensing and active deformation for robust grasping of delicate objects”. In: *IEEE Robotics and Automation Letters* 5.2 (2020), pp. 2714–2721.

[7] Philipp Rothemund et al. “A soft, bistable valve for autonomous control of soft actuators”. In: *Science Robotics* 3.16 (2018).

[8] Dylan Drotman et al. “Electronics-free pneumatic circuits for controlling soft-legged robots”. In: *Science Robotics* 6.51 (2021).

[9] Kai Luo et al. “Soft kink valves”. In: *Journal of the Mechanics and Physics of Solids* 131 (2019), pp. 230–239.

[10] K. Xu and N. O. Pérez-Arancibia. “Electronics-Free Logic Circuits for Localized Feedback Control of Multi-Actuator Soft Robots”. In: *IEEE Robotics and Automation Letters* 5.3 (2020), pp. 3990–3997.

[11] Jahan Zeb Gul et al. “3D printing for soft robotics–a review”. In: *Science and technology of advanced materials* 19.1 (2018), pp. 243–262.

[12] Saeed Akbari et al. “Enhanced multimaterial 4D printing with active hinges”. In: *Smart Materials and Structures* 27.6 (2018), p. 065027.

[13] Viacheslav Slesarenko and Stephan Rudykh. “Towards mechanical characterization of soft digital materials for multimaterial 3D-printing”. In: *International Journal of Engineering Science* 123 (2018), pp. 62–72.

[14] Thomas Henry Gordon Megson. *Structural and stress analysis*. Butterworth-Heinemann, 2019.

[15] Lei Liu and Yaning Li. “Failure mechanism transition of 3D-printed biomimetic sutures”. In: *Engineering Fracture Mechanics* 199 (2018), pp. 372–379.

3.6 Supporting Information

3.6.1 Supporting Video

A video summarizing the work can be found here: `https://youtu.be/40t8UxduZZ8`

3.6.2 CAD files

The CAD files of the 3D printed bistable valve can be found in the following Github repository: `https://github.com/sihanwang0318/3D-printed-Bistable-Valve-CAD-File.git`

4

Modular 3D-printed Multi-channel Valves

Contents

4.1 Problem 45
4.2 Objective 46
4.3 Key contributions 46
4.4 Summary of results 47
4.5 Contributed Paper 47
4.6 Supporting Information 56
4.6.1 Supporting Video 56
4.6.2 CAD files 56

4.1 Problem

The work presented in Chapter 3 successfully exploits multi-material 3D printing to develop a pneumatically-driven bistable valve. However, a limitation is that each valve can only control one single actuator between two states (ON and OFF). The same problem can be observed in other state-of-art work in the community [8, 69], such as the silicone bistable valve discussed in Section 2.2.2 or the 3D printed pneumatic transistors discussed in Section 2.2.3. All these pneumatic devices are fundamentally single-channel valves controlling one pneumatic chamber between two digital states. However, modern soft robots come with an increased number of

chambers and DoFs for enhanced functionality. These more complex soft robotic systems demand pneumatic control devices that can simultaneously control multiple channels or chambers. Suppose only traditional 2/2 way valves are implemented, the onboard pneumatic circuits have to be equipped with a large number of valves, which severely increases the overall size, weight, and power consumption of the robots.

4.2 Objective

The objective of this work is to modify our previous work described in Chapter 3 and develop a set of modular multi-channel valves (3/2, 4/2 and 5/2 way valves), aiming to decrease the number of units required in the pneumatic circuits for controlling soft robots with multiple pneumatic actuators.

4.3 Key contributions

The contributions of this work are as follows:

- By introducing the multi-channel compatibility into the 3D-printed bistable valve, the number of units required when controlling multi-DOF soft robots is significantly decreased. This lowers the system size/weight while reducing the energy consumed by the circuit.

- The modified 3D-printed spool/cylinder mechanism comes with a much higher breakthrough pressure compared with other works [8, 69], ensuring its compatibility with those high-pressure soft actuators [109].

- The multi-channel valves can be used in any soft pneumatic robots that behave as finite-state machines. Such robots can be used in numerous applications such as object sorting (demonstrated in this work), legged locomotion [68], crawling [110], multi-modal gripping [111], and so on.

4.4 Summary of results

This paper presents a modular approach to designing multi- channel bistable valves for pneumatically driven soft robots based on Multi-material 3D printing. Different multi-channel valve units (3/2 way, 4/2 way, and 5/2 way) are designed to provide varieties in the pneumatic circuit design. The experimental results verify that the proposed multi-channel valves successfully perform the desired function without leakages or "cross-talking" between air channels. The valves can be switched by pneumatic signals ranging from 48.6 kPa to 65.4 kPa. The valves can withstand a pressure of up to 187.2 kPa without leakages, which is sufficient for most soft robotic applications. The air channels in these valve units come with an average sonic conductance of 0.04 lpm/kpa and an average critical pressure ratio of 0.38. For demonstration, the multi-channel valves were used to control a bi-directional actuator through four different positions, performing an object sorting task.

4.5 Contributed Paper

The work has been published as a journal paper in IEEE Robotics and Automation Letters (RA-L) and invited to present at an oral session at the International Conference on Robotics and Automation (ICRA 2022). The paper is attached on the following pages.

A Modular Approach to Design Multi-channel Bistable Valves for Integrated Pneumatically-driven Soft Robots via 3D-printing

Sihan Wang[1], Liang He[1*] and Perla Maiolino[1]

***Abstract*—A pneumatic system that transmits power via the force of compressed air is an essential component of an air-driven soft robot. Pneumatic valves are one of the key parts of this system. However, the development of soft or electronics-free valves for soft robotic applications is in its infancy, with only a few 2/2 way valves developed. Previous research has shown demands for a complex pneumatic system that can regulate the airflow in multiple channels or switching the pressure within a chamber between multiple states. Hardware redundancy is found in such complex pneumatic circuits if only 2/2 way valves are available for the system design. To increase the design freedom, this paper presents a modular approach that integrates multi-channel modular valve units and bi-stable structures for the conversion of pneumatic signals. By utilising soft-material 3D printing, the 3/2-way valve, 4/2-way valve and 5/2-way valve design are proposed in this paper to control multiple air channels simultaneously. The modular design of these 3D printed multi-port valves allows quick design and fabrication solutions of a complex electronics-free pneumatic system by reassembling different modular units of the valve. Experiment characterization of the multi-channel valves shows maximum allowable pressure at 187.2 kPa and a flow rate of 7.42 L/min under 50 kPa pressure loss. A demonstration of controlling four states of a dual-chamber soft robotic arm with only two modular multi-chamber valves was included, showing reduced valve units and overall weight compared to conventional electronics-free 2/2 way valves.**

***Index Terms*—Soft Robot Applications, Additive Manufacturing, Hydraulic/Pneumatic Actuators**

I. Introduction

PNEUMATIC soft robots make use of the interaction between compressed air and soft elastomeric materials to achieve high adaptability and compliance. This mechanism has drawn attention from many researchers due to various advantages, including low cost, flexible manufacture choices, safe human-robot interaction and adaptability to environments or objects with unknown kinematics or dynamics [1]. These valuable characteristics lead to the development of various pneumatic actuators with different structures, motion, pressure ranges, and fabrication methods [2, 3]. However, the control of these actuators requires complex pneumatic systems which consist of rigid solenoid valves, electric pumps, and conventional electronic controllers [4, 5, 6]. The existence of these tethered external rigid pressure systems significantly limits these robots' mobility and application fields, especially for those soft robots designed for extreme environment operations (e.g., nuclear plant exploration with high-radiation, tissue interaction during metal-free scenarios in magnetic resonance imaging). Another limitation is sensory information processing. In many applications, the conversion of pneumatic sensory information into an electrical signal before being processed back to a pneumatic signal for control brings additional system complexity and limits the application in extreme conditions.

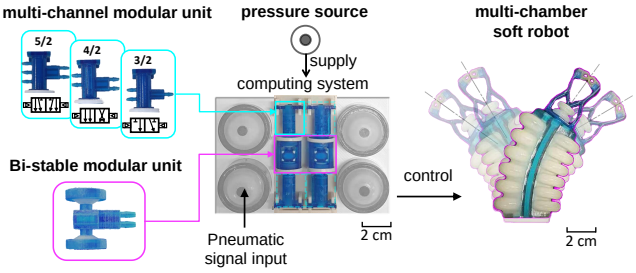


Fig. 1. The modular design of the 3D-printed multi-channel valves for controlling soft robots. Three types of multi-channel-valve modular units (3/2 way valve, 4/2 way valve and 5/2 way valve) are designed to control the flow of pneumatic signals. A bistable modular unit with a pneumatically-driven bistable structure is used to take input from pneumatic signals to operate the attached multi-channel valve unit. A computing system can be made by attaching the desired multi-channel valve units to a certain number of bistable units. The computing system distributes the energy obtained from constant pressure resources to a multi-chamber soft robots to control its actuation, based on the pneumatic signal input.

These existing limitations make the development of electronic-free valves a critical contribution to the future of fully soft robots required in extreme environments. This encouraged many researchers to develop various soft or electronics-free devices to compute and regulate the pneumatic signal and power for soft robots. One typical work is a soft valve that makes use of a semi-spherical bistable structure and two pairs of kinking tubes [7]. This design uses a passive bi-stable membrane driven by external pressure to press and make the internal tubing buckle, therefore regulating the flow based on the input pneumatic signal. [8] also developed three different soft switch valves (a normally-open valve, a normally closed valve and a hysteretic valve) to control the locomotion

Manuscript received: September, 08, 2021; Revised December, 17, 2021; Accepted January, 24, 2022.

This paper was recommended for publication by Editor Kyu-Jin Cho upon evaluation of the Associate Editor and Reviewers' comments. This work was supported by the Engineering and Physical Sciences Research Council (EPSRC) Grant EP/V000748/1; S. Wang was supported by the CSC-PAG Oxford Scholarship for his DPhil study.)

[1]Authors are with the Oxford Robotics Institute, University of Oxford, UK sihan.wang/liang.he/perla.maiolino@eng.ox.ac.uk

*Corresponding Author: Liang He

Digital Object Identifier (DOI): see top of this page.

of a soft crawler. These valves are made of soft tubes which are adhered to the skin of the robots. The linear deformation of the actuators is used to kink the tubes and therefore regulate the flow, while a bistable membrane provides the hysteresis. More recently, with the development of multi-material 3D printing technology, [9] designed a set of fully 3D printed fluidic circuit elements including fluidic diodes, "normally closed" valves, and "normally open" valves with tunable pressure-gain ranging from 0.67 to 2.

All those electronics-free valves described above are fundamentally 2/2 or 3/2 way valves with only two or three ports forming one single air channel and two corresponding states (blocked and unblocked). More valves are needed when the system requires multiple independent-controlled signals: a) one valve is used to control one single chamber gripper or one single chamber crawler [7]; (b)three valves are used to control the locomotion of a three-chamber crawler [8]; (c) three valves are used to control three independent fingers of a robotic hand [9]. (d) four valves are used to control the oscillating actuation of a two chamber soft turtle [9]. Soft robots developed from previous research have greatly demanded a pneumatic system that can regulate the airflow in multiple channels or chambers based on a single input signal. For example, the bi-directional actuator requires one chamber inflated and the other deflated [10]. A soft legged robot with a diagonal couplet gait pattern also requires opposite actuation for the two diagonal pairs of feet [11]. Suppose only traditional 2/2 way valves are implemented, complex pneumatic circuits have to be designed with many valves, which severely increases the overall size, weight, and power required for computation and system complexity.

An industrial solution to direct air from different sources to different chambers is the Directional Control Valve (DCV), which consists of a spool inside a cylinder to restrict/permit the air flow in different air channels [12]. However, these industrial valves' material, size, weight, and cost limit their applications in untethered electronics-free soft robots. More recently, the advance of additive manufacturing allows the design of 3D printed directional control valves [13]. However, the development is still in its infancy. According to the experiments, the use of single-material 3D printing brings inevitable leakage, resulting in at least 3% pressure loss [13]. This can be solved by introducing soft seals with a multi-material 3D printer.

Valves with multiple channels were also exploited from the microfluidics community. [14] designed a rotary planar bistable multi-port valve that successfully regulates the flow in 5 separate fluidic channels, yet incorporating a stepper motor that limits the size and overall weight of the system. The first electronics-free multi-channel valve successfully embedded in an untethered soft robot was designed by [11]. The valve in [7] was modified by adhering two (rather than one) fluid lines to either side of the bistable membrane so that the valve can be used as a 4/2 way valve. One limit of this work is the leakage brought by its kinking tube mechanism when the controlled chamber has a high operation pressure. The fabrication of the valve also requires significant manual work.

Thus, this paper presents a method for 3D printing modular multi-channel valves for complex pneumatic circuit design (Fig. 1). By rapid manufacturing soft bi-stable structures, the design of 3/2-way, 4/2-way, and 5/2-way valves are proposed to control multiple air channels in soft robots. These valves of 50 mm x 18 mm x 18 mm have a breakthrough pressure of 187.2 kPa and a flow rate of 7.42 L/min under 50 kPa pressure loss. Finite element method (FEM) is used to validate the design of the valve in terms of sealing performance. The modular approach to fast integrate multiple valves and to program advanced logical gates for multi-channel soft robots is demonstrated with a bi-directional soft robotic manipulator.

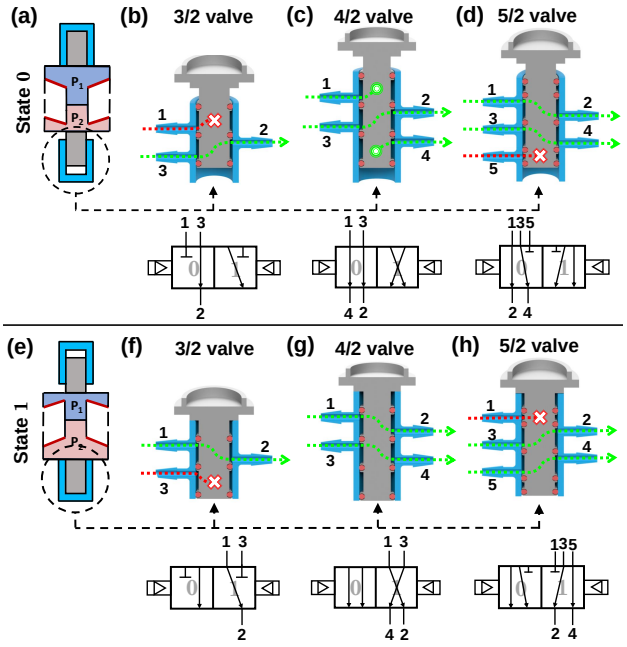


Fig. 2. Design and operating principles for 3D printed multi-channel valves. The overall structure of these valves is shown in **(a)** and **(e)**. All types of multi-channel valves include the same bistable modular unit in the middle. The structure consists of two symmetrically oriented bistable conical shells (shown by solid red lines). The two conical shells are tethered by unstretchable connectors (shown by black dotted lines) so that there's always one shell in "expanded" state and the other shell in "contracted" state. The state of the bistable structure can be switched between State I and State II by applying positive pressure to chamber P_1 or P_2. A spool with soft seals (shown in grey) is attached to each end of the central bistable structure and is placed in a cylinder (shown in blue), controlling the opening and closing of multiple air channels based on the state of the bistable structure. The 3/2, 4/2 and 5/2 way valve unit each comes with a unique spool and spool cylinder, with the geometry and working principle presented in **(b)** and **(f)**, **(c)** and **(g)**, **(d)** and **(h)**, respectively. The logical symbol of each valve at each state is placed below each corresponding spool and cylinder pair.

II. Design and Fabrication of the 3D Printed Directional Control Valve

A. Modular design of the multi-channel bistable valve

The operation of the valve makes use of a bistable structure to eliminate the need for a continuous signal. The bistability of the structure comes from two symmetrically oriented conical chambers (shown in Fig. 1). The states of the chamber can be switched from one state to another by applying a pneumatic signal (positive pressure) to one of the chambers. The state of the bistable structure determines the position of a spool in

its cylinder, which has multiple spool seals distributed along its axial direction. The seals fit between the spool and the cylinder and prevent air from going through. This means that the space between the spool body and the cylinder is divided into multiple isolated regions so that different air channels can be restricted or permitted. By changing the location of each seal along with the spool and each port along with the cylinder, we designed a "3/2 way valve", a "4/2 way valve," and a "5/2 way valve" to suit different applications."3","4" and "5" respectively indicates the total number of ports on the spool cylinder and the number "2" refers to the number of states of the valve.

Fig. 2 shows the switching stroke for the valves. The bistable "State 0" and "State 1" of the valve are shown in Fig. 2 (a) and (e). Once sufficient pressure is applied to the top shell P_1, the top shell will be switched to an "expanded" state. Due to the restricted length of the tether (black dashed line in Fig. 2(a)), only one shell can be in the "expanded" state at one time, which means the bottom shell will be pulled to its "contracted" state. To switch the valve back to "State 1", a positive pressure is applied to the bottom chamber P_2. In "State 1", the connection status of the controlled air channels in 3/2, 4/2 and 5/2 way valves are shown in Fig. 2(f)(g)(h). In "State 0", the connection status of the controlled air channels in 3/2, 4/2 and 5/2 way valves are shown in Fig. 2(b)(c)(d). One should note that all ports, spools and the spool seals were placed on both sides of the valves in a symmetrical manner, therefore bringing the valves a completely symmetrical structure and behaviour. Fig. 2 only shows the air channels located inside the bottom of valves to ensure simplicity and ease of reading.

B. Fabrication

The use of a multi-material Polyjet 3D printer (J735, Stratasys Ltd, USA) allows both rigid and soft materials to be implemented in the design. The materials used by the printer are Vero© and Agilus30©. Vero is a rigid plastic-like material with a quoted tensile strength of 50-65MPa, a Young's Modulus of 2200 MPa and a shore hardness of 83-86D. Agilus30 is a soft and rubber-like material, which has a quoted tensile strength of 2.1-2.6MPa, a Young's Modulus of around 1MPa and a shore hardness of 30A (Stratasys Ltd.). The compliant conical shells (shown as solid red lines in Fig. 2(a)(e)) and the spool seals are printed by pure Agilus30. The support material used during printing is SUP 706 (J735, Stratasys Ltd, USA), which can be chemically removed by placing the printed components in a tank (GEMINI SSR-550) filled with chemical support removal solution (0.02 kg/L Sodium Hydroxide and 0.01 kg/L Sodium Metasilicate).

C. Finite Element Modelling of the channels

One key component in this design is the seals on the spool printed by compliant material, as it supposes to regulate the airflow into different ports with minimum leakage. Therefore, we performed FEA simulations to validate the spool design. The simulations were performed using COMSOL Multiphysics 5.6 (COMSOL Inc., Sweden). The CAD model of the

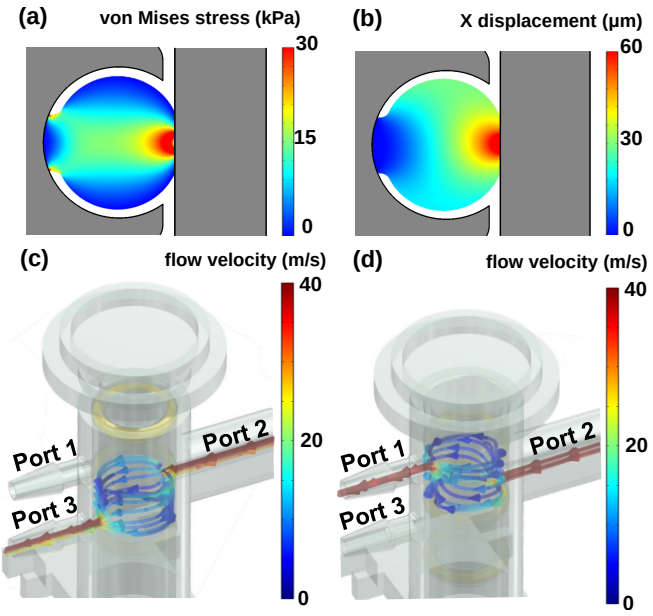


Fig. 3. FEM results of the multi-channel valve unit. **(a)** shows the stress distribution of the spool seal during operation. **(b)** shows the displacement distribution of the spool seal. The fluid dynamics simulation of the airflow in the valve under both states are presented in **(c)** and **(d)**.

spool and cylinder of the 3/2-way-valve unit was imported into COMSOL. Distinct material properties were then set to each material used by the design. Specifically, the spool seals were modeled as Agilus30 (E = 0.51 MPa;ρ = 1.15×10^3 kg/m^3; v = 0.49), while the spool body and cylinder were modeled as Vero (E = 2495 MPa; ρ = 1.18×10^3 kg/m^3; v = 0.375) [15]. Two simulations were implemented, whose procedures are as follows:

The first simulation aims to find the deformation and stress distribution of the spool seal. This simulation is performed in a 2D manner using the COMSOL Multiphysics "Solid Mechanics" module with a "Stationary" study. The rigid spool body is assigned as a "fixed" constraint, and a uniform boundary load is applied to the spool cylinder, therefore compressing the compliant piston seal. The boundary load is incrementally increased from zero until the inner surface of the spool cylinder reaches the actual fabricated diameter. "User-controlled mesh" calibrated for "General Physics" with a maximum element size of 0.02 mm is used for meshing. The obtained stress distribution and the deformation of the piston seal are presented in Fig. 3(a) and (b), respectively. Maximum von Mises stress within the seal is 28.7 kPa.The internal stress and deformed shape of the seal guarantees a seamless engagement between the spool seal and the cylinder, therefore eliminating the leakage. The second simulation aims to validate the value spool design for flow regulation and investigates the detailed flow pattern inside the valve. This simulation is performed in a 3D manner using the COMSOL Multiphysics "Single Phase Laminar Flow" module with a "Stationary" study. Port 2 is set as an "inlet" with a pressure of 10 kPa, while and the other two ports are set as "outlet".

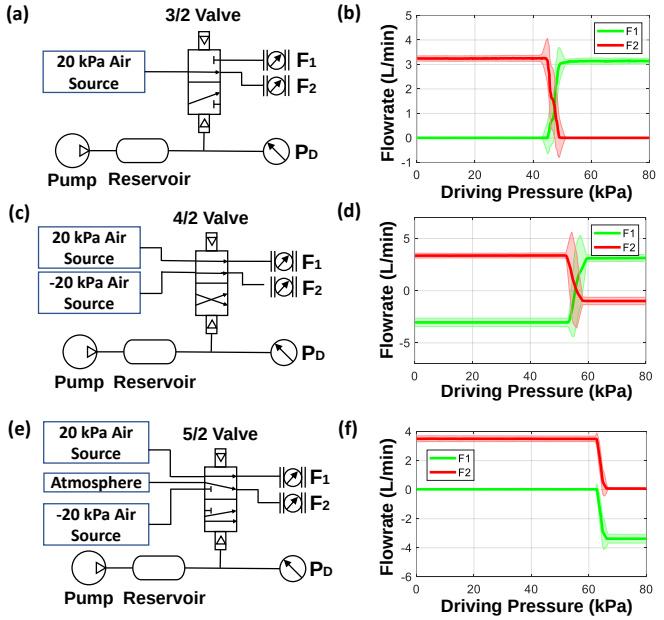


Fig. 4. **(a)**, **(c)**, and **(e)** show the experimental setup for measuring the switching behaviour of the 3/2 way, the 3/2 way, and the 5/2 way valve, respectively. P_D represents the driving pressure used to switch the state of the valve. The volume flow rate at both output ports are measured by flow rate sensor F_1 and F_2. **(b)**, **(d)**, and **(f)** show how the output flow rate changes as P_D increases through the 3/2 way, the 4/2 way, and the 5/2 way valve, respectively. The volume flow rate at all output ports are measured by flow rate sensor F_1 and F_2. The pressure applied at both input ports, P_{s1} and P_{s2}, are set to 20 kPa and -20 kPa respectively. The shaded errorbar represents the standard deviation of 5 independent trials.

All other surfaces in the model are assigned as the "wall" constraints. The material inside the valve air channel is modelled as air at room temperature. "User-controlled mesh" calibrated for "Fluid dynamics" with a predefined "fine" element size is used for meshing. The obtained velocity field of the airflow under both State 0 and State 1 are presented in Fig. 3(c) and (d). The simulation shows that the flow rate is 1.68 L/min and 1.72 L/min for State 0 and 1, respectively, when the pressure loss across the valve is 10 kPa. The flow pattern in both State 0 and State 1 shows that the position of the spool in the cylinder successfully regulate the airflow as desired.

III. Experiments and Results

A. Switching behaviour of the valve

The valves designed in this work take a pneumatic signal as input to switch its state. The experiments presented in this section aims to investigate the performance of its switching behaviour. The experimental schematics and results are shown in Fig. 4.

As presented in Fig. 4(a)(c)(e), air sources with different constant pressure are connected to specific ports of the 3/2, 4/2 and 5/2 way valve, respectively. Each air source used consists of an air compressor (BB50D, BAMBI AIR COMPRESSORS LTD, with integrated reservoir), a pneumatic filter (AF20-F02-A, SMC) for contaminant removal and a pressure regulator (AR20-F02-1-B, SMC) for controlling the pressure applied to the valve ports. To continuously monitor the switching behaviour of the valve, flow rate sensors (HAF 20SLPM AIR, Honeywell) are connected in series to all other valve ports. The changes in the measured volume flow rate indicate the change in the valve state. The input pneumatic signal used to switch the state of the valve P_D is provided by a pneumatic system including a displacement pump (mini air pump, rated airflow of 2L/min, SIMILK), a solenoid valve for venting (VDW10AA, SMC), a pressure sensor (ADP5160, Panasonic) and a reservoir (rigid plastic, with the volume of 250 ml) for pressure stabilization. The valve driving pressure P_D is increased slowly from 0 to 80 kPa at a rate of 1 kPa/s through a PID controller. All sensory data are captured through Teensy 4.1, whose sampling rate is set at 5 kHz. The measurements were taken repeatedly 5 times with 0.5 hrs relaxation between each trial to get rid of any hysteresis effect and ensure all valves are measured in a consistent manner. The results are presented in Fig. 4(b)(d)(f). The switching behaviour consistency of this bistable structure under continuous operation (switching at 0.2 Hz) has been tested in our previous work [16].

As shown in Fig. 4(b)(d)(f), the measured flow rate curve demonstrates that all three valves successfully perform the desired function without "cross-talking" caused by the leakage. The critical pressure required for valve switching increases with the number of valve ports (48.6 kPa for 3/2 way valves, 55.5 kPa for 4/2 way valves and 65.4 kPa for 5/2 way valves). This is due to the increased friction between the piston and the piston cylinder as the number of piston seals goes up. In terms of consistency, the standard deviation in critical switching pressure between the 5 independent trials on the 3/2, 4/2 and 5/2 way valves are 2.1 kPa, 1.98 kPa and 1.4 kPa, respectively.

B. Valve flow rate Characterization

Volume flow rate plays a significant role in the performance of the valves, as it determines how fast the pneumatic actuators connected to them can be activated or deactivated. Therefore, the flow rate characterization experiments were implemented to determine the volume flow rate in each valve channel versus the pressure drop across the valve.

To do the characterization, we connected all channels in the valves to a variable-pressure source and measured 1) the volume flow rate through each valve channel; and 2) the pressure drop across the valve. The flow rate is measured by connecting a digital airflow sensor (HAF 20SLPM AIR, Honeywell) in series with the valve channel. The pressure drop across the valve is measured by placing two pressure sensors (ADP5160, Panasonic) at the upstream and downstream of the valve channel, respectively. Each valve comes with two states, so the characterization was implemented for all opening channels under both valve states. The measured flow rate versus pressure drop relationships were then used to fit the mathematical model stated by ISO 6358 [17] and used in the community [18] (see Equation 1 and 2). The experimental results and the fitted models were presented in Fig. 5 and

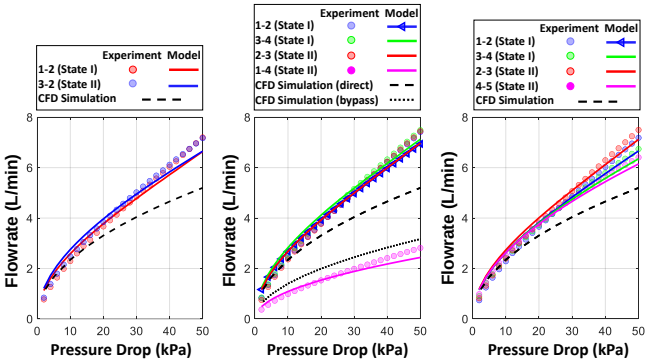


Fig. 5. Flow rate characterization of the air channels in the 3/2 way valves **(a)**, 4/2 way valves **(b)** and 5/2 way valves **(c)** under both of their states. CFD simulation results are presented for comparison. The experiment data are presented in circular dots, while the fitted models are presented in solid lines.

TABLE I
THE MEASURED SONIC CONDUCTANCE AND CRITICAL PRESSURE RATIO AT CHOKED POINT OF EACH CHANNEL OF THE VALVES UNDER BOTH STATES.

3/2 Valve	Channel	C	b	*Sonic conductance C and critical pressure ratio at choked point b is presented. The unit of C is "lpm/kPa". The percentage deviation is obtained by dividing the standard deviation by the mean value of the corresponding quantities.
	1-2 (I)	0.0450	0.355	
	3-2 (II)	0.0472	0.386	
	Deviation	3.37%	5.92%	
4/2 valve	Channel	C	b	
	1-2 (I)	0.0472	0.334	
	3-4 (I)	0.0480	0.391	
	2-3 (II)	0.0487	0.290	
	1-4 (II)	0.0163	0.548	
	Deviation	39.56%	28.84%	
5/2 valve	Channel	C	b	
	1-2 (I)	0.0457	0.354	
	3-4 (I)	0.0445	0.401	
	2-3 (II)	0.0498	0.286	
	4-5 (II)	0.0432	0.441	
	Deviation	6.23%	17.9%	

Table I. The simulation results from CFD analysis are also included for comparison.

$$Q = C\Psi P_{high} \tag{1}$$

$$\Psi = \begin{cases} \sqrt{1 - (\frac{\frac{P_{Low}}{P_{High}} - b}{1-b})^2} & \frac{P_{low}}{P_{high}} \geq b \\ 1 & \frac{P_{low}}{P_{high}} < b \end{cases} \tag{2}$$

where Q is the volume flow rate inside the valve channel, P_{high} is the absolute pressure at the valve upstream, P_{low} is the absolute pressure at the valve downstream, C and b are the parameters which needs to be fitted and they represent sonic conductance and critical pressure ratio at choked point respectively.

It can be seen from Fig. 5 and Table I that most air channels come with similar flow rate characteristics as they share the same geometry and dimension. When these valves are applied in real soft robotic applications, the consistency in flow rate characteristics within each valve channel ensures consistent behaviour of the soft robots no matter which valve state is used. The average flowrate under 50 kPa pressure loss over all valve channels is 6.74 L/min. The maximum flowrate observed under 50 kPa is 7.42 L/min, measured at the "2-3 (STATE II)" channel in the 5/2 valve. The 3/2 way valve comes with the best consistency between its channels, with a percentage deviation of 3.37% and 2.92% in C and b respectively. The 5/2 way valve comes with a slightly lower consistency between its air channels, with a percentage difference of 6.23% and 17.9% in C and b respectively. The slight reduction in consistency is caused by the increased number of piston seals included in the design. One should note that the 4/2 way valve comes with a relatively poor consistency as the "1-4" channel in State II comes with a much lower flow conductance. This is because the special "bypass" geometry of this air channel significantly increases the overall length and geometrical complexity of the channel. The other three air channels in the 4/2 way valve come with a satisfying consistency with a percentage deviation of 1.6% and 15.0% in C and b respectively.

C. Breakthrough pressure when no energy supplied

Due to the bistability of the valve, no energy is required for maintaining either state of the valve. This experiment aims to find out how much pressure can be held in the valve channels without any external force or power applied. The experimental schematics is shown in Fig. 6(a). Three pressure sensors (ADP60, Panasonic) were placed at each port of the valve. A compressor with pneumatic filter and regulator is used to apply air with gradually increased pressure (called source pressure P_s) to the input port (port 2) of the valve. The breakthrough pressure is defined as the maximum pressure that can be held within the air channel without leakage. The specific algorithm for breakthrough pressure identification is shown in Fig. 6(b). "$P_2 > 0.01 \times P_s$" indicates that leakage results in some unwanted "cross-talking" between channels, while "$P_1 < 0.99 \times P_s$" indicates that the pressurized air leaks to the exterior environment. Since all valves designed in this work share the same piston seal design, only 3/2 way valve is investigated here. The experimental results are shown in Fig. 6(c). The measured breakthrough pressure of a newly fabricated valve is 187.2 kPa, with a standard derivation of 3.73 kPa among five independent trials. A fatigue test is preformed to investigate the long term reliability of the spool seals made of Agilus 30. The position of the spool in the spool cylinder is repeatedly switched, while the breakthrough pressure is measured throughout the process every 500 cycles until failure. To investigate whether the hardness of the spool seals affects the long-term reliability of the valve, the same fatigue test is also preformed on a valve whose spool seals are made of a less compliant material (FLX9760, Stratasys Ltd, USA, 60A shore hardness). As shown in Fig. 6(d), the Agilus 30 spool seals retain the optimal performance within the first 1000 cycles and show a 35.9 % drop in breakthrough pressure at 1500 cycles, while the less compliant spool seals degrade within less than 200 cycles and completely fail after 600 cycles.

D. Controlling a bi-directional actuator

The modular approach of the valve design allows multiple channels to be connected to achieve diverse logical computation. To demonstrate the modularity, the multi-channel valves

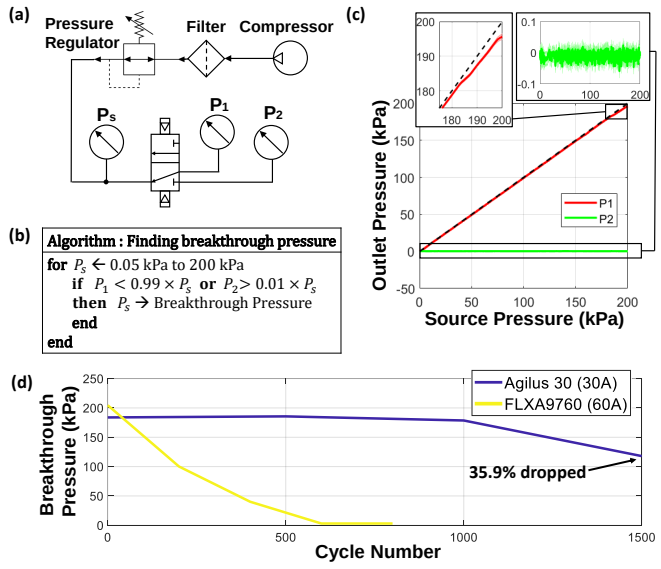


Fig. 6. **(a)** shows the experimental setup used to find the breakthrough pressure of the valve. P_s represents the source pressure applied to the inlet of the valve. P_1 and P_2 represent the measured pressure at the other two ports of the valve. The algorithm for breakthrough pressure identification is shown in **(b)**. The experiment results of the output pressure readings (P_1 and P_2) versus the source pressure P_s of a newly fabricated valve are shown in **(c)**. The long-term reliability of the spool seals with different shore hardness are presented in **(d)** in a fatigue test.

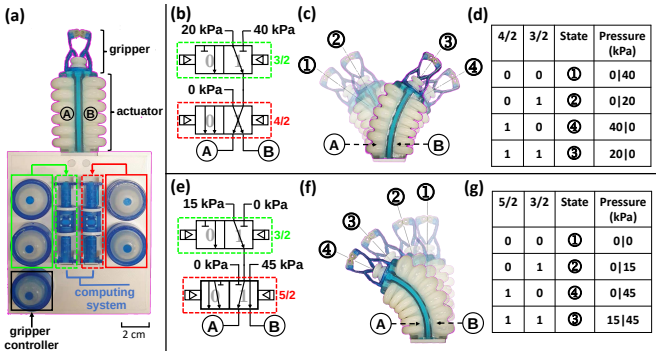


Fig. 7. **(a)** shows a bi-directional actuator with a gripper being controlled by an electronics-free control board consists of multi-channel valves. The computing system in the middle consists of two valves, while each of them switches its states based on the pneumatic signal sensed by the two 3D-printed pneumatic switches connected to it. A separate manual pneumatic switch is used to control the gripper. **(b)** shows the schematics when a 4/2 way valve and a 3/2 way valve is used to control the bi-directional actuators with two independent chambers. Chamber A and B refers to the two independent chambers in the bi-directional actuator. **(c)** shows all possible configurations, which can be achieved by switching the states of the valves. **(d)** shows the truth table, which describes the relationship between the valve state and each corresponding configuration. **(e)** shows the schematics when a 5/2 way valve and a 3/2 way valve is used to control the bi-directional actuators with two independent chambers. **(f)** shows all possible configurations, which can be achieved by switching the states of the valves. **(g)** shows the truth table, which describes the relationship between the valve state and each corresponding configuration.

were used to control a bi-directional actuator (see Fig. 7(a)). The bi-directional actuator consists of two air chambers with side bellows (Ⓐ and Ⓑ). Two different control schemes were used: (1) "3/2 way valve + 4/2 way valve" and; (2) "3/2 way valve + 5/2 way valve". Four 3D printed manual switch controller were used to generate the pneumatic signal so that they can switch the state of the two valves based on manual operation. The schematics of the pneumatic circuits under both control schemes are presented in Fig. 7(b) and Fig. 7(e), respectively. Note that the constant pressure source used here is the same as the one used in Sec. III-A and Sec. III-C. A pneumatic driven gripper is attached to the tip of the bi-directional actuator to perform a demonstration of manipulation, attached in the supplementary video.

As shown in Fig. 7(c), the "3/2 way valve + 4/2 way valve" control scheme successfully controls the bi-directional actuator through four different postures located symmetrically in both directions. The measured bending angles are -54^o, -34^o, 36^o and 60^o. The slight difference between leftward and rightward bending angles are due to the small stiffness difference between the left and right chamber (manufacture error). As shown in Fig. 7(f), the "3/2 way valve + 5/2 way valve" control scheme behaves like a 2 bit Digital-Analogue Converter (DAC), controlling the bi-directional actuator through four different amount of bending in one direction. The measured bending angles are 0^o, 17^o, 43^o and 64^o.The two truth tables which state the relationship between the valve status and the actuator posture are shown in Fig. 7(d) and (g).

IV. Discussion

The multi-channel valves designed in this work come with several key features which are highly beneficial when applied with soft robots, including (a) high breakthrough pressure; (b) low mass and; (c) multi-channel compatibility.

Thanks to the multi-material 3D printing technique, the soft spool seals can be directly printed on the spool without any post-processing or manual assembly. Meanwhile, the accuracy of the printer guarantees precise control on the optimal fit between the spool seal and the cylinder. These advantages bring this multi-channel valve design a much higher breakthrough pressure (187.2 kPa) compared with other electronics-free valves used in soft robotics, such as soft kink valves (63.0 kPa) [7, 19, 11] and 3D printed fluidic circuitry (at least 10 kPa pressure required by the valve to regulate a 20kPa source pressure) [9]. The high breakthrough pressure means the valves are compatible with a broader range of soft robots, which require higher pressure during operation [20]. Meanwhile, the ability to regulate high-pressure pneumatic signal enables the valve to deliver a higher range of pressure gain (the pressure ratio between the output pneumatic signal and the input pneumatic signal). The benefits brought by the high pressure-gain has been demonstrated in [11], where a small pneumatic signal induced by a tactile sensor is sufficient to switch the state of a bistable valve, and therefore changing the locomotion direction of a soft legged robot. The mass of the multi-channel valve designed in this work is 5.4 g for 3/2 way valve, 6.1 g for the 4/2 way, and 6.3 g for the 5/2 way valve. This is 20 times lighter than the conventional

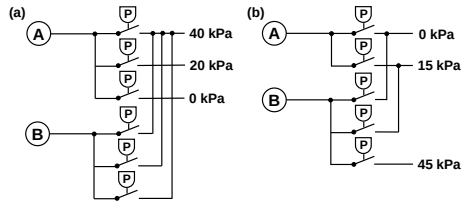


Fig. 8. The control scheme used to achieve the same functionalities as demonstrated in Fig. 7 by using only 2/2 approach. **(a)** shows the scheme for controlling the bi-directional actuator through four different postures at both bending directions (see Fig. 7(c)). **(b)** shows the scheme for controlling the bi-directional actuator through four different postures at single bending direction (see Fig. 7(f)).

rigid solenoid valves and 3-4 times lighter than the silicone-casted bistable valves [7]. The lightweight and electronics-free features of the valve enable it to be easily embedded in untethered soft robots without significantly increasing their mass or decreasing their mobility.

The valves designed in this work can control multiple independent air channels simultaneously, which can greatly reduce the number of valves used in the control circuit, especially when controlling soft robots with more than one air chamber. By using the "3/2 + 5/2 way valve" control scheme (see Fig. 7(e)(f)(g)), we successfully control the posture of the bi-directional actuator in a 2-bit DAC manner by using only two valves and two constant pressure sources. To achieve these postures with only 2/2 way valve, at least 5 valves must be used, while every valve requires an independent pneumatic signal (see Fig. 8(b)). In previous work [21], a similar 2-bit DAC operation make use of 12 valves and 4 constant pressure sources. By using the "3/2 + 4/2 way valve" control scheme (see Fig. 7(b)(c)(d)), we successfully control the posture of a two-chamber bi-directional actuator through four different configurations (two different bending directions with two different amplitudes). To achieve these postures with only 2/2 way valve, at least 6 valves must be used (see Fig. 8(a)). The valve number reduction brought by the multi-channel valves reduces the size and mass of the overall computing circuit and reduces the energy consumed by computing. Both of them are of great importance for soft robotic applications.

V. Conclusion

This paper presents a modular approach to design multi-channel bistable valves for pneumatically driven soft robots based on Multi-material 3D printing. Each valve comes with a bistable modular unit, which uses pneumatic signals to change its state. Different multi-channel-valve modular units (3/2 way, 4/2 way, and 5/2 way) are designed to provide varieties in the pneumatic circuit design. Each multi-channel-valve unit consists of a spool with multiple seals and a cylinder with multiple ports, therefore permitting and restricting the airflow in different air channels based on the state of the bistable unit. An FE simulation is performed to validate the design of the spool seals. The experiment characterization verifies that the proposed multi-channel valves successfully perform the desired function. The state of the valve can be switched by a pneumatic signal ranging from 48.6 kPa to 65.4 kPa, depending on the multi-channel valve units chosen. The valve can withstand a pressure of 187.2 kPa in the controlled air channels without leakage. The air channels in the multi-channel-valve units come with an average sonic conductance of 0.0436 lpm/kPa and an average critical pressure ratio of 0.379. With different multi-channel-valve units chosen, a dual-chamber bi-directional actuator can be controlled through different sets of computing system configurations.

Overall, the following features of this modular multi-channel valve design make it suitable for soft robotic applications. (1) The high breakthrough pressure of the valve ensures its compatibility with high-pressure soft actuators. (2) A higher range of pressure-gain. (3) A much lighter weight compared with conventional solenoid valves or other electronics valves in previous work. (4) The valves' multi-channel design significantly reduces the number of valve units required when controlling multi-chamber soft robots. The valve number reduction brings a decrease in system size and mass and reduces the energy consumed by computing. For future work, the valves can be used in an oscillatory circuit to achieve gait control for a soft-legged robot with multiple chambers. Size miniaturization can also be investigated further.

References

[1] Chiwon Lee et al. "Soft robot review". In: *International Journal of Control, Automation and Systems* 15.1 (2017), pp. 3–15.

[2] James Walker et al. "Soft robotics: a review of recent developments of pneumatic soft actuators". In: *Actuators*. Vol. 9. 1. Multidisciplinary Digital Publishing Institute. 2020, p. 3.

[3] Liang He et al. "A method to 3D print a programmable continuum actuator with single material using internal constraint". In: *Sensors and Actuators A: Physical* 324 (2021), p. 112674.

[4] Robert F Shepherd et al. "Multigait soft robot". In: *Proceedings of the national academy of sciences* 108.51 (2011), pp. 20400–20403.

[5] Andrew D Marchese, Cagdas D Onal, and Daniela Rus. "Soft robot actuators using energy-efficient valves controlled by electropermanent magnets". In: *2011 ieee/rsj international conference on intelligent robots and systems*. IEEE. 2011, pp. 756–761.

[6] Yichao Tang et al. "Leveraging elastic instabilities for amplified performance: Spine-inspired high-speed and high-force soft robots". In: *Science Advances* 6.19 (2020), eaaz6912.

[7] Philipp Rothemund et al. "A soft, bistable valve for autonomous control of soft actuators". In: *Science Robotics* 3.16 (2018).

[8] K. Xu and N. O. Pérez-Arancibia. "Electronics-Free Logic Circuits for Localized Feedback Control of Multi-Actuator Soft Robots". In: *IEEE Robotics and Automation Letters* 5.3 (2020), pp. 3990–3997.

[9] Joshua D Hubbard et al. "Fully 3D-printed soft robots with integrated fluidic circuitry". In: *Science Advances* 7.29 (2021), eabe5257.

[10] Jin Huat Low et al. "A bidirectional soft pneumatic fabric-based actuator for grasping applications". In: *2017 IEEE/RSJ International Conference on Intelligent Robots and Systems (IROS)*. IEEE. 2017, pp. 1180–1186.

[11] Dylan Drotman et al. "Electronics-free pneumatic circuits for controlling soft-legged robots". In: *Science Robotics* 6.51 (2021).

[12] M Metwally, A Abou El-Azm Aly, and M Ola. "Effect of spool side chambers on dynamic response of contactless electro-operated pneumatic directional control valve". In: *Computers & Fluids* 86 (2013), pp. 125–132.

[13] Slawomir Blasiak, Pawel Andrzej Laski, and Jakub Emanuel Takosoglu. "Rapid Prototyping of Pneumatic Directional Control Valves". In: *Polymers* 13.9 (2021), p. 1458.

[14] Dusty R Miller et al. "A bistable, multiport valve enables microformulators creating microclinical analyzers that reveal aberrant glutamate metabolism in astrocytes derived from a tuberous sclerosis patient". In: *Sensors and Actuators B: Chemical* 341 (2021), p. 129972.

[15] Viacheslav Slesarenko and Stephan Rudykh. "Towards mechanical characterization of soft digital materials for multimaterial 3D-printing". In: *International Journal of Engineering Science* 123 (2018), pp. 62–72.

[16] Sihan Wang, Liang He, and Perla Maiolino. "Design and Characterization of a 3D-printed Pneumatically-driven Bistable Valve with Tunable Characteristics". In: *IEEE Robotics and Automation Letters* 7.1 (2021), pp. 112–119.

[17] International Organization for Standardization (ISO). *Pneumatic fluid power — Determination of flow-rate characteristics of components using compressible fluids*. 2013.

[18] Sagar Joshi, Harshal Sonar, and Jamie Paik. "Flow path optimization for soft pneumatic actuators: Towards optimal performance and portability". In: *IEEE Robotics and Automation Letters* 6.4 (2021), pp. 7949–7956.

[19] Kai Luo et al. "Soft kink valves". In: *Journal of the Mechanics and Physics of Solids* 131 (2019), pp. 230–239.

[20] Matthew A Robertson et al. "Soft pneumatic actuator fascicles for high force and reliability". In: *Soft robotics* 4.1 (2017), pp. 23–32.

[21] Daniel J Preston et al. "Digital logic for soft devices". In: *Proceedings of the National Academy of Sciences* 116.16 (2019), pp. 7750–7759.

4.6 Supporting Information

4.6.1 Supporting Video

A video summarizing the work can be found here: `https://youtu.be/WLF4muOTwRg`

4.6.2 CAD files

The CAD files of the 3D printed bistable valve can be found in the following Github repository: `https://github.com/sihanwang0318/MultiChannelValve.git`

5

Magnetorheological elastomer (MRE) based proportional valves

Contents

5.1 Problem 57
5.2 Objective 58
5.3 Key Contributions and Limitations 58
5.4 Contributed Paper 59
5.5 Supporting Information 76
5.5.1 Some supporting videos 76
5.5.2 Dimensions of the MRE valves. 76
5.5.3 Dimensions of the four different MRE geometries investigated. 76

5.1 Problem

As we present in the Literature Review chapter, various approaches have been exploited for developing integrable control devices for soft pneumatic robots, including silicone-casted bistable valves [8] (see Section 2.2.2), 3D-printed pneumatic transistors [69] (see Section 2.2.3), tube-balloon logic devices [73] (see Section 2.2.4), and so on. One should note that most of these devices work in a digital ON/OFF manner. Our previous works described in Chapters 3 and 4 are also digital valves,

controlling the pneumatic actuators through a finite number of distinct states. However, recent applications of soft robots require not only binary ON/OFF control. Proportional valves offer a distinct advantage over digital on/off valves in the field of soft pneumatic robots due to their fine-grained control capabilities. Unlike digital valves that operate in a binary fashion, proportional valves allow for precise regulation of pressure inside the pneumatic actuators, enabling smoother and more flexible movements in soft robotic systems. This level of control is essential for applications requiring delicate and adaptive interactions, such as human-robot interaction [9], grasping [10], soft pneumatic arm control [11] and so on. Moreover, the ability of proportional valves to adjust flow rates in real-time enables programmable dynamic responsiveness. This is crucial for applications where dynamic behaviours are of importance, such as different types of soft locomotive robots [30, 47, 110]. Traditionally, to achieve continuous pressure regulation in soft robots, the most widely used devices are industrial proportional valves. Despite their accuracy and robustness, these expensive devices are usually bulky and rigid, therefore can not be integrated into the body of soft robots.

5.2 Objective

The objective of this work is to develop a novel proportional valve which can be integrated into the body of soft robots without sacrificing its compliance. Apart from the integrability, the valve is desired to have fast response, low cost and high accuracy to fit the needs of soft robots.

5.3 Key Contributions and Limitations

The contributions of the work are as follows:

- A novel proportional valve design which applies MRE in controlling soft actuators, achieving continuous pressure modulation with high accuracy (mean error of 0.05 kPa) and fast response (<0.02s).

- The compliant nature of the MRE enables the valve to be easily integrated into any silicone-based soft robots.
- Higher durability and robustness due to its structural simplicity. No significant behaviour change was observed after 10k operation cycles.
- Lower cost compared to the industrial proportional valves.
- As a major limitation, the MRE valve design suffers high operation current (2 A)and power (16 W) for continuously generating the magnetic fields. This can be solved by introducing electro-permanent magnets into the design.

5.4 Contributed Paper

The work has been published as a journal paper in *Advanced Intelligent Systems*. The paper is attached on the following pages.

A magnetorheological elastomer based proportional valve for soft pneumatic actuators

Sihan Wang Liang He Alessandro Albini Peizhi Zhang Perla Maiolino*

Sihan Wang
Address: Department of Engineering Science, University of Oxford, Oxford, UK
Email Address: sihan.wang@eng.ox.ac.uk
Dr. Liang He
Address: Department of Engineering Science, University of Oxford, Oxford, UK
Email Address: liang.he@eng.ox.ac.uk
Dr. Alessandro Albini
Address: Department of Engineering Science, University of Oxford, Oxford, UK
Email Address: alessandro.albini@eng.ox.ac.uk
Peizhi Zhang
Address: Research Innovation Center Waseda Univ., Shinjuku-ku, Tokyo 162-0041, Japan
Email Address: pzsc@fuji.waseda.jp
Prof. Perla Maiolino
Address: Department of Engineering Science, University of Oxford, Oxford, UK
Email Address: perla.maiolino@eng.ox.ac.uk

Keywords: *magnetorheological elastomers, soft robotics, proportional valve, pneumatic actuator*

The interest in soft pneumatic actuators has been growing rapidly in robotics, owing to the contact adaptability with the material softness. However, these actuators are mostly controlled by rigid electronic pneumatic valves, which can hardly be integrated into the robot itself, limiting its mobility and adaptability. Recent advances in soft or electronics-free valve designs provide the potential to achieve an integrated soft robotic system with reduced weight and rigidity. Nevertheless, the challenge in valve response remains open. To enable dynamic control of a soft pneumatic actuator, a fast-response proportional valve is needed. In this paper, we explored the potential of Ecoflex-based magnetorheological elastomer (MRE) membrane to create a proportional valve that can be used in the control of a soft robot made from the same silicone material. Experimental characterization shows that the proposed MRE valve ($30mm \times 30mm \times 15mm$, 30 grams) can hold pressure up to 41.3 kPa and regulate the airflow in an analog manner. The valve is used to perform closed-loop Proportional-Integral-Differential (PID) control with 50 Hz on a soft pneumatic actuator, and is able to control the pressure within the actuator chamber with a root-mean-square error of 0.05 kPa.

1 Introduction

Soft robots driven by soft pneumatic actuators (SPAs) are known for their low cost, high adaptability to unknown environments and safe human-robot interaction [1]. As an emerging area, researchers have developed various SPAs with different materials, structure designs, actuation modes, pressure ranges, and fabrication procedures [2]. A basic design principle has been carried out in most of the SPAs: the actuation is achieved by mediating the interaction between pressurized air and soft elastomeric materials. The dexterity, mobility, and efficiency of a SPA ultimately depend on the control of pressure. Previously, this pressure control was achieved mainly by conventional pneumatic systems, including solenoid valves, proportional regulators, displacement pumps, syringe drivers, and electronic controllers [3, 4]. These bulky and non-integrable devices limit the performance of pneumatic-driven soft robots, carrying challenges for the robot to be miniaturized, untethered, and agile.
These existing limitations motivate researchers to develop different lightweight and integrable control devices for regulating pressure in soft pneumatic actuators. One category is the pneumatically driven soft valves, which directly receive pneumatic signals and correspondingly regulate the pressure in the pneumatic actuators [5]. Various fabrication techniques have been used including silicone-casting [5] and 3D printing [6]. These devices can be used as the pneumatic correspondent of various electronic components including transistors, diodes [7], oscillators, logic gates [8], Digital-Analog Converters (DAC) [9]

and digital memories [10]. Pneumatically driven soft valves bring simplicity to the system since the conversion of sensory information into electrical signals is no longer required. The soft structure also means these valves can be integrated into the robots themselves without sacrificing the overall compliance of the robots. However, these devices come with a relatively long response time (ranging from 0.5s to 1.5s), which limits their application in control.

Electrostatic effect [11] and dielectric effect [12] has also been investigated in valve designs for controlling soft pneumatic actuators, introducing faster response time but require a high operation voltage. The requirement of voltage amplifiers limits their application in soft robots, especially when the robot is demanded to be untethered and miniaturized.

The devices listed above work in a digital ON/OFF manner. However, recent applications of soft robots require not only binary ON/OFF control, but also proportional control on their pressure or flowrate.

The ability to continuously alter the pressure or flowrate of soft robots in an analog manner provides advantages in various applications. In human-robot interaction [13] and adaptive grasping [14], the proportional pressure control is essential for controlling the interactive force between the actuator and its environment. For soft pneumatic manipulators [15], the proportional pressure control is the key for trajectory following. In soft-matter computing [16], continuously altering the flowrate enables us to fine-tune the frequency of an oscillating pneumatic signal.

The most widely used devices for continuously altering the pressure are syringe drivers [3] and industrial proportional valves [17]. These highly accurate and robust approaches are usually bulky and non-integrable for soft robots. Moreover, the syringe drivers cannot deliver a large flowrate and therefore are slow in response time.

Recent research has attempted the proportional pressure control of soft robots by using electro-permanent magnets (EPM) [18]. By adjusting the magnetic field strength, the device can continuously alter its fluidic resistance and therefore modulate the pressure. However, this device is only capable of controlling soft robots driven by Magnetorheological Fluid, which narrows down its application since many soft robots are driven by compressed air.

Another solution for proportional pressure or flowrate control on a fluid-driven actuator is by using thermally-driven hydrogels [19]. The physical properties of such devices (reflected in the fluidic resistance) are controlled by temperature to achieve adjustment of the flowrate and pressure of fluidic-driven soft actuators. However, a long response time (over 20 minutes) is usually required which brings limitations for most soft robotic applications.

Recent development in Magnetorheological Elastomers (MRE) shows that this soft magneto-active rubber-like material has the advantages of continuously adjustable mechanical characteristics [20] and fast response time [21, 22] under magnetic actuation. The interaction between the MRE and the magnetic field has been exploited in designing various actuators. Microfluidic pumps and mixers based on MRE [23] have been used in microfluidic platforms. Soft actuators [24] and grippers [25, 26, 27] have been developed, which make use of the force exerted by MRE when placed within a magnetic field. Besides, MRE can be used as highly deformable robot skin for proprioception in soft pneumatic actuators [28]. An MRE valve [29] has also been designed based on its deformation under a magnetic field, although the valve is based on a highly bulky and rigid mechanism which limits its application in soft robots. Recently, MRE has been applied in the soft robotics field thanks to its compliant nature and its ability to be integrated into silicone-based soft robots [24, 26]. The softness of the material and its capability to bond to silicone rubber indicate the potential of developing an MRE-based valve to be integrated with SPAs for fast and precise fluidic control.

Thus, this paper presents the design of a proportional valve for controlling soft pneumatic actuators based on an MRE membrane. The valve makes use of an electrical coil embedded in silicone to generate a magnetic field and therefore controlling the MRE membrane movement. The valve behavior was characterized by two aspects: (1) the variation in flowrate of the valve under different electric currents and; (2) the maximum pressure held by the valve without leaking under different electric currents. The valve behaviors with different MRE membrane thicknesses and air channel widths were investigated. To demonstrate the applications of the MRE valve designed, the valve was used to perform closed-loop flowrate

and pressure control on a soft pneumatic actuator. It was observed that the valve can control the pressure within the actuator chamber with a root-mean-square error (RMSE) of 0.05 kPa.

2 Results

2.1 MRE Valve Design

2.1.1 Valve Structure and Working Principle

The MRE valve consists of an electromagnet and an MRE membrane to create the valve gate. Figure 1(A) shows the cross-sectional view of the proposed valve. The electromagnet is sealed in silicone to ensure maximum compliance. The gate of the valve is designed by encapsulating a pressurized cavity between the MRE membrane and the electromagnet. The detailed dimensions of the valve can be found in Supporting Information S1. The proposed valve works in a "normally-open" manner as shown in Figure 1(B). When no current goes through the coil, no force is exerted by the MRE so air travels freely through the air channel. When an electric current is engaged in the coil, a magnetic field will be generated. The MRE is then magnetized and exerted a force toward the concentration of the magnetic flux. This attraction force deforms the MRE and correspondingly restricts the gate of the valve. This "restriction" effect gradually increases as the electric current increases and eventually shuts down the airflow completely. A video presenting the working principle of the MRE valves can be found in Supporting Video SV2.

2.1.2 Fabrication

Multi-stage silicone casting is used to fabricate the MRE valve presented in this work. The detailed fabrication procedure is presented in Figure 1(C). The first stage of casting aims to seal an electromagnet into a silicone housing. This is achieved by placing the electromagnet into a cylindrical mold filled with uncured silicone. The second stage of casting aims to build an MRE layer on top of the electromagnet while leaving an air channel inside. This is achieved by pouring the uncured MRE on top of the electromagnet. A Mylar strip is placed in the middle during MRE's curing and pulled out afterward, therefore leaving a thin air channel as the gate of the valve. A video describing the whole fabrication process can be found in Supporting Video SV1, while the technical details involved can be found in Section 4.

2.2 Experiment Characterization

2.2.1 Optimal Carbonyl Iron Powder Content Level

It was shown in literature [30] that the saturation magnetization improves by increasing the content of the Carbonyl Iron Powder (CIP). Creating MRE with high CIP content is beneficial to the valve design as it decreases the electric current required to regulate the airflow. However, higher CIP content in MRE results in significantly reduced flexibility and difficulties in polymerization. The bonding between the MRE membrane and the silicone base of the valve can also be an issue. To investigate the optimal CIP content level for fabricating the MRE valves, a set of samples as shown in Figure 2(A) were tested. These samples were made by bonding an MRE membrane (2mm thickness) to a silicone membrane (2mm thickness) while leaving an air channel in their middle. The detailed schematics used for the experiments are shown in Figure 2(B). The pressure within the air channel of the samples was gradually increased until the sample fails and the pressure was monitored during the whole process. The pressure at failure was then recorded. For each CIP content level, three identical samples were made and tested. The mean and standard deviation of the pressure at failure for different CIP levels are presented in Figure 2(C). Two different failure modes were observed. For samples with a CIP level of no more than 80%wt, the MRE membrane undergoes a burst in its center under high pressure and leaves a crack. The pressure at failure here is consistently higher than 150 kPa. For CIP levels higher than 80%wt, the MRE

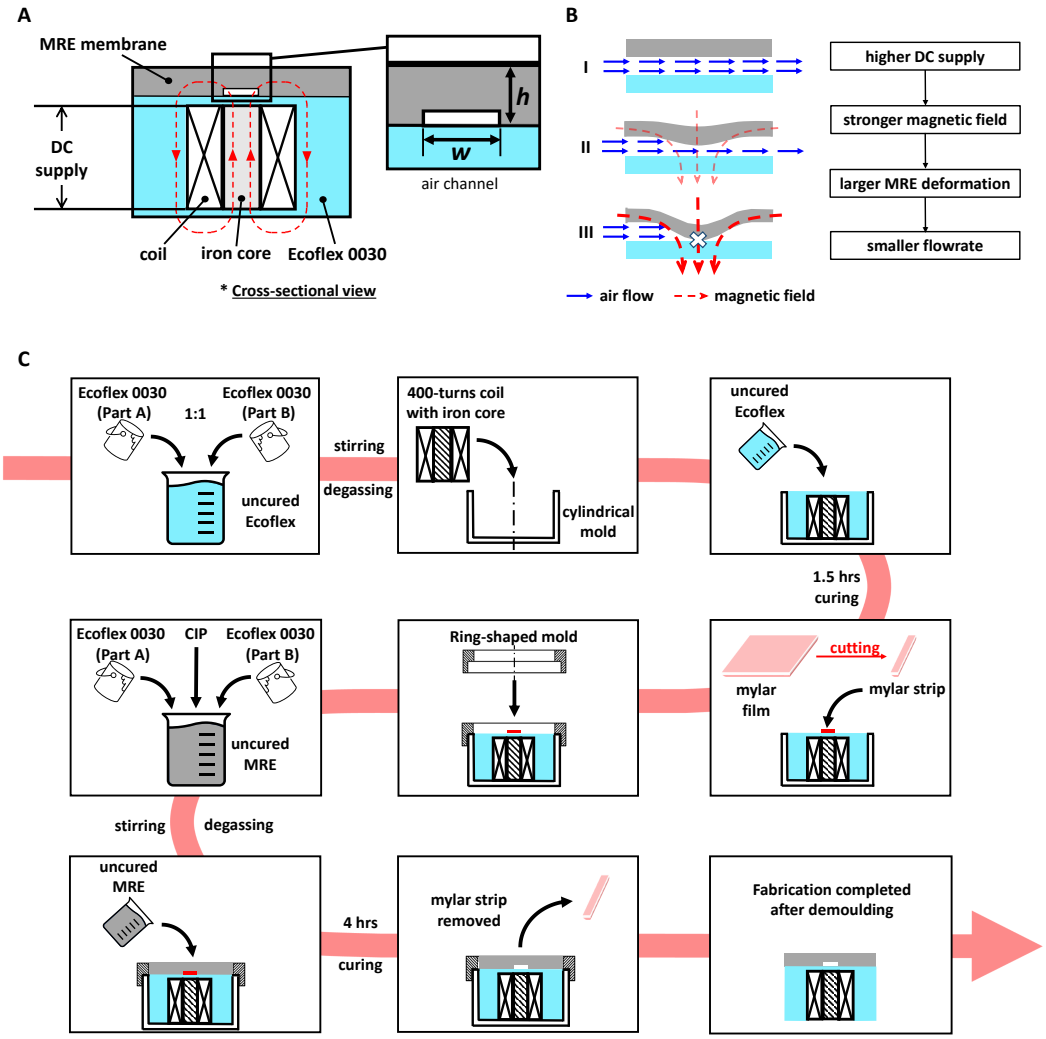


Figure 1: **(A)** shows the structure of the MRE valve. The concept and working principle of the valve is demonstrated in **(B)**. The detailed views of the air channel explain how the deformation of the MRE valve affects the airflow through the channel. An increase in electric current results in a stronger magnetic field. This brings more deformation to the MRE membrane and therefore decreases the flowrate. **(C)** describes the fabrication process of the MRE valve.

layer delaminates from the silicone layer, indicating that the bonding between the two layers is the dominant weakness. The pressure at failure here drops significantly below 50 kPa. The standard deviation also increases, indicating a lack of consistency for samples with too high CIP levels. This inconsistency is most likely brought in during the fabrication process, as the higher CIP level significantly increases the viscosity of the uncured MRE and therefore makes it difficult to be cast into an even-thickness MRE membrane. Based on the results presented in Figure 2(C), the CIP content level chosen for fabricating the MRE valves is 80%wt, as it is the highest CIP level achieved without sacrificing too much strength. To further investigate the structure of the 80 wt% MRE, a scanning electron microscope (SEM) was used. Both the surface and the middle of the sample were examined by the SEM, aiming to investigate the structure consistency throughout the sample. Note that the sample was cut with a knife to observe the interior. The obtained SEM images are shown in Figure 2(D) and (E). As shown in Figure 2(D), no significant difference were found between the MRE structure at its surface and middle, indicating a good structural consistency throughout the sample. Despite the relatively large weight ratio, the iron particles are uniformly distributed within the silicone in both images. This homogeneous particle distribution is of benefit as it ensures the repeatability and consistency of the MRE membrane behavior. Figure 2(E) represents a 3000 times magnified SEM image of the interior of the sample. This SEM image with larger amplification ratio clearly shows that the CIP particles are firmly embedded into its silicone matrix,

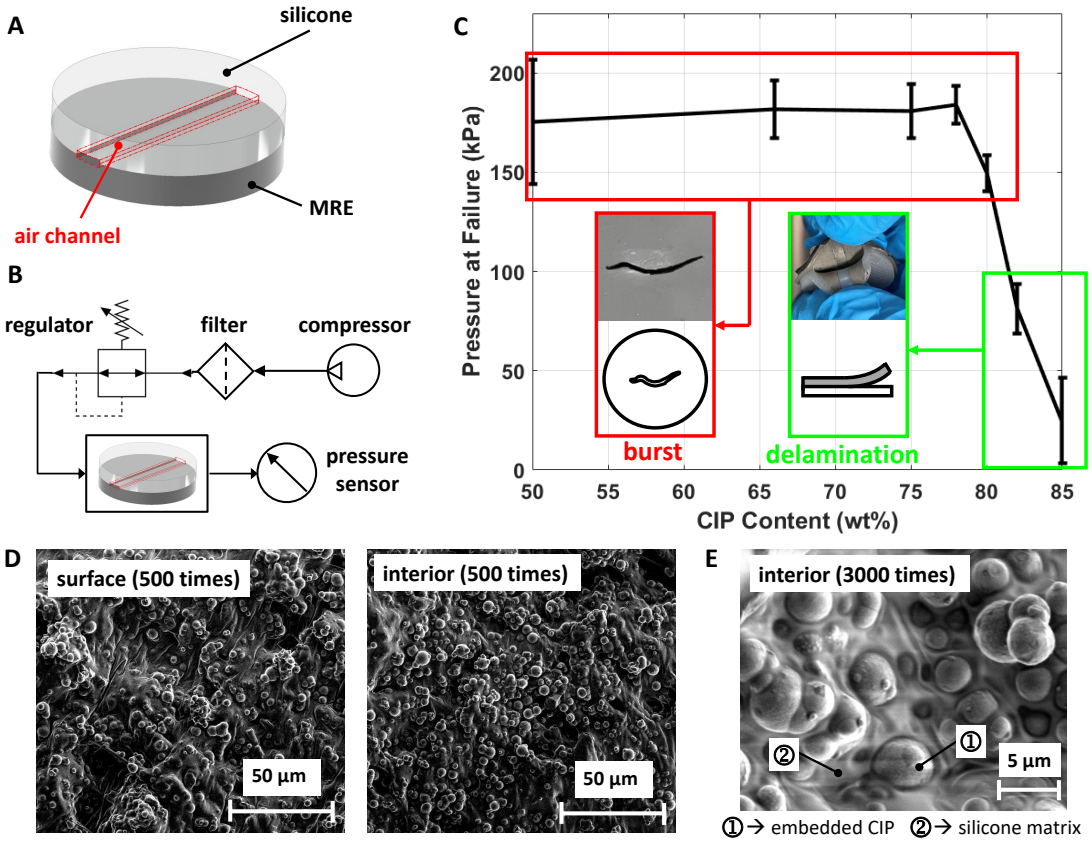


Figure 2: Maximum allowable pressure held by the MRE membrane against different CIP level. **(A)** shows the structure of the samples used in this experiment. **(B)** represents the experiment schematics used in this experiment. **(C)** shows the pressure at failure of the MRE membrane with different CIP content level. The errorbar indicates the standard deviation among three samples. **(D)** shows the 500 times magnified SEM images of the 80 wt% MRE sample at its surface and interior. **(E)** shows the 3000 times magnified SEM image of the 80 wt% MRE sample at its interior.

therefore bringing sufficient structural stability.

2.2.2 Membrane Geometry

Finite Element simulation (implemented in Comsol Multiphysics 5.6, detailed setup in Section 4) shows that the maximum magnetic flux density occurs at the annular region at the edge of the iron core. The magnetic field generated by the coil at the plane of the air channel is shown in Figure 3(A). To investigate the impact of MRE membrane geometry on valve performance, four different MRE membrane geometries (shown in Figure 3(B)) were fabricated and tested based on the simulated magnetic field.
All four geometries cover the annular region with the strongest magnetic field. The simulated magnetic fields with different MRE geometries are shown in Figure 3(C). The FE simulation shows that the "Full" and "Parallel line" provides the strongest magnetic field strength within the air channel. The larger magnetic flux density indicates that the MRE membrane can more effectively regulate the airflow given the same amount of electric current. To validate the simulation, four samples with different MRE geometries were fabricated and tested.
Experimental validation is performed with a constant input pressure of 20 kPa, while the detailed schematics are shown in Figure 3(D). The experimental results are shown in Figure 3(E). The valve with "Full" geometry shows the best performance, which successfully shuts down the 20 kPa incoming flow with a minimum electric current of 2.25 A. The valve with "center" geometry is able to shut down the 20kPa incoming flow only when the electric current reached 3 A. Based on these results, the MRE geometry chosen for fabricating the MRE valves is the "Full" geometry, due to its optimal performance and ease of fabrication.

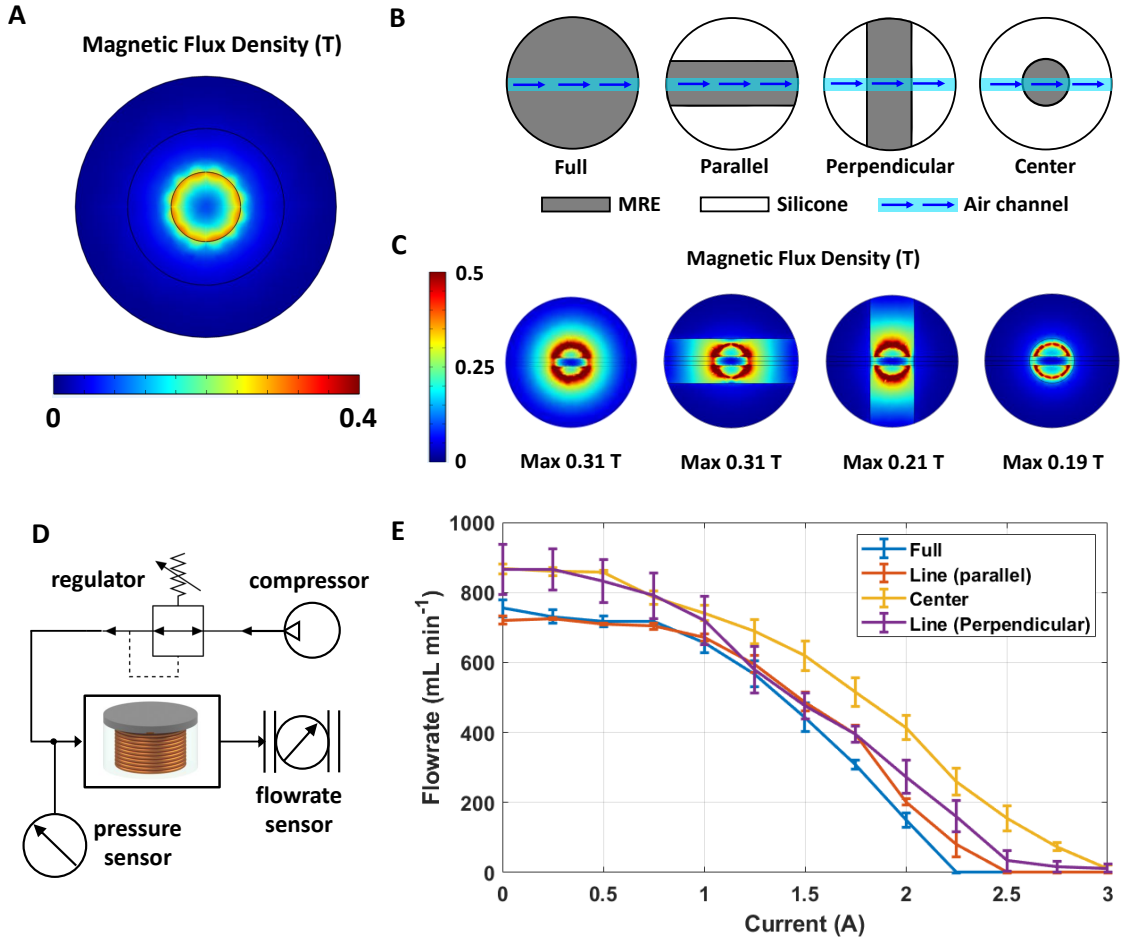


Figure 3: **(A)** represents the simulated magnetic flux density generated by the coil itself at the top surface of the coil. **(B)** represents the four different MRE geometries investigated. **(C)** represents the simulated magnetic flux density at the plane of the air channel, with different MRE membrane geometries. **(D)** shows the schematics of the physical experiments and **(E)** represents the flowrate-current curve of the MRE valves with different MRE membrane geometries. The errorbar indicates the standard deviation among three different trials.

2.2.3 Effect of the MRE Thickness on Valve behavior

The behavior of the MRE valves is mainly described by the following two aspects: (a) the threshold pressure and (b) the flowrate under different current supplies (flowrate-current profile). threshold pressure is defined as the maximum pressure the valve can withstand without leaking when the electrical current is engaged in the coil. This value is of interest as it ensures the valve can deliver enough pressure to drive the pneumatic soft actuators efficiently. The flowrate-current profile confirms the valve can be operated in an analog manner with repeatability. With increasing current, the airflow decreases monotonically due to the increase of the magnetic force and the reduction of the opening width of the valve channel. This variable pneumatic resistance can be used to control the soft pneumatic actuators similar to an industrial proportional valve.

To investigate the effect on valve behavior brought by the different MRE membrane thicknesses, samples with membrane thicknesses ranging from 1 mm to 3 mm with a step size of 0.5 mm were tested. The flowrate and threshold pressure characterization results are presented in Figure 4(A) and (B), respectively.

Figure 4(A) indicates that the increase in MRE thickness significantly enhances the regulation of the airflow. As the MRE thickness increases from 1 mm to 3 mm, the electric current required to fully shut down the flow decreases from over 3 A to 1.75 A. This is because the increase in MRE membrane thickness increases the exerted attractive force due to more magnetization, meaning that a weaker magnetic flux density is required to shut down the flow. However, one should also note that the flowrate of the

valve without electric current ("fully open" state) is decreased by a thicker MRE membrane, even if the air channel width is kept constant. As the MRE thickness increases from 1 mm to 3 mm, the flowrate without electric current decreases by 33.1%. This is because the thicker MRE performs less deformation when air passes beneath it.

2.2.4 Effect of the Air Channel Width on Valve behavior

As shown in Figure 4(A), the increase in MRE membrane thickness not only decreases the current required to regulate the airflow, but also decreases the volume flowrate when the valve is in its fully "open" stage (with no electric current going through). This lack of flowrate is undesirable as it increases the response time of the soft robots with large internal volumes. One possible way to easily compensate for the flowrate reduction is by increasing the width of the air channel. This can be easily achieved by increasing the width of the Mylar strip used during the fabrication. Three samples with different air channel widths (1 mm, 2 mm, and 3 mm) were fabricated here and tested. The obtained characterization results are shown in Figure 4(C) and (D).
As shown in Figure 4(C), the increase in air channel width significantly scales up the volume flowrate. The valve with a 3 mm channel width brings an additional 406% flowrate at "fully open" state, compared to the one with a 1 mm channel width. Meanwhile, the electric current required to fully shut down the airflow does not see a significant change as the channel width increases. (see Figure 4(D)).

2.2.5 Temperature Response

The heat generated during the operation of the valve inevitably raises its temperature, therefore potentially changing the performance and characteristics of the valve. This experiment aims to investigate the performance of the valve during long-term continuous operation, including the temperature and the flowrate through the valve. An MRE valve sample with 3 mm channel width and 2 mm MRE thickness was used here. A constant electric current was applied to the coil. The temperature of the valve was kept monitored throughout the process by a temperature sensor placed in the middle of the bottom surface of the valve. The input pressure of the valve was kept at 20 kPa. The temperature and flowrate curves under three different levels of electric current (1 A, 1.75 A, and 2.5 A) were tested and presented in Figure 4(E) and (F). These electric current values were selected as they cover the range within which the pneumatic resistance of the valve changes most rapidly, according to Figure 4(C). The test was stopped when the surface temperature reaches 70 ^{o}C for safety. Sufficient time (1 hr) was placed between each trial to ensure that the valve returns to the ambient temperature.
It can be observed that it takes 62 s, 130 s, and 348 s for the MRE valve to reach 70 ^{o}C with a continuous electric current of 1 A, 1.75 A, and 2.5 A, respectively. This temperature rise does not change the basic working principle or the overall behavior of the valve qualitatively. The increase in current still brings a decrease in flowrate and eventually shuts down the airflow. However, the quantitative behavior of the valve does have a certain sensitivity to the temperature. The flowrate through the valve channel sees a 30.2% and 23.8% reduction over the entire heating process with 1 A and 1.75 A electric current, indicating a small increase in the pneumatic resistance due to the temperature change. This thermal drift is most likely caused by the thermal deformation of the MRE membrane and the silicone. This observed sensitivity to the temperature may affect the control accuracy when the valve is used in an open-loop control scheme, as the valve behavior will slightly differ from the pre-obtained characterization results. However, this thermal drift can be compensated by a sensory feedback loop with a simple PID controller (see Section 2.3), as the basic working principle of the valve remains valid. When 2.5 A current is applied, the valve is able to shut down the airflow completely without leaking throughout the entire heating process.

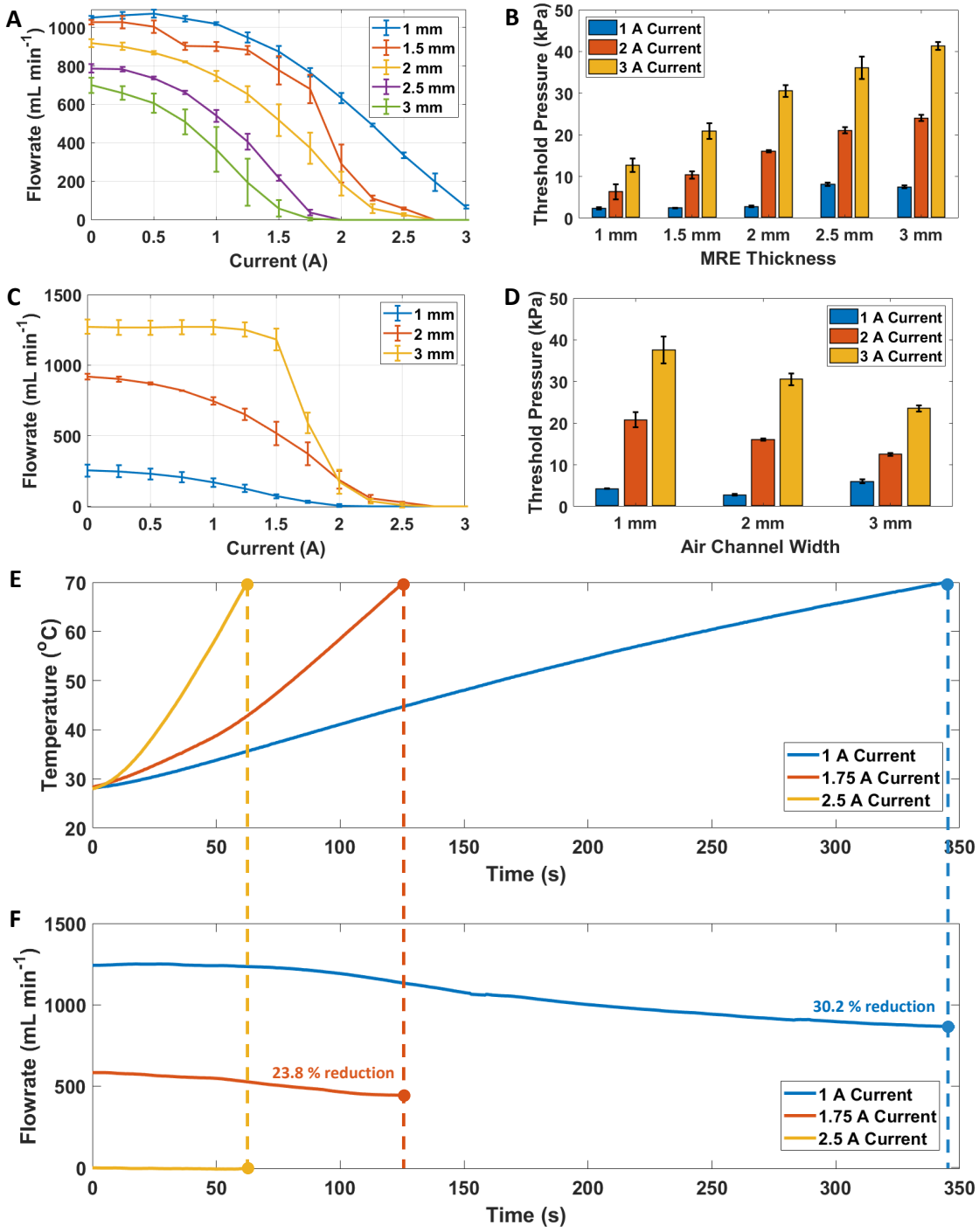


Figure 4: Characterization of the MRE valve behavior with different design dimensions. **(A)** shows the flowrate-current curve of the MRE valves with different MRE thicknesses. **(B)** shows the threshold pressure of the MRE valves with different MRE thicknesses. **(C)** shows the flowrate-current curve of the MRE valves with different channel widths. **(D)** shows the threshold pressure of the MRE valves with different air channel widths. **(E)** presents the temperature profile of the MRE valves under different amount of electric current, while **(F)** presents how the flowrate of the valve changes during the temperature increase.

2.2.6 Durability Test

Cycling tests were performed to investigate the durability of the MRE valve.The tests were preformed by repeatedly activating the MRE valve with 2mm channel width and 2mm membrane thickness for 5000 times. For each cycle, an electric current of 2.5A was applied to the valve for 0.5 seconds, followed by a resting time of 1.5 seconds. For safety reasons, the cycling tests were paused every time when the valve

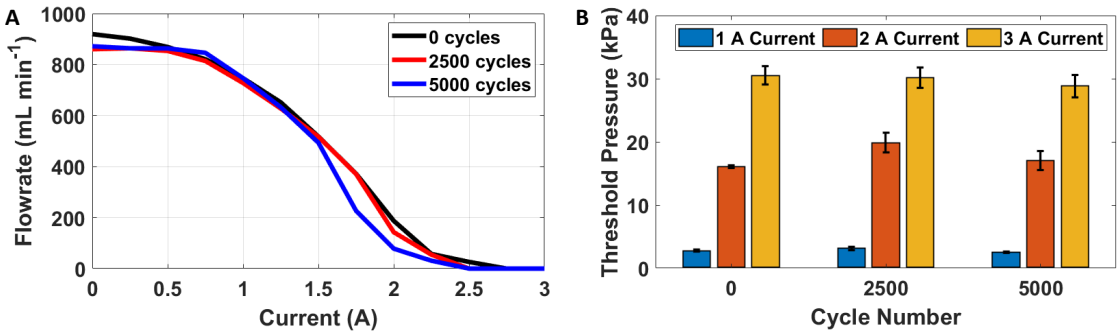


Figure 5: Durability performance of the MRE valve under cycling tests. **(A)** shows the flowrate-current curve of the MRE valves after 0, 2500 and 5000 cycles. **(B)** shows the threshold pressure of the MRE valves after 0, 2500 and 5000 cycles.

temperature exceeded 70^{o}C and resumed after cooling. The valve behavior (flowrate-current profile and threshold pressure) were tested after every 2500 cycles. Note that the valve was cooled down to room temperature before these tests to isolate the thermal drift from the observations. The measured valve behavior after 2500 and 5000 cycles are presented in Figure 5.
It was observed that the valve does not undergo any significant change in its properties and behaviors after the 5000 cycles. The flowrate-current curve keeps its trend after 5000 cycles and only deviates from the initial values by a root-mean-square-error of 55.3 mL min^{-1}. The 5000 repeating cycles increase the threshold pressure of the MRE valve by a factor of 11.8%, 24.0% and 5.9% with a 1 A, 2 A and 3 A electric current, respectively. This minor increase in the threshold pressure can be caused by the fact that the iron particles were slightly reoriented or relocated in the silicone matrix during the cycling tests.

2.3 Applications in Controlling Soft Robots

Flowrate and pressure are the two most significant factors to be considered when controlling soft pneumatic robots. To drive these robots accurately, one should be able to continuously regulate these two parameters to the desired values. Therefore, to validate the applications of these MRE valves in controlling soft pneumatic robots, the closed-loop control performance of these valves in both flowrate and pressure regulation was tested. PID controllers were implemented in real-time on a microcontroller. The detailed setup, tuning and the PID parameters can be found in Section 4 and Supporting Information. The step response of the controlled flowrate and pressure were recorded.

2.3.1 Closed-loop Flowrate Control

For closed-loop flowrate control, the experimental schematic is shown in Figure 6(A). Constant pressure was supplied to the inlet of the MRE valve, while the MRE valve outlet was connected to the atmosphere via a flowrate sensor. The MRE valve here behaved like a pneumatic resistor whose resistance value can be continuously altered. The reading of the flowrate sensor q was then compared with a reference value q^*, which is a step signal in our test. The error between the reference and the actual value was sent into a PID controller. The reference value was also sent into a forward model obtained in Figure 4, which gave the expected amount of electric current required by the valve. The final control signal combined the output of the PID controller and the model. The obtained control signal was then fed into a signal amplifier to control the electric current through the MRE valve. The electric equivalent of the pneumatic circuit used here is presented in Figure 6(B). Figure 6(C) presents the step response of the controlled flowrate under three different control schemes tested. "PID only" means only a PID controller is used in the loop. In this case, the response time at the rising edge is around 0.5 s while the response time at the falling edge is around 0.8 s. No significant steady-state error is observed, and the root-mean-square error (RMSE) during the steady state is 14.37 mL min^{-1}. "Model only" means the PID feedback loop is disabled and the valve is controlled in an open-loop manner with only the forward model obtained from Figure 4. A significant error of more than 50 mL min^{-1} is observed, caused by the

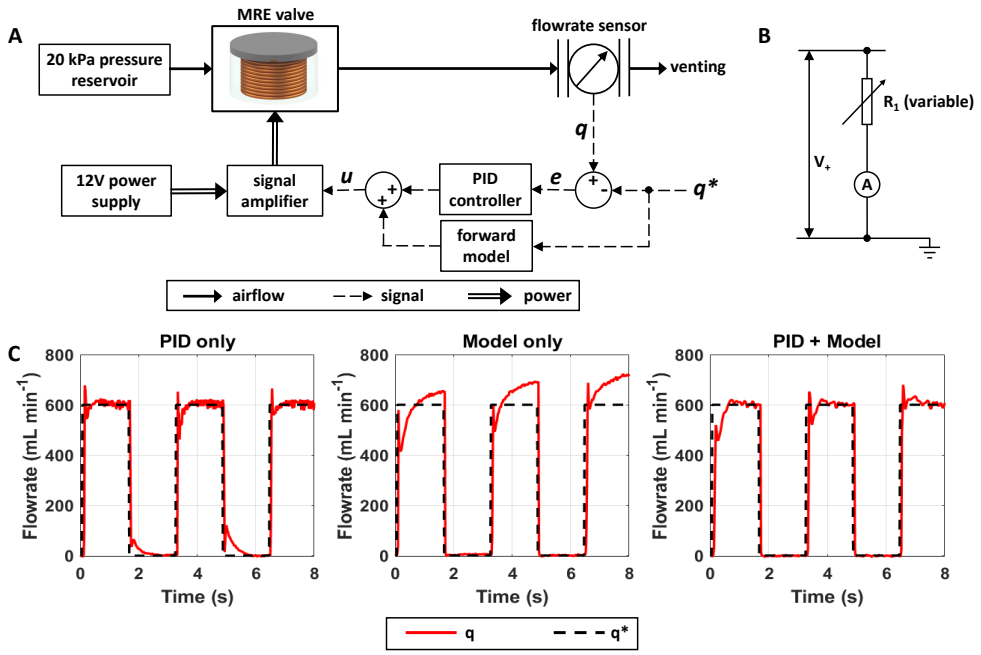


Figure 6: Flowrate control achieved by the MRE valves. **(A)** shows the schematics of the pneumatic and electric circuit used to achieve a closed-loop feedback control on flowrate with the MRE valve. **(B)** shows an electronic equivalent of the pneumatic circuit used here. **(C)** shows the step response of the controlled flowrate under different control scheme.

difference between the actual valve behavior and the pre-obtained model. The response time at the rising edge is longer than 2 s due to the viscoelasticity of the MRE membrane. However, the response time at the falling edge reduces to 0.15 s thanks to the feed-forward model. "PID + Model" means the feed-forward model is combined with a PID controller to eliminate the model inaccuracy and thermal drift. This scheme shows the best performance among all three schemes. The response times are 0.4 s and 0.1 s at the rising and falling edge respectively. No significant steady-state-error are observed and the RMSE during the steady state is 8.77 mL min^{-1}.

2.3.2 Closed-loop Pressure Control

For closed-loop pressure control, the schematics are shown in Figure 7(A). The pressure reservoir was set at 15 kPa. The soft actuator (PneuNet, a silicone-casted bending actuator [31]) was placed between the MRE valve and the venting path. When no electric current passes through the MRE valve, it was fully opened. This means the soft pneumatic actuator had much lower pneumatic resistance at its upstream than its downstream, therefore bringing a large pressure within the actuator chamber. When a large electric current passed through the valve, the valve was fully closed. In this case, the air inside the chamber would soon escape to the atmosphere and the soft pneumatic actuator would return to its natural shape. The pressure reading p in the actuator chamber was then compared with a reference value p^*. The error between the actual and reference pressure was then fed into a PID controller (see details in Supporting Information S3), whose output was fed into a signal amplifier to control the electric current in the MRE valve. The electric equivalent of the pneumatic circuit used here is presented in Figure 7(B). The MRE valve is equivalent to the variable resistor R_1, the natural pneumatic resistance of the venting path is equivalent to the constant resistor R_2 and the pneumatic actuator can be seen as a capacitor C. Figure 7(C) presents the step response of the controlled pressure within the soft actuator. The slowest response (0.7 s) occurs when the reference signal goes from 0 to 8 kPa. This is limited by the fluid-dynamic nature of the system, as it takes time for the air to pressurize the large actuator chamber through a relatively narrow valve channel. The RMSE of the controlled pressure at each steady state is 0.05 kPa. Figure 7(D) presents the postures of the soft pneumatic actuator at each steady state. A video of the pneumatic actuator being controlled can be found in Supporting Video SV3.

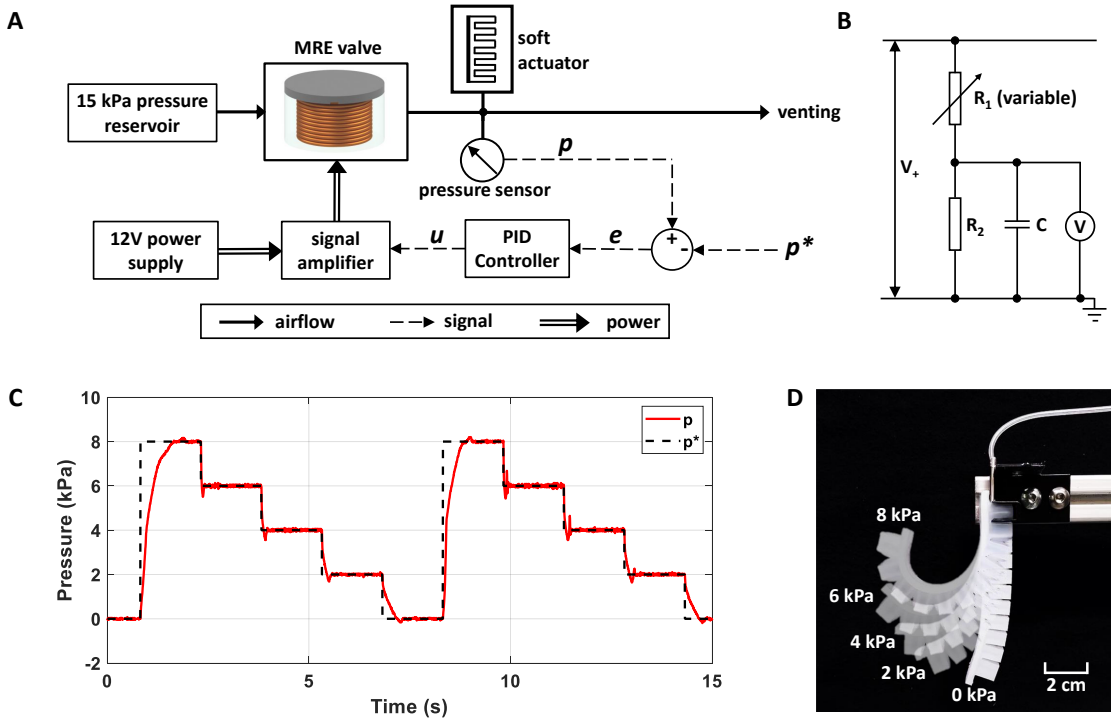


Figure 7: Pressure control achieved by the MRE valves. **A** presents the schematics of the pneumatic and electric circuit used to control the pressure within a soft pneumatic actuator. **B** shows the electronic equivalent of the pneumatic circuit used for pressure control. **C** shows the step response of the pressure within the soft pneumatic actuator controlled by the MRE valve. **D** shows the different amount of bending of the actuator under different desired pressure values.

3 Discussion and Conclusions

This paper presents a proportional valve which is based on the activation of an MRE membrane. Inspired by the continuous deformation of MRE under a magnetic field, this design utilizes silicone-casting to produce an air channel within MRE whose pneumatic resistance can be continuously altered by the magnetic field generated by a coil. Apart from the analog activation manner, this design also ensures a fast response time, operating at a time scale of tens of milliseconds, much shorter than the mechanical response time of most soft pneumatic actuators. Multiple advantages of this MRE valve can be observed when compared with those existing proportional valves used in industries. Firstly, this MRE valve can be integrated into silicone-based soft robots as it is made with compliant MRE and silicone materials. The total cost of the valve is well below $5, which is much lower than its industrial counterparts. Moreover, the valve comes with a simple structure with no moving parts. This brings the valve better mechanical robustness, ease of manufacture, and compatibility with both pneumatic and hydraulic systems. Lastly, the MRE valve comes with higher accuracy in the lower pressure region (below 40 kPa), which makes it highly suitable for soft robotic applications.

The experiment characterization proves that the valve can hold pressure up to 41.3 kPa. The valve works in an analog manner, whose pneumatic resistance can be continuously changed by adjusting the electric current through it from 0 to 3 A. Closed-loop flowrate regulation and pressure control with a 50 Hz control frequency were implemented to demonstrate the compatibility and responsiveness of the valve for controlling soft pneumatic robots.

One major limitation existing in the current design is the temperature rise during operation caused by the Joule heating effect. Though this temperature rise does not affect the basic working principle or the overall valve behavior qualitatively, the pneumatic resistance of the valve does exhibit a thermal drift. This may become problematic when the valve is used for open-loop control with no sensory feedback available. This limitation could be addressed in future work by replacing the electric coil with an electropermanent magnet (EPM), applying embedded temperature compensation or introducing a heat dissipa-

tion system. In future studies, the size miniaturization and the possibility to pack multiple channels and valves in a circuit will be investigated.

4 Experimental Section

Fabrication of MRE valve:
The fabrication procedure can be found in Figure 1(C). Firstly, equal amount of Part A and Part B of the silicone elastomer (Ecoflex 00-30, Smooth-On, USA) were mixed. Ecoflex 00-30 was a type of platinum-catalyzed silicone with a shore hardness of 00-30. The mixed elastomer was well-stirred and then placed in a vacuum chamber (3CFM/7.6L, VEVOR, UK) until the formation of new bubbles stops. Meanwhile, a 400-turn coil with an iron core (EK1909U, Gikfun, China) was placed in the center of a 3D-printed cylindrical mold (printed by Creality Ender-5 with 1.75mm PLA). The mixed and degassed silicone was then poured into the mold until reaching the mold brim. The brim was designed to be slightly higher than the coil, ensuring that the coil can be fully enclosed in silicone. After curing for 1.5 hrs, the silicone was mostly cured and was strong enough to perform the following fabrication procedures. A sheet of Mylar film (0.075 mm, RS PRO, UK) was cut into strips of 2 mm width. The strip was then placed at the top middle of the silicone cylinder, followed by a ring-shaped mold (printed by Creality Ender-5 with 1.75mm PLA) attached to the top of the previous cylindrical mold. The uncured MRE was fabricated by combining 5μm Carbonyl Iron Powder (Sigma-Aldrich, USA) with Ecoflex 00-30. The MRE was well-stirred and degassed in a vacuum chamber until no bubble turns out. After fully being mixed and debubbled, the uncured MRE was then poured into the ring-shaped mold until it reaches the mold brim. After four hours of curing, the poured-in MRE layer bonded firmly with the silicone beneath. The mylar strip was then pulled out gently so that an air channel was formed. Lastly, The MRE valve was removed from the mold.

SEM Setup: Platinum sputtering was performed in advance with a sputtering device (MSP-1S, Nissin EM Ltd.) to reduce sample charging and enhance secondary electron emission. The scanning electron microscope (SEM) used here is JSM-6510LA, manufactured by JEOL Ltd. The observation was performed at an acceleration voltage of 3 kV and a working distance of 10 mm.

Magnetic Field Simulation:
The simulation was constructed in COMSOL Multiphysics 5.6, while the specific settings are as followed:

- **Geometry Construction:** MRE valves were constructed in COMSOL using the "Geometry" function. Same as the MRE valve in the physical world, it also contained a core (cyl1), a coil (cyl2), a silicone housing (cyl3), and an MRE membrane with a flow pass (cyl4) in the simulation. Additionally, a block was built to cover the entire MRE valve as the surrounding environment (blk1).
- **Material Selection:** The materials of cyl1, cyl2, cyl3, cyl4, and blk1 were set to soft iron, copper, silicone, soft iron, and air, respectively. These are the preset materials in the COMSOL library. The relative permeability was 5000 for cy1 (i.e., core), 1 for cy2 (i.e., coil), 10 for cy3 (i.e., silicone housing), 10 for cy4 (i.e., MRE membrane), and 1 for blk1 (i.e., air). Here, we set the relative permeability of the MRE membrane to 10, based on related research on MRE [32].
- **Physics Study:** "Magnetic Field" was selected as the physics study by using the "Add Physics" function. In the "Magnetic field" menu, we added "Ampere's Law" with cyl1, cyl3, and cyl4 selected. To build the magnetic field modelling, we used relative permeability to represent the constitutive relation, which can be presented by:

$$B = \mu_0 \mu_r H \tag{1}$$

where B is the magnetic flux density, μ_0 is the permeability of the vacuum, μ_r is the relative permeability of the materials, and H is the magnetic field strength. Additionally, μ_0 is set as $4\pi \times 10^{-7}$ H m^{-1}. We then added "Magnetic Insulation" and "Initial Values" with cyl1, cyl2, cyl3, and

cyl4 selected. In the "Initial Values," the "Magnetic vector" potential was selected to 0. Finally, we added "Coil" to cyl2. In the "Coil" setting, we set the "Conductor model" to "Homogenized multi-turn", the "Coil type" to "Numeric", the "Coil current" to 2 A, the "Number of turns" to 400, and the "Coil wire cross-section area" to 0.35 mm. In the "Input", the subcategory of "Coil," a cross-section surface was selected to define the input current.

- **Mesh & Study:** The whole MRE valve module was meshed by selecting the "Mesh" function. The sequence type was set to "Physics-controlled mesh". And the "Element size" was set to "Normal". The minimum element quality was around 0.17, and the average element quality was around 0.6. Since the main function of the simulation was to confirm the magnetic field density of four different MRE membranes, the average element quality did not need to be high. Therefore, the average element quality of 0.6 satisfied our requirements. In the "Study", we added 2 steps. Step 1 was "Coil geometry analysis", and Step 2 was "Stationary". Then we clicked "Compute" to calculate the simulation.
- **Results:** A "Slice plot" with the "Magnetic Flux Density Norm" was used to obtain the simulated magnetic field presented in the paper. The "Slice plot" was selected to the surface on the long side of the flow pass. "Rainbow" was selected in the "Coloring and Style".

Valve Characterization:

- **Flowrate-Current Profile Characterization:** A compressor (BB50D, Bambi Air Compressor LTD, with integrated reservoir) with pneumatic filter (AL20-F02-A, SMC) and regulator (AR20-F02-1-B, SMC) was used to keep the input pressure constant throughout the process. A pressure sensor (ADP60, Panasonic) was placed at the inlet of the valve to monitor this pressure. The current through the MRE valve was driven by a continuous DC power supply box with current reading (GPS-3303, GW-INSTEK). The flowrate through the valve under different amounts of electric current is recorded by a digital flowrate sensor (HAF 20SLPM AIR, Honeywell).
- **Threshold Pressure Characterization:** A compressor (BB50D, Bambi Air Compressor LTD, with integrated reservoir) with a pneumatic filter (AL20-F02-A, SMC) and regulator (AR20-F02-1-B, SMC) was used to incrementally increase the input pressure applied to the valve from 0 kPa. This supply pressure was continuously monitored by a pressure sensor (ADP60, Panasonic) throughout the entire process. To detect any leakage of the valve, the volume flowrate sensor (HAF 20SLPM AIR, Honeywell) was directly connected to the valve output. Once the flowrate sensor came out with a reading larger than 5 mL min^{-1}, the valve was identified as "leaked" and the input pressure then was recorded as the threshold pressure. Three independent trials were performed to ensure repeatability.
- **Temperature Response Characterization:** The temperature readings were obtained by a digital temperature sensor (DS18B20, SMD). a piece of electric tape is used to ensure firm contact between the sensor and the MRE membrane. The constant electric current through the coil is supplied by a DC power supply box with current reading (GPS-3303, GW-INSTEK). The flowrate through the valve was recorded by a digital flowrate sensor (HAF 20SLPM AIR, Honeywell).

Preparation of Pneumatic Actuator:
The pneumatic actuator used in this work is a PneuNet bending actuator [31]. We used the same fabrication technique as the original work. The main body containing the inflatable chambers and the strain-limiting bottom layer was cast individually at first with silicone (Eco-flex 00-30, Smooth-on, USA). They were then bonded together with the same type of silicone. The strain-limiting material used is paper (80gsm). After curing, the actuator was connected to the MRE valve via a needle (18G, blunt head) and silicone pipes (OD 2mm, ID 1mm).

Tuning of PID Controller:

For controlling the flowrate and pressure, a microcontroller (Teensy 4.1) is used to implement the closed-loop PID controller. The gains of the PID controllers were tuned empirically to achieve a fast response without significant overshoot or steady-state error. Firstly, only the P gain is introduced to increase the response speed. The I gain is then increased to reduce the steady-state error. Lastly, the D gain is brought in for suppressing oscillations. The detailed setup and parameters of the PID controllers are presented in Supporting Information S3.

Acknowledgements
This work was supported by the Engineering and Physical Sciences Research Council (EPSRC) Grant EP/V000748/1; S. Wang was supported by the CSC-PAG Oxford Scholarship for his DPhil study; P. Zhang was supported by JSPS KAKENHI Grant No.21J13536.

References

[1] N. El-Atab, R. B. Mishra, F. Al-Modaf, L. Joharji, A. A. Alsharif, H. Alamoudi, M. Diaz, N. Qaiser, M. M. Hussain, *Advanced Intelligent Systems* **2020**, *2*, 10 2000128.

[2] J. Walker, T. Zidek, C. Harbel, S. Yoon, F. S. Strickland, S. Kumar, M. Shin, In *Actuators*, volume 9. Multidisciplinary Digital Publishing Institute, **2020** 3.

[3] B. Wijnen, E. J. Hunt, G. C. Anzalone, J. M. Pearce, *PloS one* **2014**, *9*, 9 e107216.

[4] B. Zhang, J. Chen, X. Ma, Y. Wu, X. Zhang, H. Liao, *Soft Robotics* **2021**.

[5] P. Rothemund, A. Ainla, L. Belding, D. J. Preston, S. Kurihara, Z. Suo, G. M. Whitesides, *Science Robotics* **2018**, *3*, 16 eaar7986.

[6] S. Wang, L. He, P. Maiolino, *IEEE Robotics and Automation Letters* **2021**, *7*, 1 112.

[7] J. D. Hubbard, R. Acevedo, K. M. Edwards, A. T. Alsharhan, Z. Wen, J. Landry, K. Wang, S. Schaffer, R. D. Sochol, *Science Advances* **2021**, *7*, 29 eabe5257.

[8] D. J. Preston, P. Rothemund, H. J. Jiang, M. P. Nemitz, J. Rawson, Z. Suo, G. M. Whitesides, *Proceedings of the National Academy of Sciences* **2019**, *116*, 16 7750.

[9] S. Wang, L. He, P. Maiolino, *IEEE Robotics and Automation Letters* **2022**.

[10] M. P. Nemitz, C. K. Abrahamsson, L. Wille, A. A. Stokes, D. J. Preston, G. M. Whitesides, In *2020 3rd IEEE International Conference on Soft Robotics (RoboSoft)*. IEEE, **2020** 7–12.

[11] R. Diteesawat, T. Helps, M. Taghavi, J. Rossiter, *Science robotics* **2021**, *6*, 51 eabc3721.

[12] S. Xu, Y. Chen, P. H. Nak-seung, K. P. Becker, R. J. Wood, *Proceedings of the National Academy of Sciences* **2021**, *118*, 34.

[13] P. Polygerinos, N. Correll, S. A. Morin, B. Mosadegh, C. D. Onal, K. Petersen, M. Cianchetti, M. T. Tolley, R. F. Shepherd, *Advanced Engineering Materials* **2017**, *19*, 12 1700016.

[14] R. A. S. I. Subad, L. B. Cross, K. Park, *Applied Mechanics* **2021**, *2*, 2 356.

[15] T. George Thuruthel, Y. Ansari, E. Falotico, C. Laschi, *Soft robotics* **2018**, *5*, 2 149.

[16] D. Drotman, S. Jadhav, D. Sharp, C. Chan, M. T. Tolley, *Science Robotics* **2021**, *6*, 51 eaay2627.

[17] B. Eryilmaz, B. H. Wilson, *Journal of the Franklin Institute* **2006**, *343*, 1 48.

[18] K. J. McDonald, L. Kinnicutt, A. M. Moran, T. Ranzani, *IEEE Robotics and Automation Letters* **2022**, *7*, 2 3914.

[19] M. S. Kalairaj, H. Banerjee, K. S. Kumar, K. G. Lopez, H. Ren, *Bioengineering* **2021**, *8*, 9 127.

[20] J. M. Ginder, M. E. Nichols, L. D. Elie, J. L. Tardiff, In *Smart Structures and Materials 1999: Smart Materials Technologies*, volume 3675. SPIE, **1999** 131–138.

[21] A. G. Díez, C. R. Tubio, J. G. Etxebarria, S. Lanceros-Mendez, *Advanced Engineering Materials* **2021**, *23*, 6 2100240.

[22] M. Zhu, M. Yu, S. Qi, J. Fu, *Smart Materials and Structures* **2018**, *27*, 5 055017.

[23] S.-Y. Tang, X. Zhang, S. Sun, D. Yuan, Q. Zhao, S. Yan, L. Deng, G. Yun, J. Zhang, S. Zhang, et al., *Advanced Functional Materials* **2018**, *28*, 8 1705484.

[24] S. Kashima, F. Miyasaka, K. Hirata, *IEEE Transactions on magnetics* **2012**, *48*, 4 1649.

[25] P. Zhang, M. Kamezaki, Z. He, H. Sakamoto, S. Sugano, *IEEE Robotics and Automation Letters* **2021**, *6*, 4 8181.

[26] R. Guan, H. Zheng, Q. Liu, K. Ou, D.-s. Li, J. Fan, Q. Fu, Y. Sun, *Composites Science and Technology* **2022**, *223* 109409.

[27] V. Skfivan, O. Sodomka, F. Mach, In *2019 2nd IEEE International Conference on Soft Robotics (RoboSoft)*. IEEE, **2019** 126–130.

[28] H. Wang, M. Totaro, A. A. Blandin, L. Beccai, In *2019 2nd IEEE International Conference on Soft Robotics (RoboSoft)*. IEEE, **2019** 242–248.

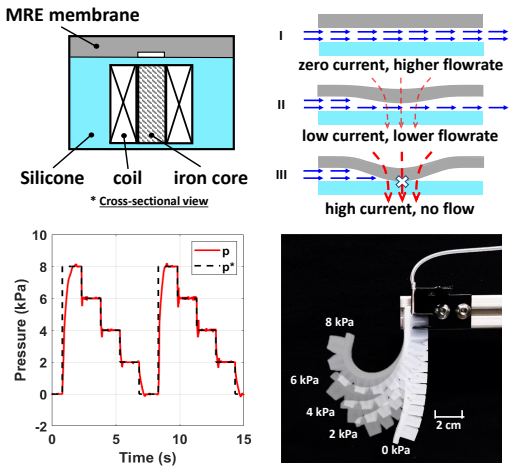
[29] H. Böse, R. Rabindranath, J. Ehrlich, *Journal of Intelligent Material Systems and Structures* **2012**, *23*, 9 989.

[30] A. K. Bastola, M. Hossain, *Composites Part B: Engineering* **2020**, *200* 108348.

[31] B. Mosadegh, P. Polygerinos, C. Keplinger, S. Wennstedt, R. F. Shepherd, U. Gupta, J. Shim, K. Bertoldi, C. J. Walsh, G. M. Whitesides, *Advanced functional materials* **2014**, *24*, 15 2163.

[32] A. K. Bastola, M. Paudel, L. Li, *Journal of Intelligent Material Systems and Structures* **2018**, *29*, 14 2946.

Table of Contents



Magnetorheological elastomer (MRE) proportional valves for controlling pneumatic soft robots are presented. The valves make use of the electromagnets to deform MRE membranes and regulate the airflow in an analog manner. They are able to accurately control the flowrate or pressure of soft pneumatic robots. These proportional valves offer great potential to simplify the way we control soft pneumatic robots.

5.5 Supporting Information

5.5.1 Some supporting videos

A video showing the flowrate regulation capability of the MRE valve is attached here: `https://youtu.be/talJvx7T-m8`

A video showing the fabrication process of the MRE valve is attached here: `https://youtu.be/LEyd6HjvUxc`

A video showing the real-time pressure control of a soft pneumatic actuator via the MRE valve is attached here: `https://youtu.be/q4G9t4Rnfnc`

5.5.2 Dimensions of the MRE valves.

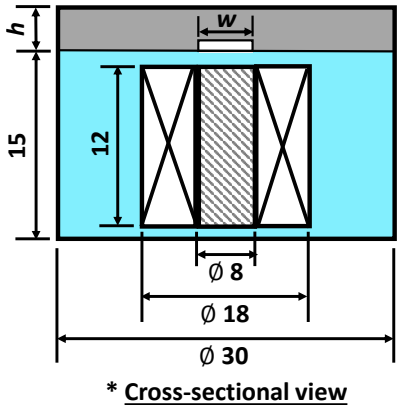


Figure 5.1: The detailed dimensions of the MRE valves are presented. h and w are the adjustable parameters investigated in this work.

5.5.3 Dimensions of the four different MRE geometries investigated.

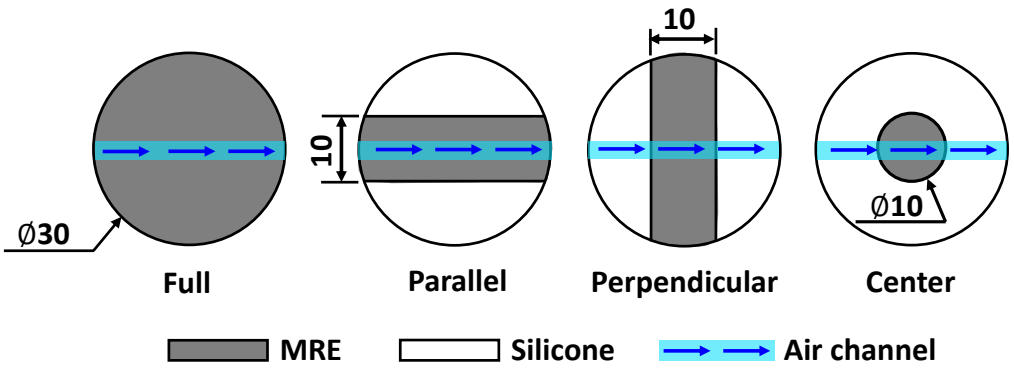


Figure 5.2: The detailed dimensions of the four different MRE geometries investigated.

6

Magnetorheological-Elastomer-Based Valve Array

Contents

6.1 Problem 77
6.2 Objective 79
6.3 Methodology 79
6.3.1 MRE valve unit and its scaling up 79
6.3.2 Magnetic interference 80
6.3.3 Heat Dissipation 82
6.3.4 Design and fabrication of MRE valve array 85
6.4 Results 87
6.4.1 Magnetic interference 87
6.4.2 Heat dissipation 89
6.4.3 Demonstration 91
6.5 Conclusions and future work 93
6.6 Supporting Information 93
6.6.1 Supporting Video 93
6.6.2 Simulation settings when investigating magnetic interference 94
6.6.3 Simulation settings when investigating thermal dissipation 95

6.1 Problem

The MRE-based proportional valve developed in our previous work (refer to Chapter 5) successfully achieves continuous pressure modulation with high accuracy and

rapid response. Its compliant nature allows for seamless integration into soft robots. However, each individual valve unit comes with only one channel, meaning that it is only capable of controlling one pneumatic actuator. Recently developed soft robots usually come with more complex structures and more pneumatic actuators to achieve their tasks like object manipulation or locomotion [112, 113]. This raises the need for a compact array comprising multiple MRE-based proportional valves operating steadily and independently within. Such a valve array opens up the possibility of realizing various untethered, multi-DOF soft pneumatic robots. For example, a soft robotic hand equipped with multiple pneumatic actuators [88] can be fully controlled by an MRE valve array embedded in its palm, eliminating the necessity for external proportional valves. Similarly, the locomotion of a soft quadruped robot [47] can be controlled by an onboard MRE valve array, marking a significant step toward achieving fully untethered locomotion with soft robots. However, simply packing multiple MRE valves in a compact space brings two major problems.

The first crucial problem is the magnetic field interference between each coil, which is commonly encountered when designing devices with multiple magnetic field sources [114, 115]. The magnetic interference can not only disrupt the independent functioning of MRE valves themselves but also affect nearby equipment [116]. One typical approach to solve the problem is magnetic shielding [117, 118]. However, the introduction of magnetic shields brings system complexity and is challenging to be embedded into soft robots. Another commonly used method is by carefully choosing the coil spacing and pole arrangement, reaching a balance between magnetic interference and space utilisation [119].

Overheating of the coils is another problem. Since multiple coils are integrated into the soft robots, the accumulated heat will be more difficult to be dissipated, which prevents the long-term operation of the valves and brings safety concerns. The predominant method employed for dissipating heat from electromagnetic coils is fluidic cooling [120]. There is a broad range of coolants to choose from including air, water, and helium [120–122]. The efficiency of such systems depends

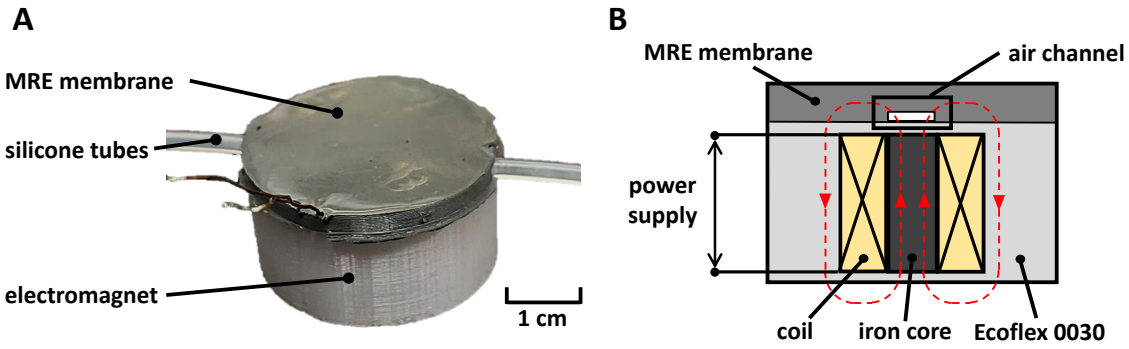


Figure 6.1: MRE valve single unit structure. **A** shows the photo of a single MRE-based proportional valve. An MRE membrane is located on top of an electromagnet embedded in silicone. The controlled air channel is located between the coil and the MRE membrane. **B** shows the cross-section view of the MRE valve. By applying an electric current to the electromagnet, a magnetic field whose strength is controllable can be generated. This magnetic field deforms the MRE membrane, therefore achieving a continuous flowrate or pressure modulation in the controlled air channel.

on multiple factors including the pumping power, the coolant type, the coolant flowrate, and channel geometry.

6.2 Objective

The objective of this work is to develop an MRE array that ensures multiple MRE valve units can work together independently and steadily within limited spaces. To address the magnetic interference problem, the spacing and pole arrangement of the valves inside the array need to be investigated through Finite Element (FE) simulations and physical experiments, ensuring the magnetic field generated by a single valve coil does not affect the operation of its neighbours. To address the overheating problem, an embedded fluid cooling system needs to be designed with the help of FE simulations. The heat dissipation rate needs to be sufficiently high so that the valve coil temperature remains safe during long-term operation.

6.3 Methodology

6.3.1 MRE valve unit and its scaling up

Our previous work[85] presents the design of an MRE-based proportional valve for controlling pneumatic robots. An electromagnet embedded in silicone is used to

generate magnetic fields while ensuring structural compliance. The valve's gate is created by enclosing a pressurized cavity between the MRE membrane and the electromagnet. The valve operates in a "normally-open" mode. When no current flows through the coil, there is no force applied by the MRE, allowing air to move freely through the air channel. However, when an electric current flows through the coil, it generates a magnetic field. This magnetic field magnetizes the MRE, causing it to be drawn toward the concentration of the magnetic flux and therefore restricting the valve's gate. As the electric current increases, this "restriction" effect gradually intensifies, eventually resulting in the complete cessation of airflow. Figure. 6.1 shows the structure of the MRE valve single unit.

6.3.2 Magnetic interference

The magnetic interference problem of the MRE valve array involves two aspects: 1) the interference between the MRE valve array and its surrounding environment and; 2) the interference between neighboring valve units within the array. The MRE valve array as a whole should have the least amount of magnetic flux leaked to the environment so that it won't affect the operation of external sensors or actuators. Meanwhile, the characteristics of every single valve unit should stay unaffected by the operation of its neighboring units, so that each MRE valve unit can be controlled independently and accurately.

By investigating the magnetic interference with different valve spacing and magnetic pole arrangement, one can find the optimal array layout which keeps sufficiently low magnetic interference while minimizing the size of the array. As the valve spacing gets sparser, the magnetic interference is suppressed significantly, but the overall size of the array also increases. The magnetic pole arrangement is also an important factor to be investigated. When the magnetic poles for neighbouring coils are opposite, the magnetic interference can be strengthened due to the formation of a closed magnetic loop.

COMSOL Multiphysics® was used to simulate and analyze magnetic field interference. The magnetic interference with different MRE valve spacing and pole

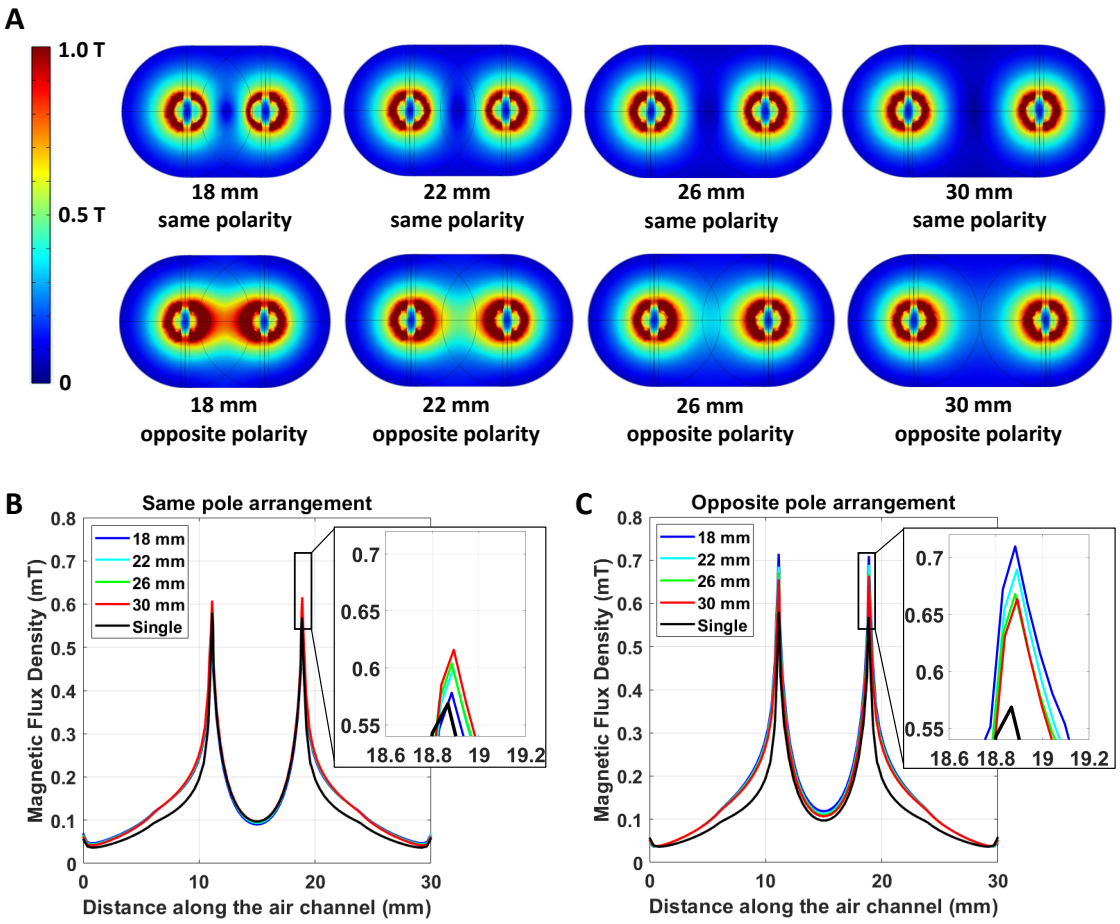


Figure 6.2: Simulation results of the magnetic field with different magnetic pole arrangements and MRE valve spacing. **(A)** shows the magnetic field distribution at the plane of the air channel with different valve spacing and pole arrangements. **(B)** shows the magnetic flux density along the air channel of the valve when the neighboring unit has the same pole arrangement. **(C)** shows the magnetic flux density along the air channel of the valve when the neighboring unit has the opposite pole arrangement. The benchmark (magnetic flux density of a single valve without interference) is shown in both **(B)** and **(C)** for ease of comparison. The enlargement views of the curve peaks are also given for clarity.

arrangement was investigated. Since the coil diameter is 18 mm, the valve spacing investigated in the simulation ranged from 18 mm to 30 mm. For each valve spacing, both the "same" and "opposite" pole arrangements were considered. An electric current of 2A was engaged in a pair of neighboring valves and the resultant magnetic field was simulated. The detailed settings of the simulation can be found in the supporting information. By comparing the simulated magnetic field within the neighbouring valves in the array against the original magnetic field within a single

MRE valve, the intensity of magnetic interference was obtained.

The magnetic field distribution with different valve spacing and pole arrangements are presented in Fig. 6.2(A). Compared with the same pole arrangement, the opposite pole arrangement brings a generally stronger magnetic field, especially at the region between the two valves. This indicates an undesirably strong magnetic interference with the surrounding environment. The valve spacing also significantly affects the environmental magnetic interference. As the valve spacing gets sparser, the magnetic field in the middle becomes weaker. At the position right between two valves, the magnetic flux density decreases from 0.71 T to 0.23 T when the valve spacing decreases from 30 mm to 18 mm with the same pole arrangement.

The magnetic flux density along the valve channel in the MRE valve array with the same and opposite pole arrangement is presented in Fig. 6.2(B) and (C). The magnetic flux density of a single MRE valve with no interference is considered the benchmark for comparison. To minimize the characteristics change when the valve is placed in an array, it is desirable to have a magnetic flux density curve that resembles the benchmark. It can be observed that the opposite magnetic pole arrangement brings a stronger magnetic flux density along the air channel than the benchmark. The peak value observed along the air channel is 0.71 T, 22% higher than the benchmark. In contrast, the magnetic flux density in the same pole arrangement was much closer to the benchmark. The peak value observed is 0.6 T, only 3% higher than the benchmark. Therefore, the same magnetic pole arrangement can bring the least change in valve characteristics. With a similar magnetic flux distribution along the valve channel, a single MRE valve design can be easily adapted into an array without re-characterization. Finally, based on simulations, we confirmed that the MRE valve array with the same pole arrangement and a valve spacing of 30 mm (1.2 times the diameter of a single valve unit) could satisfy our requirements.

6.3.3 Heat Dissipation

For a single MRE valve unit, the raise in temperature with different amounts of electric current has been measured and presented in Fig. 6.3(A). It took 348 s, 130

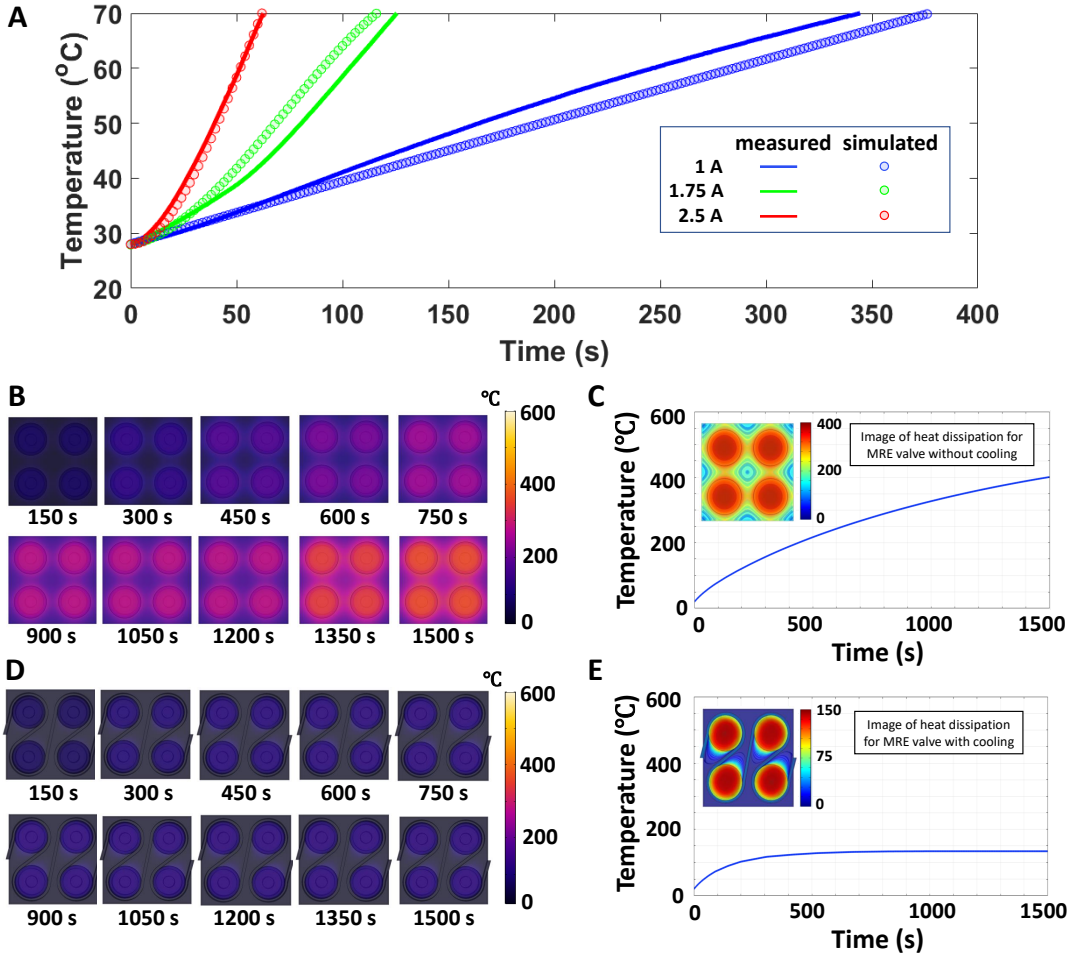


Figure 6.3: Thermal analysis on the MRE valve array. **(A)** shows the measured and simulated temperature curve of a single MRE valve under different amounts of electric current. The measured data was obtained by attaching a temperature sensor to the surface of a single MRE valve, while the simulated data was obtained when the convective heat transfer coefficient was set to 9.2 W/m^{2}K. **(B)** shows the simulated temperature distribution of the MRE valve array without a cooling system over a period of 1500s. **(C)** presents the simulated temperature-time curve at the center of the MRE valve units when the array is without a cooling system. **(D)** shows the simulated temperature distribution of the MRE valve array with a cooling system over a period of 1500s. **(E)** presents the simulated temperature-time curve at the center of the MRE valve units when the array comes with the proposed cooling system.

s, and 62 s for the MRE valve to reach 70 °C with a continuous current of 1 A, 1.75 A, and 2.5 A, respectively. When multiple coils are densely packed in a confined space in an MRE valve array, the issue of overheating becomes severe. The rapid temperature rise during operation imposes several constraints on the MRE valve array, such as reduced lifespan, unpredictable characteristics, and safety concerns.

The entire heat dissipation process of the MRE array can be described as followed. Firstly, the coil generated heat which can be described with Joule's law of heating. The heat travels through the silicone housing and MRE membrane via thermal conduction. Finally, the heat is released into the surrounding air by thermal convection. Heat conduction can be described by Fourier's Law as below.

$$Q_c = -kA_c\frac{dT}{dX} \tag{6.1}$$

where Q_c is the heat dissipation rate required by the valve unit, A_c is the cross-sectional area through which conduction occurs (i.e., the surface area of the coil), k is the thermal conductivity of the material (i.e., silicone), dT is the change in temperature, and dX is the change in distance.

The heat convection, i.e., heat transfer between the valve unit and surrounding environment, can be described as Newton's Law of Cooling as below.

$$Q_v = hA_v(T_s - T_\infty) \tag{6.2}$$

where Q_v is the heat dissipation rate required by the valve unit, A is the cross-sectional area through which conduction occurs (i.e., the surface area of the valve), h is the heat transfer coefficient, T_s is the surface temperature of the valve, and T_∞ is the temperature of the cooling materials. T_∞ is set to the ambient temperature (25 °C). Since the copper coil we used can sustain a maximum temperature of 155 °C, we set T_s to 155 °C also as the maximum operating temperature. And Q_v is equal to Q_c for sustainable heat dissipation, which can be described as

$$Q_v = Q_c = I^2R. \tag{6.3}$$

where I is the applied current, and R is the resistance of the coil. By substituting all known values into Equation 6.1, 6.2, and 6.3, the required value of h that keeps the coil temperature under 155 °C can be obtained. h should be over 1000 W/m^2K to ensure sustainable heat dissipation of the valve.

On the other hand, by matching the measured temperature increase curve of the MRE valve unit with the results obtained from the simulation (see Fig. 6.3(A)), it

can be found that the actual convective heat transfer coefficient between the MRE valve and the air under free convection h is only 9 W/m^2K. This actual h value is significantly lower than the required value for sustainable heat dissipation. Only the forced convection in liquids can provide a convective heat transfer coefficient larger than 1000 W/m^2K [123]. Therefore, a cooling system with flowing liquid is necessary.

Simulations were constructed to compare the difference in heat dispassion with and without a cooling system. For the cooling system simulation, we applied an S-shape cooling belt design, where water flows within the belt surrounding each valve unit. The detailed geometry of the cooling belt can be found in Section 6.3.4. For the system without cooling, the MRE valves were directly embedded into the silicone. The heat transfer coefficient between the MRE array and the surrounding air h was set to 9.2 W/m^2K, as investigated before. The water flow in the cooling belt is set as a laminar flow with a flowrate of 0.36 L/min. The electric current through all electromagnets is set to 1.5 A. A time-dependent study was implemented, whose detailed settings can be found in supporting information. The temperature increase of the MRE valve array center was recorded from 0 to 1500 s, while the thermal images of the MRE valve array were recorded every 150 s. The results are shown in Fig. 6.3(B)-(E).

Fig. 6.3(C) shows that the temperature of the MRE valve array increased continuously until 400 °C without a cooling system. With the cooling system, the temperature converged at 140 °C after 600 seconds (see Fig. 6.3(E)). The simulation results showed that such a water cooling system is capable to keep the coil temperature below 155 °C, ensuring MRE valves in the array work continuously and safely. In the following section, we focused on the design and fabrication to achieve such a cooling system in practice.

6.3.4 Design and fabrication of MRE valve array

To conduct cooling fluid into the valve array, a cooling chamber that tightly wounds the valves in an S shape is introduced, as shown in Fig. 6.4(B). The layout of the cooling channel is designed in this particular way to achieve both efficient cooling

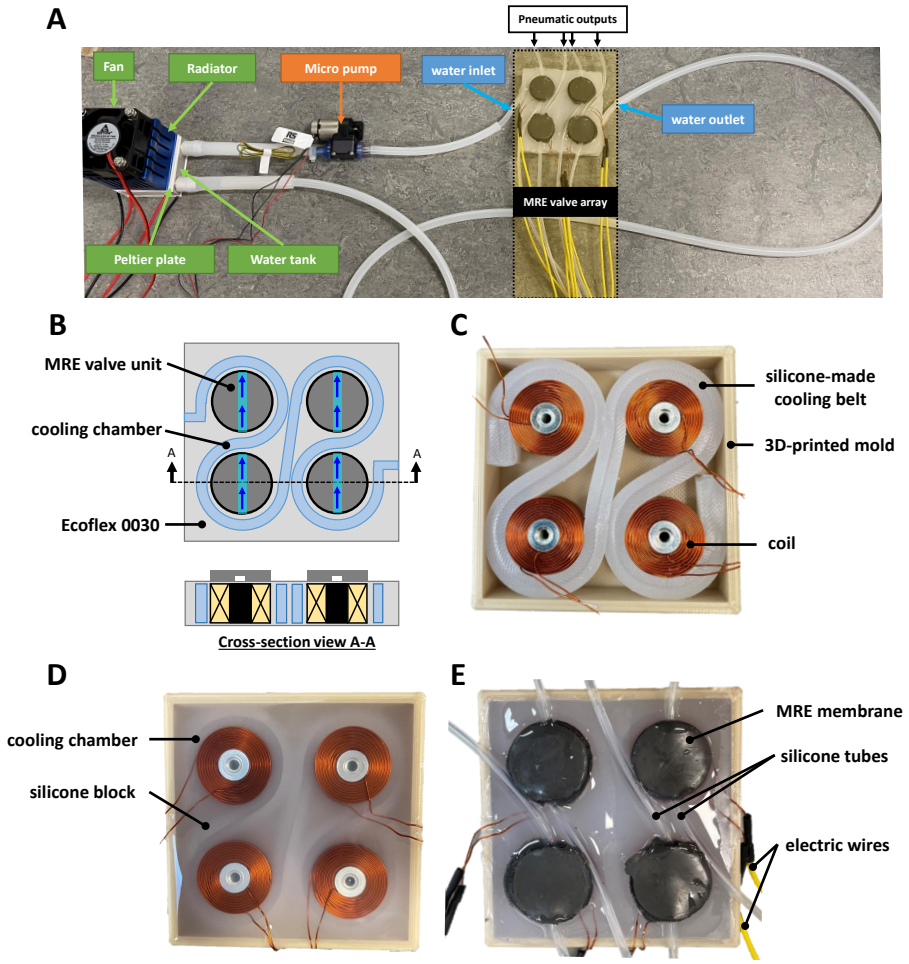


Figure 6.4: Design and fabrication of the MRE valve array and its cooling system. **(A)** shows a photo of the MRE valve array and its cooling system. The yellow block shows the MRE valve array consisting of four MRE valve units. The cooling chamber of the MRE valve array is connected in a loop with a micropump and a cooling device (a fan, a radiator, two Peltier plates, and a water tank). Cooling water is driven by the micropump, bringing the heat generated by the MRE valve array to the cooling device, so that it maintains the valve array at a safe temperature. **(B)** shows the top and cross-sectional view of the MRE valve array. **(C)** to **(E)** shows the fabrication process of the MRE valve array. Firstly, a cooling belt with a rectangular internal chamber was fabricated. It was then placed together with four coils into a mold as shown in **(C)**. Next, the silicone is poured into the mold and covers the coils and the cooling belt, as shown in **(D)**. Finally, the MRE membrane is fabricated on top, and silicone tubes are attached, as shown in **(E)**.

by maximizing contact area with the valves, and ease of manufacture by having only one single cooling channel without any forks. The cooling chamber has a rectangular cross-section of 8 mm × 2 mm. Water is filled into the chamber and driven by a micro pump to ensure sufficient flowrate.

A cooling device was used to cool down the fluid after the heat was exchanged with the coils. As presented in Fig. 6.4(A), the cooling device consists of a tank, two Peltier plates, a radiator, and a cooling fan. The tank, Peltier plates, radiator, and cooling fan had the same contact area of 40 x 40 mm for seamless matching. Thermal conductive double-sided adhesive tape is used to attach them together. Silicone tubes were used to connect the pump, cooling device, and MRE valve array together into a loop.

The fabrication procedure of the MRE valve array is shown in Fig. 6.4(C)-(E). Firstly, a silicone cooling belt with an internal chamber was fabricated. Four coils and the pre-fabricated cooling belt were then placed together in a rectangular mold. Uncured silicone is then poured inside for casting the base layer of the MRE valve. After fabricating the base layer, we fabricated the MRE layer directly on top of the base layer as four independent circular pieces. The method of making the air channels between the base layer and the MRE layer was the same as our previous work when fabricating a single MRE valve unit [85]. Mylar strips (2 mm width, 0.075 mm thickness) were placed between the electromagnets and the MRE membrane before curing and later removed to create an air channel. The overall size of the MRE valve array is 60 $\times$ 60 $\times$ 15 mm.

6.4 Results

To prove the validity of the proposed design, the fabricated MRE valve array (30 mm valve spacing, same pole arrangement, cooling system engaged) was tested in terms of both magnetic interference and heat dissipation. Lastly, the fabricated MRE valve array was used to control the actuation of a multi-chamber soft pneumatic robot.

6.4.1 Magnetic interference

To investigate the amount of magnetic flux leaked to the surrounding environment, a hall sensor (SS490, Honeywell) was perpendicularly placed between two adjacent valve units on top of the MRE membrane to measure the magnetic flux density. The current was then applied to the two valves from 0 to 3A with 0.5 A steps. Both

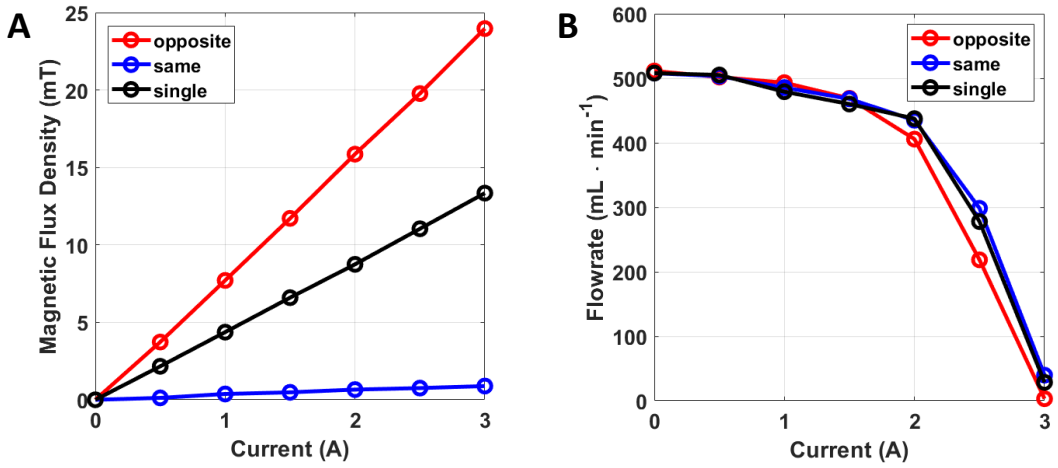


Figure 6.5: Experimental results about the magnetic interference of the MRE valve array. **(A)** shows the measured magnetic flux density in the middle of two MRE valve units under different amounts of electric current and different pole arrangements. The magnetic field shows good linearity along with the current. **(B)** shows the measured flowrate through the valve channel under different amounts of electric current and pole arrangement.

the "same" and "opposite" pole arrangements were tested by changing the current direction, and the corresponding results are presented in Fig. 6.5(A).

As shown in Fig. 6.5(A), the measured magnetic flux density increases linearly as the electric current increases. When applying the same pole arrangement, the magnetic field is significantly less than the opposite pole arrangement. This is consistent with the simulation results presented in Fig. 6.2. The maximum magnetic field for the "opposite" and "same" pole arrangements is 24.0 mT and 0.89 mT, respectively. Our findings in Fig. 6.5(A) confirm that the magnetic interference between the MRE valve array and its environment can be sufficiently suppressed when the same magnetic polarity is applied with a valve spacing of 30 mm.

The second aspect investigated in terms of magnetic interference is whether the flowrate characteristics of a particular MRE valve in the array are affected by the operation of its neighboring valves. In this evaluation, we measured the flowrate characteristics of a random MRE valve unit in the array while its neighboring valves were operating with either the same or the opposite polarity. The measured flowrate characteristics were then compared with the flowrate characteristics of a single MRE valve as the benchmark. The upstream pressure applied to the valve

channel was kept at 15 kPa, while the downstream was directly connected to the atmosphere. The electric current applied to the tested MRE valve ranged from 0.5 to 3 A with 0.5 A steps. The result is represented in Fig. 6.5(B).

As shown in Fig. 6.5(B), the flowrate decreases as the current increases since the MRE membrane is attracted closer to the electromagnet under the larger magnetic field. The opposite pole arrangement brings a lower flowrate profile when compared with the benchmark, with a Root Mean Square Error (RMSE) of 27.9 mL/min. This matches our simulation results (Fig. 6.2) which tell that the magnetic flux density along the air channel is larger with opposite pole arrangement. On the other hand, the measured flowrate profile with the same pole arrangement is desirably closer to the benchmark, with an RMSE of 9.73 mL/min. This indicates that, with the same pole arrangement, the behavior of each MRE valve unit in the array stays independent from each other without magnetic interference. The results presented in Fig. 6.5(B) further verify that the same pole arrangement is more suitable for designing the MRE valve array here.

6.4.2 Heat dissipation

In the heat dissipation evaluation, we measured the temperature response of the MRE array with and without the cooling system. A thermal camera (Fluke Ti100) was used to capture thermal images. The initial temperature was set to the ambient temperature of 25 ^{o}C. Two phases were investigated during the tests, a working phase and a cooling phase. During the working phase, all 4 MRE units in the array were supplied with an electric current of 2 A. During the cooling phase, the current in the valves was shut down. The working and cooling phases lasted 5 and 10 minutes, respectively. Thermal images were recorded in the working and cooling states every 10 s and 60 s, respectively.

The captured thermal images are shown in Fig. 6.6. The temperatures on two particular points are stated, one is at the center of the MRE valve array, while the other is at the center of a single MRE valve unit. After the entire working phase, the temperature at the center of the MRE valve unit increases from 25.8

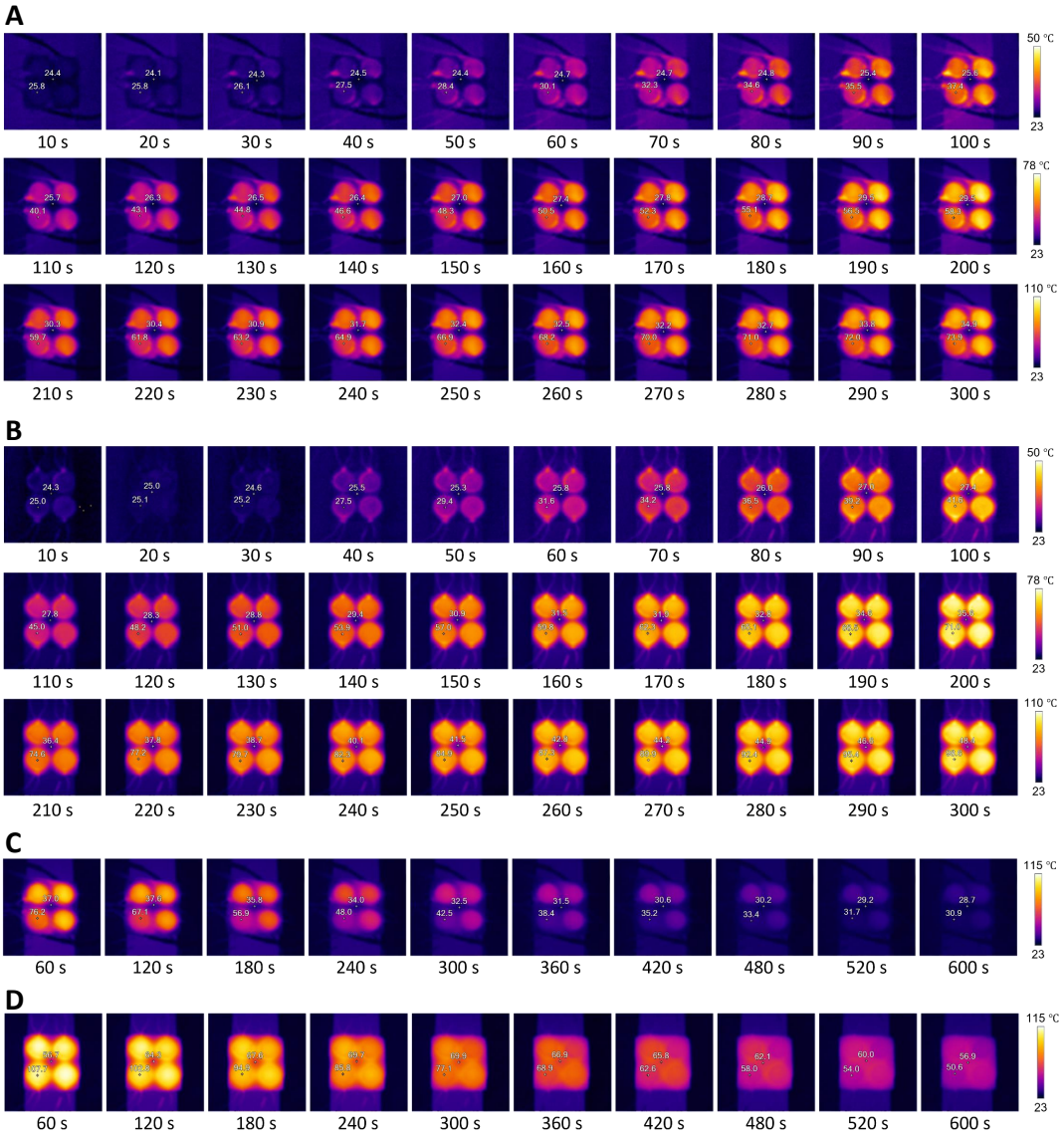


Figure 6.6: Experimental results about the heat dissipation of the MRE valve array with and without a cooling system. **(A)** shows the temperature distribution of the MRE array with a cooling system every 10 seconds during the working phase. **(B)** shows the temperature distribution of the MRE array without the cooling system every 10 seconds during the working phase. **(C)** shows the temperature distribution of the MRE array with a cooling system every 60 seconds during the cooling phase. **(D)** shows the temperature distribution of the MRE array without the cooling system every 60 seconds during the cooling phase.

to 73.9 °C with the cooling system and from 25.0 to 98.6 °C without the cooling system, respectively. The temperature at the array center increases from 24.4 to 34.9 °C with the cooling system and from 24.3 to 48.4 °C without the cooling system, respectively. The temperature of the MRE array using a cooling system

is much lower than that without a cooling system, and the difference is up to 25 °C in the center of the coil. The lowered temperature guarantees the long working life of the MRE valves and the safety of the surrounding environment.

In the cooling phase, we can observe that with the cooling system, the temperature decreases from 37.0 to 28.7 °C at the MRE valve center and from 76.2 to 30.9 °C at the center of the coil. However, without the cooling system, the whole structure becomes uniformly hot due to the thermal conduction and the temperature is around 53 °C at the end of the cooling phase, which is the same as the simulation results indicates (Fig. 6.3). The effect of the cooling belt is verified by the improved heat dissipation during both the working and cooling phases, which insists with the evaluation results and meets our goal.

6.4.3 Demonstration

The proposed MRE valve array design minimizes the effect of magnetic interference and overheating, ensuring the MRE valves in the array work steadily, independently, and safely. To illustrate its application, a soft pneumatic robot with four independent PneuNet actuators (silicone-casted bending actuators [3]) was fabricated and controlled by the MRE valve array. Each actuator was connected to an MRE valve in the array. The specific schematics can be found in Fig. 6.7(B). The valve array operated continuously and controlled the robot through different configurations for around 2 minutes. Firstly, the limbs were straightened sequentially. Next, the limbs were straightened in pairs. Finally, all the limbs were straightened together twice. The different configurations of the soft robot controlled by the MRE valve array are presented in Fig. 6.7(C)-(J). The demonstration illustrates that the proposed MRE valve array is able to control multi-chamber soft robots through various configurations.

Table 6.1 summarizes the performance of the MRE valve array when controlling four pneumatic actuators simultaneously. The performance of commonly used industrial proportional valves (FESTO valves) and rigid MRE valves [108] is also included in the table for comparison. It can be seen that the MRE valve

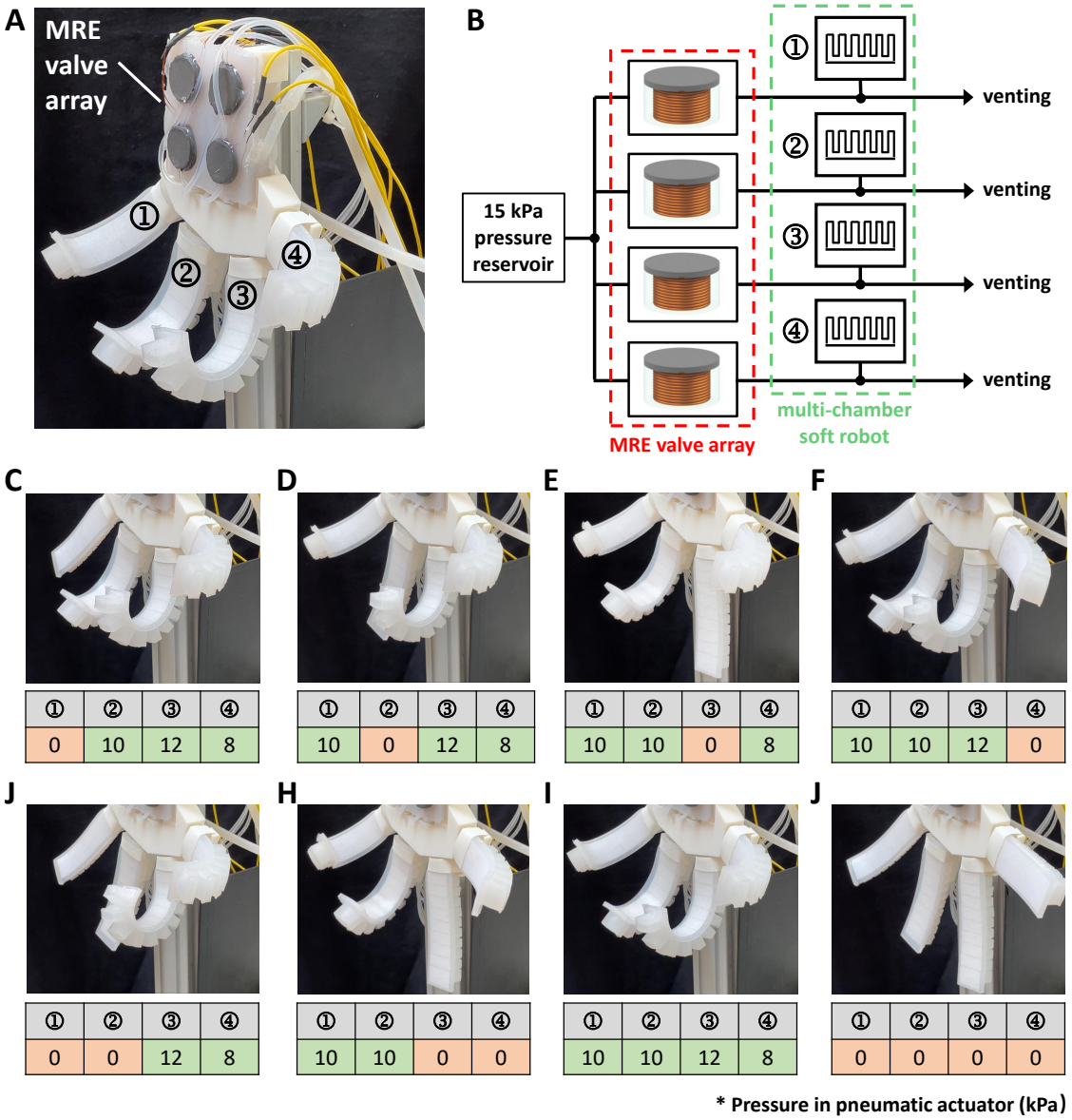


Figure 6.7: A four-chamber soft robot controlled by the MRE valve array. The structure of the robot is shown in **(A)**. It consists of four silicone-made PneuNet soft actuators. Each actuator is connected to an MRE valve unit in the array as shown in **(B)**. By activating and deactivating the valves, the soft robot exhibits different configurations. **(C)**-**(J)** shows the different configurations of the soft robot controlled by the MRE valve array, together with the pressure within each pneumatic actuator.

array presented in our work comes with the highest structural compliance and the most compact size. Although the pressure/flowrate capability is lower than that of its industrial counterparts, it's still sufficient for most soft robots based on elastomer materials.

Table 6.1: Performance of different proportional valves when controlling four pneumatic actuators simultaneously.

Work	Stiffness	Size	Max pressure	Max flowrate
Our work	10^6 Pa	60*60*10 mm	41.3 kPa	1.1 lpm
Festo valves [124]	10^9 Pa	85*60*72 mm	100 kPa	5 lpm
Rigid MRE [108]	10^9 Pa	80*00*60 mm	85 kPa	6.2 lpm

6.5 Conclusions and future work

In this study, we proposed an MRE valve array design that enables each valve unit to work independently and steadily over long-term operation. Through investigating the magnetic interference and overheating problem, we designed the distance between each MRE valve unit (30 mm), the magnetic pole arrangement (same polarity), and the cooling system (S-shape cooling chamber with forced liquid). The physical experiments verified that the proposed MRE valve array could eliminate the effect of magnetic interference. Results also showed that the cooling system efficiently dissipates the heat generated from the coils and maintains the temperature at a lower level. Finally, a demonstration was presented to illustrate the applications of the MRE valve array when controlling multi-chamber soft robots.

In the future, with the increase of DOFs of soft robots, the number of valves also needs to be increased. The 30 mm restriction in horizontal valve spacing inevitably makes the valve array flat and huge. This restriction could be reduced by using smaller electromagnetic coils. A three-dimensional MRE valve matrix could also solve the problem. An investigation of the vertical arrangement of valves will be performed. Additionally, the adaptation of the internal cooling chamber to accommodate a 3D valve matrix will be of interest.

6.6 Supporting Information

6.6.1 Supporting Video

A video of our MRE valve array controlling multiple pneumatic actuators simultaneously is attached here: `https://youtu.be/FVkGagNZaFI`

6.6.2 Simulation settings when investigating magnetic interference

The simulation was constructed in COMSOL Multiphysics 5.6, and the specific settings are as followed:

Geometry Construction

MRE valves were constructed in COMSOL using the "Geometry" function. Same as the actual MRE valve, the created geometry also contained the iron cores, the valve coils, the silicone housing, and the MRE membrane with embedded air channels. Additionally, a block was built to cover the entire MRE valve as the surrounding environment.

Material Selection

The materials of iron cores, valve coils, silicone housing, and surrounding environment were set to soft iron, copper, silicone, and air, respectively. These are the preset materials in the COMSOL library. The relative permeability was 5000 for the iron core, 1 for valve coils, 1 for the silicone housing, 10 for the MRE membrane, and 1 for the surrounding air.

Physics Settings

"Magnetic Field" was selected as the physics study by using the "Add Physics" function. In the "Magnetic field" menu, "Ampere's Law" was selected with "relative permeability" as the magnetization model. The constitutive relation can be represented by

$$B = \mu_0 \mu_r H$$

where B is the magnetic flux density, μ_0 is the permeability of the vacuum, μ_r is the relative permeability of the materials, and H is the magnetic field strength. "Magnetic Insulation" and "Initial Values" with default settings were applied to the MRE valve body. In the "Initial Values," the "Magnetic vector potential" was set to 0. Finally, "Coil" condition was applied to the valve coils. In the

settings of "Coil", we set the "Conductor model" to "Homogenized multi-turn", the "Coil type" to "Numeric", the "Number of turns" to 400, and the "Coil wire cross-section area" to 0.35 mm.

Mesh & Study

The whole MRE valve module was meshed by selecting the "Mesh" function. The sequence type was set to "Physics-controlled mesh." And the "Element size" was set to "Finer". 2 steps were created in the "Study" section. Step 1 was "Coil geometry analysis," and Step 2 was "Stationary."

Results

After computation, a "Slice plot" with the "Magnetic Flux Density Norm" was used to obtain the simulated magnetic field presented in the paper. "Rainbow" was selected in the "Coloring and Style." Moreover, a "Line plot" was used to represent the magnetic flux density along the air channel.

6.6.3 Simulation settings when investigating thermal dissipation

The simulation was constructed in COMSOL Multiphysics 5.6, and the specific settings are as followed:

Geometry Construction

The MRE valve array with the cooling chamber was constructed in COMSOL using the "Geometry" function. Same as the actual MRE valve array, the created geometry also contained the iron cores, the valve coils, the silicone housing, the cooling chamber, and the MRE membrane with embedded air channels. Additionally, a block was built to cover the entire MRE valve as the surrounding environment.

Material Selection

The materials of iron cores, valve coils, silicone housing, cooling chamber, and surrounding environment were set to soft iron, copper, silicone, water, and air,

respectively. These are all the preset materials in the COMSOL library so that the default values of their heat capacity and thermal conductivity can be used. The thermal properties of the MRE membrane are assumed to be the same as the silicone for approximation.

Physics Settings

Firstly, both "Heat transfer in solids" and "Laminar flow" were added to the simulation. In the "Heat transfer in solids" settings, the valve coils were selected as a "Heat source" with a constant heat rate determined by Joule's Law of Heating. The cooling chamber was selected as "Fluid" with "from material" properties. The remaining parts of the MRE valve array were selected as "Solid". Another "heat flux" boundary condition was added to simulate the heat convection between the MRE valve array and its surrounding environments. The "external temperature" was set to 293.15 K while the convective heat transfer coefficient is set to 9.2 $W/(m^2K)$. In the "Laminar flow" settings, the water flow in the cooling chamber was simulated. The boundary of the chamber was selected as the "Wall", while the two ends of the cooling chamber were selected as the "Inlet" and "Outlet" respectively. The inlet used "Laminar inflow" as the boundary condition, while the "Flowrate" was set to 0.36 L/min. To couple the two physics described above, a "Nonisothermal flow" Multiphysics coupling domain was added to the model. The two independent physics created above were set as the "Fluid flow" and "Heat transfer" respectively. The "Viscous dissipation" was included in the simulation.

Mesh & Study

The whole MRE valve module was meshed by selecting the "Mesh" function. The sequence type was set to "Physics-controlled mesh." And the "Element size" was set to "Normal". A "Time-dependent" study was implemented. The output timeframe was set from 0 to 1500 seconds with a step size of 50 seconds, while the tolerance is "physics controlled".

Results

After computation, a “Slice plot” with the “Temperature” was used to obtain the simulated temperature distribution presented in the paper. “Rainbow” was selected in the “Coloring and Style.” Moreover, a “1D plot” was used to represent the temperature at the valve centre against the time of operation.

7

A Design Automation Toolbox for Pneumatic Circuits

Contents

7.1 Problem 98
7.2 Objective 100
7.3 Methodology 101
7.3.1 Modular design of the logic gates 101
7.3.2 Design automation of the pneumatic computational circuit 102
7.4 Results 108
7.4.1 Validity of the design automation algorithm 108
7.4.2 Validity of the physical output 109
7.4.3 Reliability of the printed pneumatic circuit 113
7.5 Conclusions and future work 115
7.6 Supporting Information 116
7.6.1 Supporting videos 116
7.6.2 Installation of the toolbox software 116
7.6.3 Userguide of the design automation toolbox 117
7.6.4 Detailed setup when 3D-printing the pneumatic circuit . 118
7.6.5 Algorithm for finding the simplest circuit schematic . . 119
7.6.6 Algorithm for finding all valid logic gate layout 120

7.1 Problem

Numerous integrable valves developed by the research community have been discussed in the Literature Review (Chapter 2) and also in our previous work

(Chapter 3-6). While the majority of research interests focus on optimizing the structure and fabrication of these individual valves for onboard control, much less attention has been given to integrating these devices into pneumatic circuits to perform onboard signal computation. Onboard computation is undoubtedly important as it enhances the intelligence and adaptability of soft robots. However, the process of combining these individual components into computational circuits is highly challenging in various aspects. For instance, the circuit schematics must be manually designed at first to achieve the desired input-output mapping. Bringing all the required components onboard within the limited space in the robot body also requires the user's knowledge and experience. Apart from the manual circuit design process, a manual piping process is required to securely and efficiently connect all individual units together. Each individual computation unit in the circuit is often highly similar in appearance and only distinguishable from each other based on some detailed configurations. This practical difficulty brings a high chance of human error. Problems related to redundant tubing and unreliable fittings can also affect the efficiency, response time, and durability of the systems. The above-mentioned limitations are increasingly problematic as the computation circuit becomes more complex. This raises the need for an automated toolbox that directly transforms the user-specified robot behaviours into a ready-to-use computational pneumatic circuit that fits within a certain set of space constraints. By replacing the manual circuit design, fabrication, and piping process, the toolbox can significantly enhance the accessibility of electronics-free computational pneumatic circuits. Similar design automation tools which convert the users' demands into a ready-to-manufacture file have already been developed in other research fields, such as electronic circuitry,[125] electro-microfluidic circuitry,[126] and genetic circuitry,[127] but are yet to be done for pneumatic circuits in soft robots.

There are several existing software aiding the design of pneumatic circuits. Both PneuDRAW (SMC, Japan) and FluidDRAW (FESTO, Germany) can be used for drawing pneumatic circuits concisely and easily.[124, 128] Moreover, FluidSIM (FESTO, Germany) enables users to simulate the performance and functions of a

pneumatic circuit given its schematics.[129] However, although the software listed above simplifies the manual design process, none of them can design a ready-to-use pneumatic circuit based on the desired input-output mappings. In other words, achieving full design automation still remains unsolved. More recent work on a web-based pneumatic circuit design tool makes a step towards this goal[130]. The web-based toolbox takes the user's desired robot behaviour in the form of a HIGH/LOW truth table and outputs a schematic guiding the wiring configuration. The validity of the soft compiler has been demonstrated by using a pneumatic glove to implement several soft circuits composed of soft, bistable valves. This toolbox successfully automates the circuit design process, while the manual fabrication and piping processes still exist. The migration from the software-based pneumatic circuit to its physical implementation remains unsolved due to the limitations brought by the fabrication method of those silicone-casted devices. Moreover, the work is only capable of dealing with single-output truth tables.

7.2 Objective

To solve the abovementioned problems, in this work, we aim to develop a design automation toolbox for generating 3D printable pneumatic computational circuits. The toolbox comes with a graphical user interface (GUI), shown in Figure 7.1, to take users' desired computation functions in the form of a truth table and a set of 2D space constraints. It then schedules the pneumatic circuit which performs the desired computation within the space constraints and produces a 3D-printable CAD file that can be fabricated and used directly. This capability eliminates the manual work that was previously required during circuit design, fabrication, and piping processes, therefore enhancing the accessibility of pneumatic circuits for soft robotic applications. The design automation algorithm should have versatility across different input-output mappings and space constraints, making it ready for a diverse range of soft robotic applications.

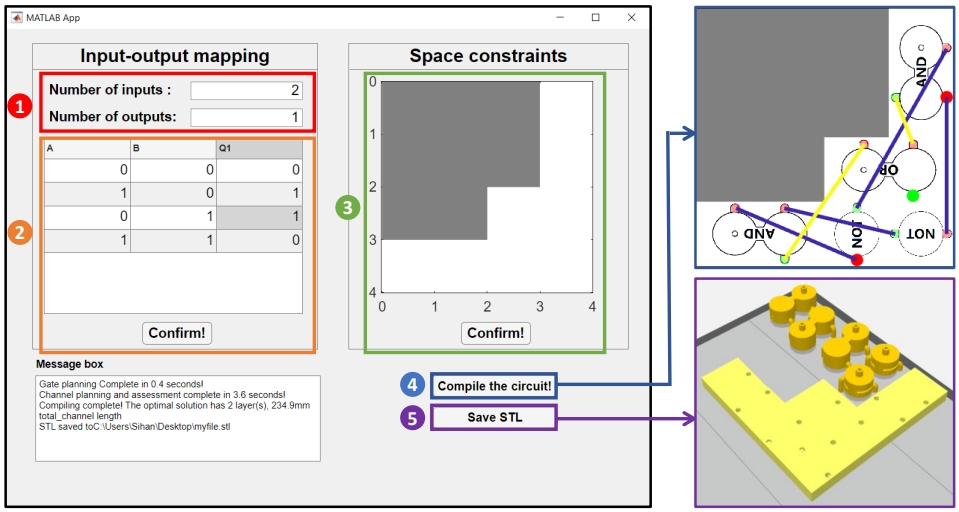


Figure 7.1: The user interface of the toolbox in MATLAB. The operation procedure is ordered here for clarity. ① indicates the region where users define the number of inputs and outputs of their desired computation. ② refers to the editable table where users define the truth table. ③ refers to the editable map where users specify the 2D space constraints of the pneumatic circuits. ④ and ⑤ refer to the buttons for planning the pneumatic circuit and saving the 3D printable CAD files, respectively.

7.3 Methodology

7.3.1 Modular design of the logic gates

In order to build the proposed computational pneumatic circuits for soft robots, the fundamental hardware components would consist of a collection of pneumatically-driven logic gates which have sufficient pressure tolerance, flow rate capability, and durability. At a minimum, one would require the design for NOT, AND, and OR gates to accomplish any user-specified truth table. This section presents the hardware design for the logic gates employed in this work.

Design

The pneumatic logic gates used in this project are built upon an existing design of 3D-printed transistors,[69] which include a normally “ON" transistor and a normally “OFF" one. We reduce the size of both transistors for higher computation density and simplify the structure of the “OFF" transistor by removing an extraneous membrane. The pneumatic “NOT" gate is constructed by using the modified normally “ON" transistor, the pneumatic “AND" gate is constructed by combining two normally

“OFF" transistors in series, while the pneumatic “OR" gate is constructed by combining two normally “OFF" transistors in parallel. Moreover, the input and output ports of all logic gates are diverted to the bottom plane, so that all gates could be connected together into a circuit with a compact layer channel. The detailed designs are presented in Fig. 7.2(A)-(C).

Characterization

To validate the fact that the logic gate design can be used by the proposed toolbox for pneumatic computational circuits, the computation correctness and the response time of these devices were experimentally characterized. The computation correctness refers to whether the device complements the desired input-output mappings, while the response time is the time difference from the engagement of input signals to the full development of the output signal. The obtained results were presented in Fig. 7.2(D)-(I). It was shown that all three logic gates perform the computation as desired. The logic gates bring a faster response when the pneumatic signal amplitude increases. The response time of the NOT, AND, and OR gates with 40 kPa pneumatic signals are 0.63 seconds, 0.15 seconds, and 0.18 seconds respectively.

7.3.2 Design automation of the pneumatic computational circuit

The objective of the proposed toolbox is to automatically convert the desired computation functions into a 3D-printing-ready CAD file that fits within a 2D workspace defined by the user. The computation functions are given in the format of a multi-input, multi-output truth table, while each input and output is a digital pneumatic signal. This truth table format can represent the realization of various meaningful robot behaviors. The output of the compiler is in the format of a 3D-printing-ready CAD model. The CAD model can be printed out by using multi-material 3D printers with soluble supports. This enables rapid, accurate, and repeatable manufacture of pneumatic circuits for controlling a wide range of soft robots, with a minimum amount of manual work involved. Moreover, the 3D

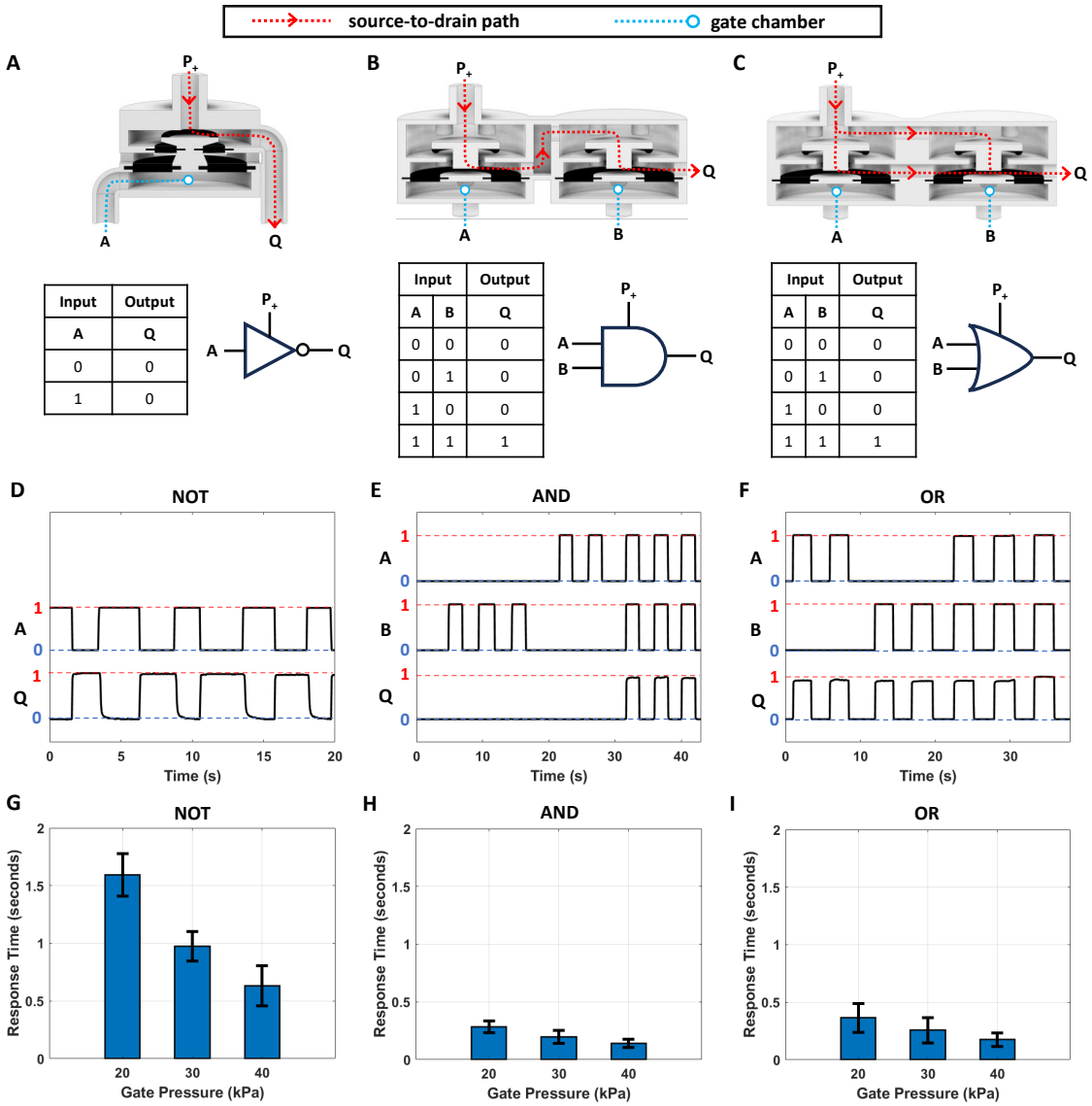


Figure 7.2: **A** shows the structure and the working principle of a pneumatic NOT gate. **B** shows the structure and the working principle of a pneumatic AND gate. **C** shows the structure and the working principle of a pneumatic OR gate. The design of these gates has been influenced by and adapted from a prior work.[69] **D-F** shows the pressure-time curve of the three logic gates at their inputs and outputs. The response time of each logic gate under pneumatic inputs with different amplitudes is presented in **G-I**.

printable pneumatic circuit can be printed inside the soft robot body, opening up the potential for an untethered robotic system with onboard computation. The proposed toolbox is based on MATLAB and Comsol. The former is used for building GUI and compiling circuit payout, while the latter is used for converting the planned layouts into 3D printable CAD files. The user interface of the toolbox is illustrated in Figure 7.1, while Figure 7.3 provides an overview of the circuit planning procedure.

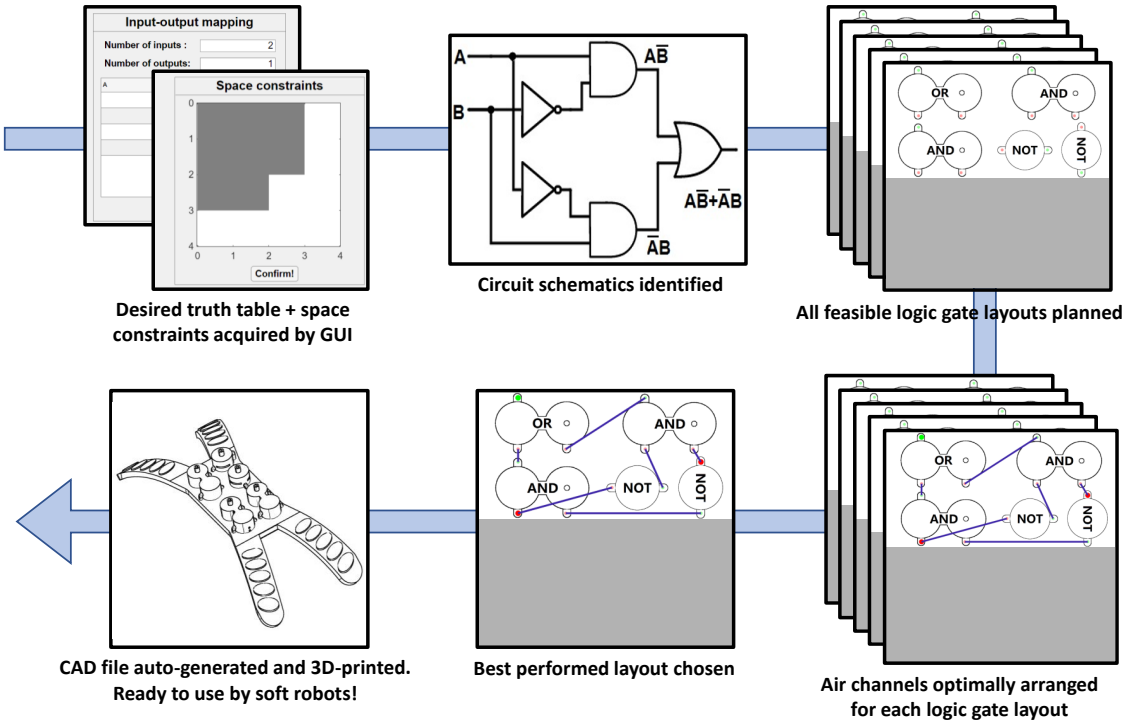


Figure 7.3: An overview of the pneumatic computation circuit design toolbox that converts the desired computation functions into a 3D-printing-ready CAD model directly. The toolbox enables rapid design and manufacture of the computational pneumatic circuits for a wide range of soft robots, with minimum manual work involved.

The subsequent sections will delve into the details of this procedure.

Circuit schematics identification

The first step during compilation is to convert the user-input truth table into a schematic that tells the minimal type/number of the logic gates required and how the gates should be connected into a circuit to achieve the desired computation. The input truth table is initially converted into logic expressions via the sum-of-product (SOP) algorithm. For each row in the truth table with a HIGH output, the SOP algorithm generates a logic expression based on the inputs in that row. It then combines all these logic expressions with OR operators. The raw output of the SOP algorithm is often highly complex. The inefficient logic expressions bring redundant logic gates and air channels into the circuit, increase the circuit size/weight, slow down the circuit response, and bring additional complexity into the following compiling process. To address these issues, the logic expressions

Table 7.1: Detailed properties inside the “PneuSignal" data structure. Each “PneuSignal" represents

Properties	Meaning
Value	Logic expressions of this pneumatic signal
Up	The logic gate located upstream of this pneumatic signal
Down	The logic gate(s) located downstream of this pneumatic signal

are simplified to their simplest forms via Matlab Symbolic Toolbox to minimize the number of logic gates used. The simplified expressions are then converted to postfix notation for the ease of further processing.

A customized data structure “PneuSignal" is used to represent the circuit schematic. Each “PneuSignal" describes the information about an air channel in the circuit (may contain forks) located between logic gates or the circuit inputs/outputs. All properties inside a “PneuSignal" and their meaning are described in Table 7.1. By identifying all “PneuSignals" involved in a pneumatic circuit, the whole schematic is effectively obtained. The algorithm used to convert the postfix logic expressions into all “PneuSignal" involved in the circuit is described in Supporting Information S2.

Logic gate layout planning

The logic gate layout determines the placement (e.g., position, orientation) of each logic gate within the 2D workspace. The backtracking algorithm is used to find out all possible logic gate layouts that fit within the user-input 2D workspace. This is essential for ensuring that the best solution is ultimately found after the planning and assessment of air channels. The usage of the backtracking algorithm is highly common in compiler design due to its simplicity in programming, low space complexity, and compatibility to solve almost all kinds of problems.[131, 132] To simplify the problem and reduce the algorithm complexity, the user-input 2D space constraints are modeled as an m*n matrix within which only certain entries are available for gate placement. Each AND/OR gate requires two adjacent available entries to be placed while each NOT gate requires only one available entry. The detailed implementation of the backtracking method for logic gate layout planning is described in Supporting Information S3.

Air channel layout planning

The objective of this step is to plan the air channel layout for each valid logic gate layout obtained in the previous steps. The air channels are designed to connect all logic gates and inputs/outputs in the circuit together according to the circuit schematic. The Bentley-Ottmann algorithm is used here to detect any intersected air channels with the lowest complexity.[133] These intersected channels will be placed at different layers to ensure each pneumatic signal stays independent from the others. The greedy algorithm is then used to generate the optimal air channel arrangement which has the least total number of layers while ensuring no intersected channels are within the same layer. Note that each different logic gate layout has its own optimal channel layout, which will be evaluated in the following step.

Optimal layout assessment

The candidate solutions obtained from previous steps are examined through the following aspects:

- **The minimum distance between any pair of independent channels must be larger than a threshold value to prevent signal interference caused by leaking.** This threshold value depends on the manufacturing precision and required robustness of the pneumatic circuit. This acts like a solid constraint, meaning that any pneumatic circuit which fails to satisfy this criterion will be rejected for further assessment.

- **The optimal solution should have the least number of layers.** Any unnecessary addition in the total layer number thickens the overall system, increases the fabrication time/cost, and slows down the system response.

- **The optimal solution should have the lowest total air channel lengths.** This reduces the internal volume within the computational systems, therefore minimizing the response time and energy consumption during operation. It also reduces the time required for post-printing support dissolving.

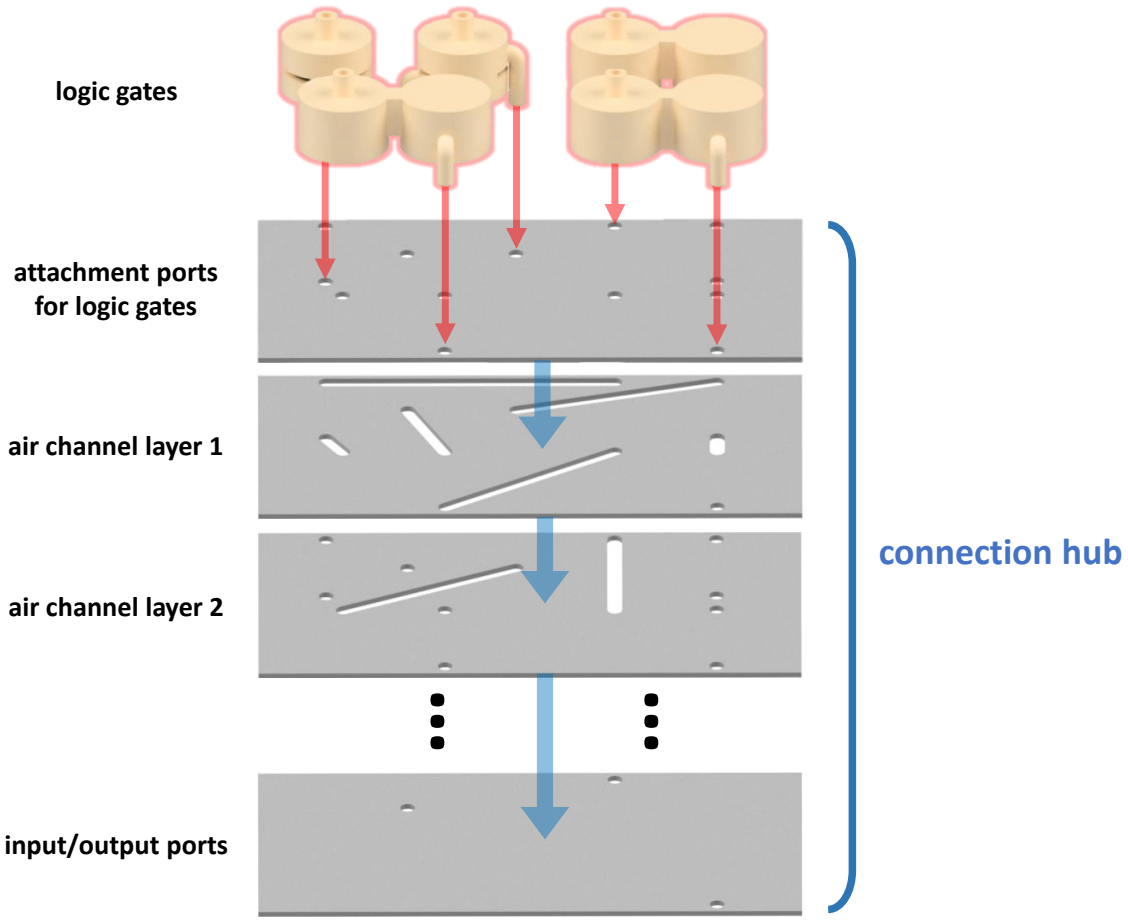


Figure 7.4: The detailed hardware structure of the computational circuit. A connection hub is used to connect all logic gates into the circuit. It includes some attachment ports for fitting with the logic gates on top, air channels in the middle, and a set of input/output ports that connects to the input and output pneumatic signal of the entire computation circuit.

3D printable CAD model generation

After determining the exact arrangement of all logic gates and air channels, the final step is to gather all information and correspondingly generate a 3D printable CAD file of a soft connection hub. The connection hub comes with embedded air channels that facilitate the interconnection of all individual gates, forming the complete pneumatic circuit. The connection hub comes with a) attachment ports on the top to attach the logic gates according to the pre-planned layout; b) the pre-planned air channels for signal communication between logic gates and; c) ports on the bottom as the total inputs/outputs of the entire computational circuit. The specific structure of the hub is shown in Fig. 7.4. Its fabrication is feasible as long as the

3D printer has the capability to print both soluble support and airtight membranes. Once the CAD file of the soft connection hub is fabricated, the modular logic gates can then be attached directly to the hub without requiring any tools. The compliance of the connection hub and the press fit tolerance between the connection hub ports and the logic gates port ensure reliable fitting and prevent leakage.

Comsol Multiphysics via Livelink for Matlab is used here to automatically generate such a three-dimensional CAD file based on the pre-acquired information. Comsol is chosen due to its seamless integration with Matlab, popularity in the soft robotics community and the potential to be used for further Finite Element (FE) simulation. The toolbox first generates a layer with only ports located at the inputs and outputs of the entire circuit. It then proceeds to create the air channel layers as specified by the pre-acquired layout. Note that there could be more than one air channel layer, in which case different air channel layers will be isolated by dummy membranes. Lastly, according to the pre-planned logic gate layout, the algorithm generates a layer with ports located at the inputs and outputs of all logic gates. All generated layers are stacked together, forming the overall CAD file of the connection hub.

7.4 Results

7.4.1 Validity of the design automation algorithm

To explore the versatility of the design automation algorithm across different input-output mappings and space constraints, the truth tables for two commonly used digital computations, namely XOR and 1:4 de-multiplexer, were inputted into the toolbox, alongside with different space constraints. XOR is chosen here due to its capability to perform various crucial logical operations, facilitate error detection and enable arithmetic operations. 1:4 de-multiplexer is chosen here to demonstrate the compatibility of the toolbox algorithm when dealing with multiple-output truth tables. The pneumatic circuits planned by the algorithm to achieve XOR and 1:4 de-multiplexer within different 2D workspaces are presented in Figure 7.5 and 7.6, respectively.

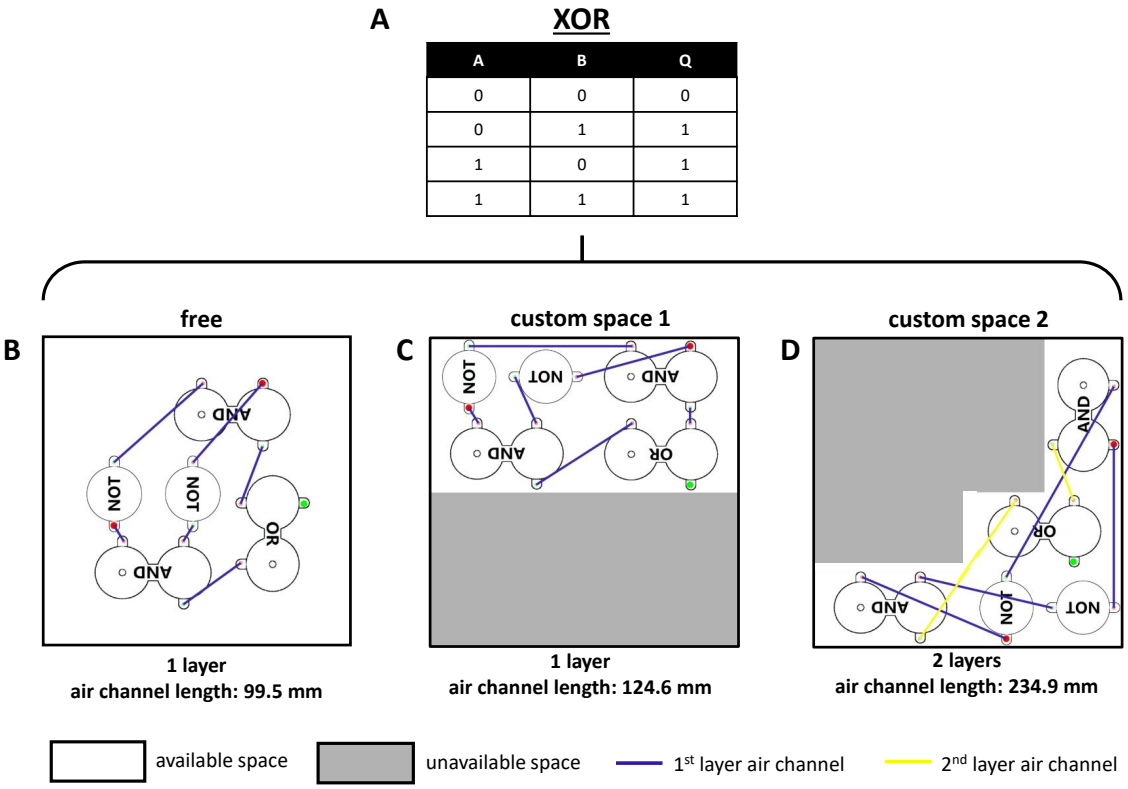


Figure 7.5: Pneumatic circuits under different space constraints scheduled by the toolbox to achieve an XOR computation. **A** presents the user-input truth table taken by the toolbox. **B - D** present the different pneumatic circuits scheduled by the toolbox under different space constraints provided by users. The available workspace is indicated in white while the unavailable workspace is in gray. The color of each air channel indicates which layer it should be placed within. The larger red dots and green dots represent the inputs and outputs of the entire computational circuit, respectively.

These results show that the algorithm is able to correctly compile the pneumatic circuits with a minimum number of logic gates while keeping all air channels and logic gates within the given workspace. All intersected pairs of air channels are correctly placed in different layers. It was also noted that, for a given truth table, the total number of layers and the total length of air channels inevitably increase when more strict space constraints are engaged.

7.4.2 Validity of the physical output

The auto-generated CAD file of the pneumatic circuits in Section 7.4.1 were fabricated by a Poly-jet multi-material 3D printer (J735, Stratasys, USA). The performance of these circuits was then tested physically with respect to their

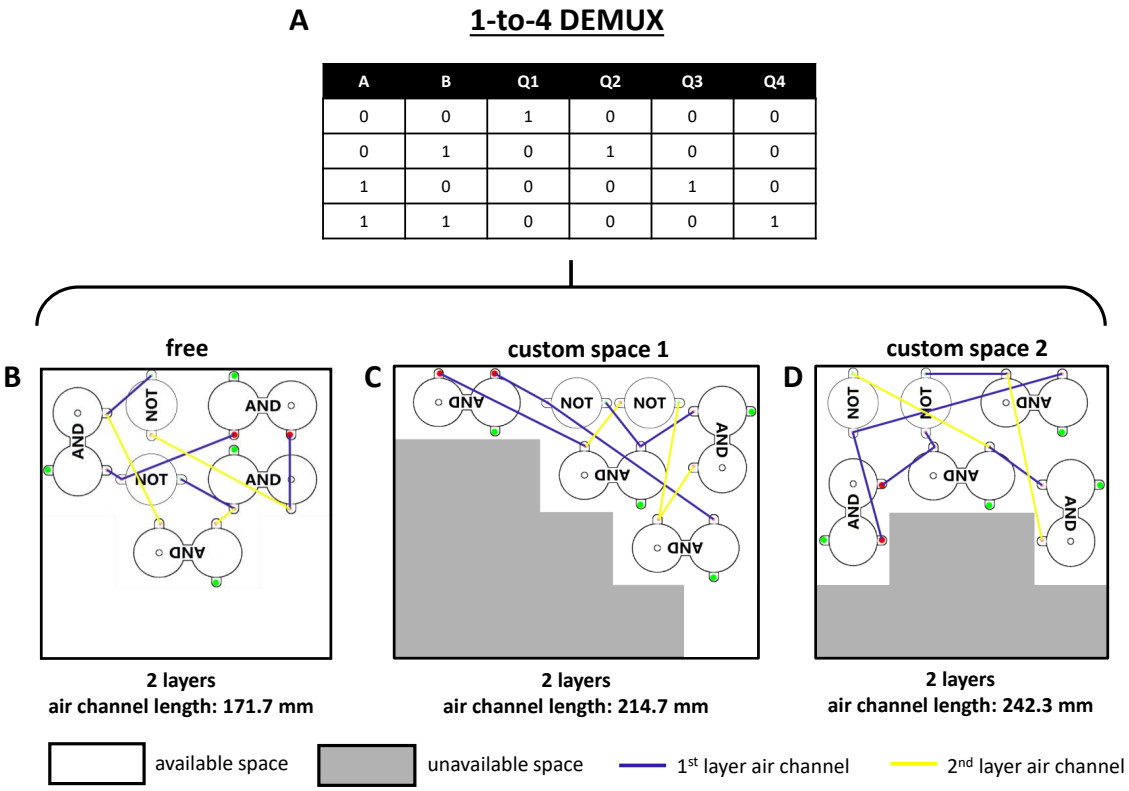


Figure 7.6: Pneumatic circuits under different space constraints scheduled by the toolbox to achieve a 1:4 DEMUX computation. **A** presents the user-input truth table taken by the toolbox. **B - D** present the different pneumatic circuits scheduled by the toolbox under different space constraints provided by users. The available workspace is indicated in white while the unavailable workspace is in gray. The color of each air channel indicates which layer it should be placed within. The larger red dots and green dots represent the inputs and outputs of the entire computational circuit, respectively.

computational correctness, response time, and long-term durability. Computational correctness describes whether the physical circuit is able to correctly implement the user-input truth table. This was tested by applying different pneumatic inputs into the circuits and monitoring the corresponding output signals. The response time is also crucial as the computation speed determines the responsiveness and agility of the soft robots controlled. It was measured as the time duration from the change in the input signal to the change observed in the output signals. Long-term durability under different operating frequencies was also investigated in terms of computation accuracy over repeated cycles. The experimental results of the physical XOR and 1:4 de-multiplexer circuits with different space constraints are presented in Figure 7.7 and 7.8.

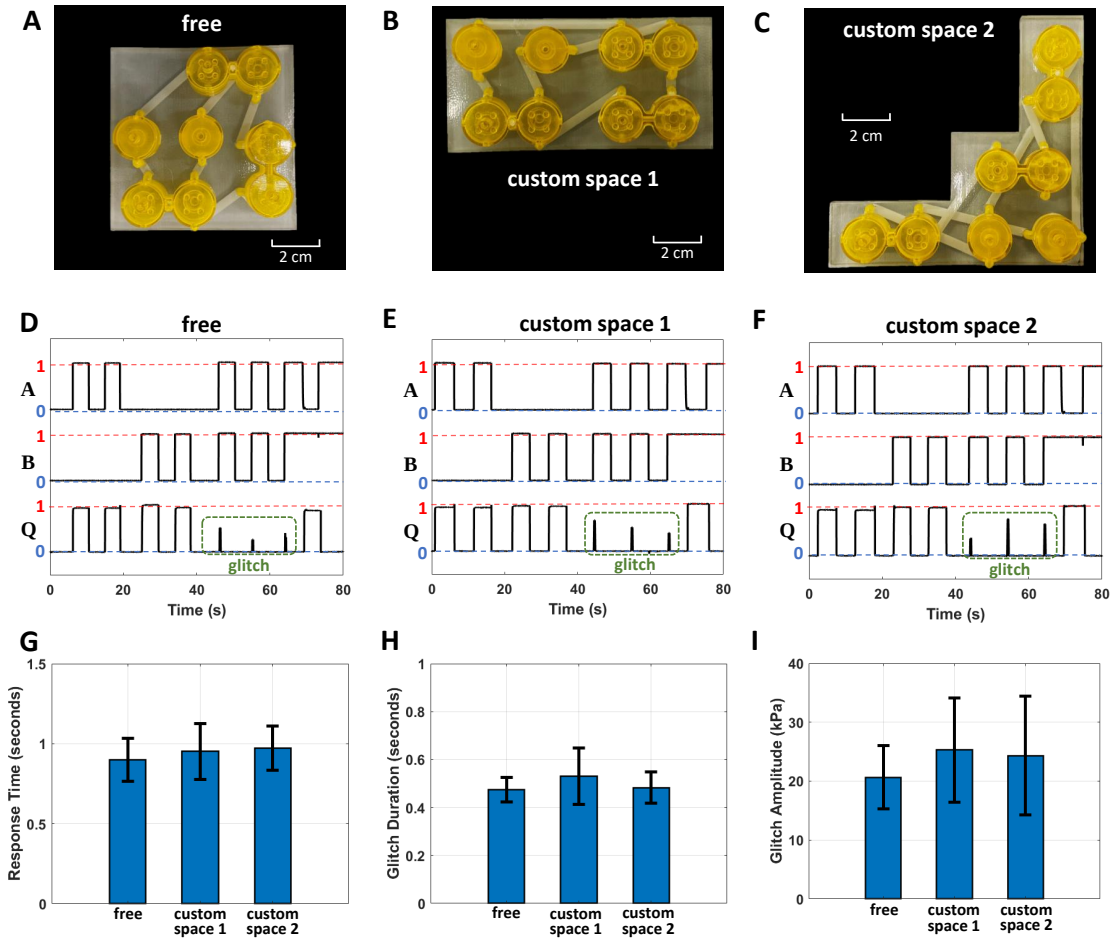


Figure 7.7: **A-C** represent the three different fabricated pneumatic circuits to achieve XOR computation, scheduled by the toolbox as previously to suit different space constraints. **D-F** present the pressure-time curve of each pneumatic circuit at their inputs and outputs, showing the correct implementation of the desired truth table. **G** presents the response time of each of the fabricated circuits. **H** presents the duration of the undesired “glitch" observed in each circuit. **I** represents the pressure amplitude of the “glitch" observed in each circuit.

Figure 7.7 (A)-(C) shows the three actual XOR circuits fabricated from the CAD files generated by our toolbox as shown in Figure 7.5. The time-series input and output pressure readings in Figure 7.7 (D)-(F) show that all these circuits correctly implement the desired truth table. The pneumatic circuits were tested with 10 repeat trials while the recorded response time for each circuit is shown in Figure 7.7 (G). It can be seen that the pneumatic circuit scheduled without any space constraints has the fastest response due to its shortest air channel lengths and least number of layers. “Glitches" were observed during the operation of all

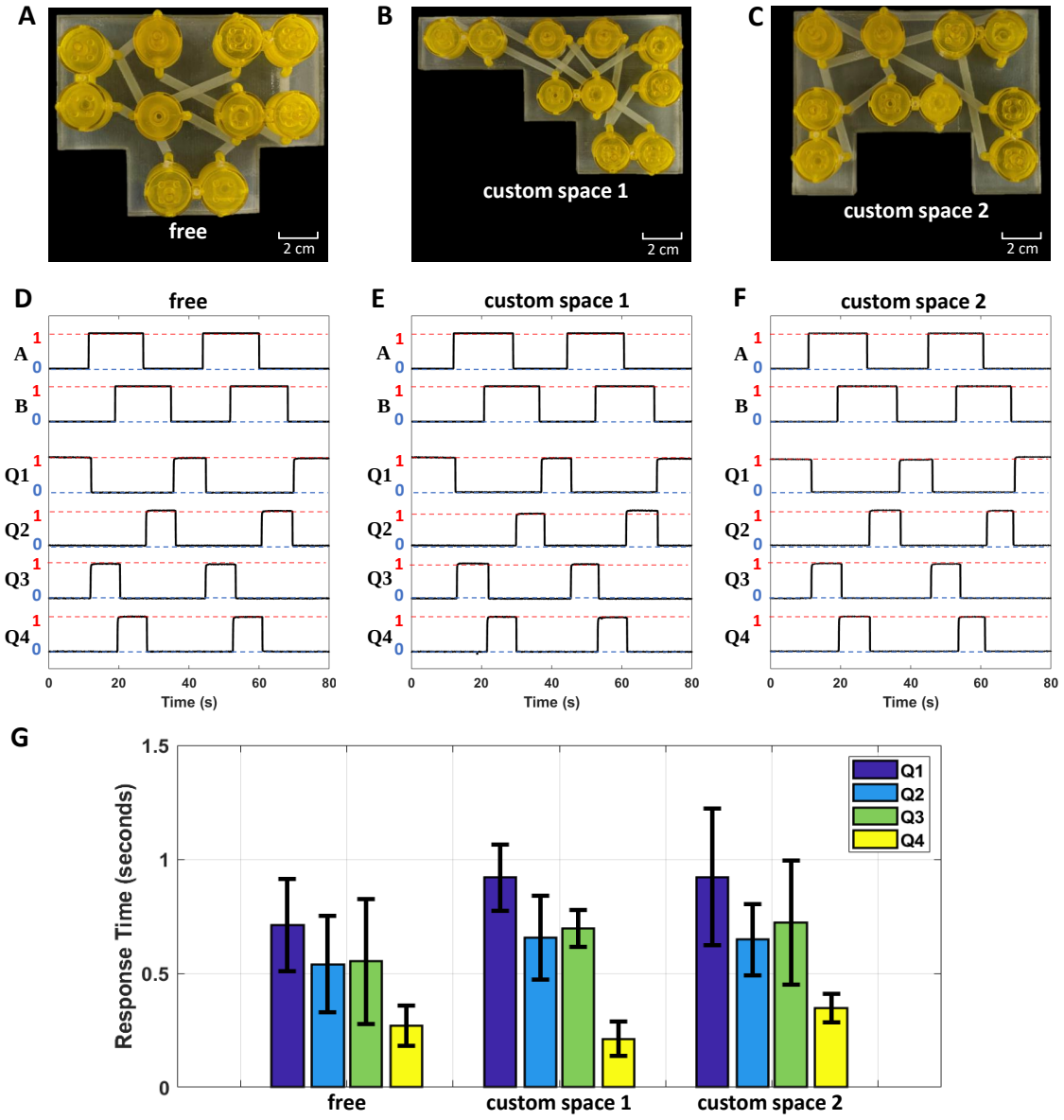


Figure 7.8: **A-C** represent the three different fabricated pneumatic circuits to achieve the 1:4 de-multiplexer, scheduled by the toolbox as previously to suit different space constraints. **D-F** present the pressure-time curve of each pneumatic circuit at their inputs and outputs, showing the correct implementation of the desired truth table. **G** presents the response time of the four outputs measured from the different pneumatic circuits.

three XOR circuits in the form of unwanted spikes when both input signals are HIGH. The unwanted pneumatic spikes are caused by propagation delays when signals take different paths with different numbers of components before reaching the same output. The duration of the glitch in this XOR circuit should in theory be similar to the response time of a single NOT gate, which matches our measured value of 0.46 seconds as shown in Figure 7.7(H). The measured amplitude of the

glitches is also presented in Figure 7.7(I). The average glitch amplitude is measured as 22.6 kPa, which is 56.5 % of the source pressure. In real soft robotic applications, this glitch amplitude will be much smaller because the pneumatic chamber of the actuator acts as a capacitor which slows down the pressure rise. The compliant nature and the generally slow mechanical response of the soft pneumatic actuators also reduce the severity of the glitch. If precise timing is indeed required, the glitch can also be solved by adding repeaters or buffers to balance the signal propagation delay in each path. However, it should be noted that this delay-matching approach has not been addressed in the design automation algorithm described in this work.

Figure 7.8 (A)-(C) shows the three actual 1:4 DEMUX circuits fabricated from the CAD files generated by our toolbox as depicted in Figure 7.8. The time-series input and output pressure readings in Figure 7.8 (D)-(F) indicate that all these circuits correctly implement the desired truth table. The pneumatic circuits were tested with 10 repeat trials while the recorded response time of each output in each circuit is shown in Figure 7.8 (G). In general, the pneumatic circuit with the least air channel lengths comes with the fastest response as it has the least propagation delay. The output Q4 (only HIGH when both inputs are HIGH) has the lowest response time with an average value of 0.28 seconds since there's no NOT gate located at its upstream path, while the output Q1 (only HIGH when both inputs are LOW) comes with the highest response time of 0.82 seconds due to the NOT gates located on its upstream paths.

7.4.3 Reliability of the printed pneumatic circuit

The long-term reliability of the pneumatic circuits was investigated through cycling tests, where different input signals were supplied to the circuits repeatedly and the output pneumatic signals were recorded. The computation accuracy, defined as the number of correct computations in every 100 cycles, was plotted against the cycle number to reflect the durability of the pneumatic computation circuits. For each computation circuit, two different frequencies were used to perform the fatigue tests. With the lower frequency, the time duration of each input signal is

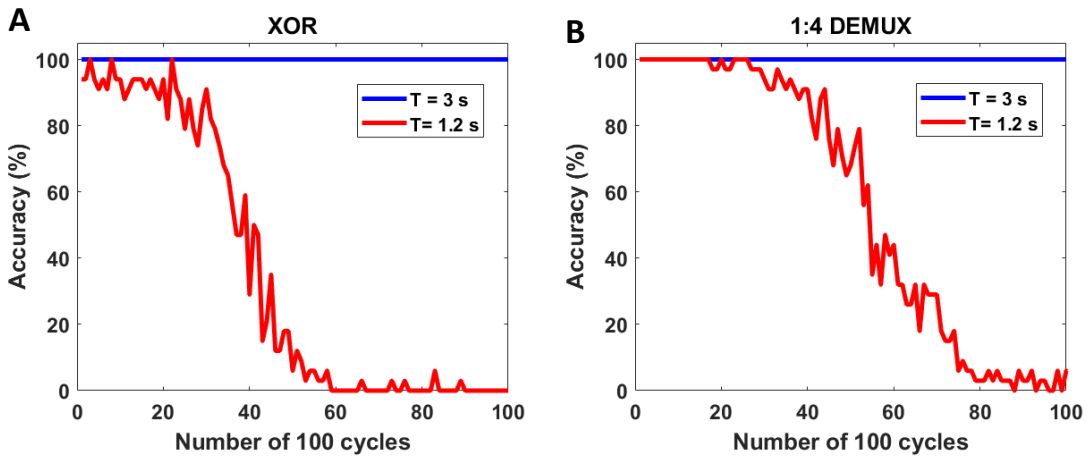


Figure 7.9: Results of the fatigue tests. **A** and **B** represent the long-term computation accuracy of the XOR and 1:4 DEMUX circuit, respectively. The tests were performed with different input signal durations to investigate the circuits' durability under different computation frequencies. Each data point in the plots refers to the number of correct computations within 100 cycles.

3 seconds, which is much higher than the response time of the circuit itself. The circuit should not fail under this frequency unless structural failure happens. With the higher frequency, the time duration for each input signal is 1.2 seconds, only slightly higher than the response time of the circuit itself. This test aims to find out how the responsiveness of the circuit evolves over usage since the circuit will fail under this frequency even with a small degradation in responsiveness. The fatigue test result is shown in Figure 7.9.

It can be seen that both the XOR and 1:4 DEMUX circuits successfully pass through 10000 cycles with 100% computation accuracy under the lower frequency (signal duration T = 3 seconds). No structural failure was observed after the fatigue tests. For the fatigue tests with higher frequency, it can be seen that the responsiveness of both circuits degrades over usage. The computation accuracy of the XOR circuit drops below 10% after around 5000 cycles, indicating that the response time of the circuit is longer than the input signal duration of 1.2 seconds. The 1:4 DEMUX circuit has a slower degradation in response time, compared with the XOR circuit. Its computation accuracy under high frequency drops below 10% after 8000 cycles. This observed degradation in response time should be considered when applying these circuits in long-term and high-frequency computation scenarios.

7.5 Conclusions and future work

This work presents a design automation toolbox that generates a 3D-printable computational pneumatic circuit to achieve a desired truth table while adhering to certain space constraints. Unlike the previous work, which solely converts user-input truth tables into conceptual circuit diagrams, this study goes a step further by accomplishing the transition from software-based circuit schematics to their physical copies. This is achieved by accurately positioning logic gates and air channels, taking into account workspace constraints, fabrication limits, material cost, and system complexity. The toolbox has the capability to replace the manual circuit design, fabrication, and piping process that used to be highly challenging and time-consuming. The automated approach also eliminates redundant tubing and unreliable fitting, therefore enhancing the responsiveness and durability of the computational circuit.

The current toolbox architecture offers the flexibility to be adapted with various types of pneumatic logic gates, provided that these devices can be 3D-printed. This can be achieved by inputting the dimensions of these new devices into the algorithm. Furthermore, the criteria for selecting the optimal circuit can be easily customized to align with different applications. The computational power required by the toolbox is kept low since the circuit planning is executed in a 2D manner, ensuring its usability across a broad range of scenarios. Regarding the scalability of the code, the toolbox typically schedules a circuit with no more than 10 logic gates within seconds, while the scheduling time extends to several minutes for circuits involving 50 logic gates. Pneumatic circuits with even more gates are impractical due to the manufacturing limits, and as such, fall outside the scope of this work.

There are still various avenues for future development that can build upon the current toolbox architecture. Firstly, the current toolbox chooses the optimal circuit layout only based on the minimum number of layers and least channel lengths. More diverse cost functions can be introduced in the future, such as Centre of Mass (CoM) positioning, input-output port positioning, and so on. Secondly, the current work does not consider the glitches caused by the different signal

propagation delays in different paths. Introducing the delay matching function based on pneumatic buffers could solve the glitching issue. Lastly, the current toolbox schedules the circuits in a 2D manner, where all logic gates are located in the same plane. This brings limitations when applied to more complex and large-scale systems. 3D circuit scheduling could be addressed in the future to further broaden its applications in soft robots.

7.6 Supporting Information

7.6.1 Supporting videos

A video userguide of our design automation toolbox is attached here: `https://www.youtube.com/watch?v=u6U-YVwS2gU`
A video showing the 1:4 de-multiplexer circuit generated by our design automation toolbox is attached here: `https://youtu.be/YOqJNM9pI1c`

7.6.2 Installation of the toolbox software

The toolbox proposed in this work requires Matlab (R2018a or newer) and Comsol MultiPhysics (Version 5.6 or newer, comes with LiveLink with Matlab) installed beforehand. The following packages must be installed on Matlab to run the toolbox correctly.

- Image Processing Toolbox
- Signal Processing Toolbox
- Symbolic Math Toolbox

The procedure to set up and run the proposed toolbox is as follows:

- Clone and install the following repository: `https://github.com/sihanwang0318/Pneumatic_compiler_toolbox.git`

- Run "Comsol Multiphysics with Matlab". This starts a LiveLink(TM) for MATLAB(R) client.
- In MATLAB, change the current folder to the path of the installed toolbox.
- Run the "toolbox.mlapp" file to launch the toolbox.

7.6.3 Userguide of the design automation toolbox

Once installed and correctly set up, the toolbox comes with a graphical user interface as shown in Figure 7.1. The following procedures are implemented when using this toolbox for designing pneumatic computational circuits for soft robotic applications:

1. Define input/output number: The first step is to tell the toolbox how many inputs and outputs are included in your desired truth table. The toolbox will automatically generate a truth table below based on these numbers.

2. Edit the truth table: The default truth table generated by the toolbox has LOW output at all times. This needs to be modified to suit the user's desired input-output mapping by directly editing the table. Any non-zero value in the cell will be treated as a HIGH signal, while zero will be treated as a LOW signal.

3. Define the available 2D space: The space constraints should be input through the editable 2D map. Available space is represented by white, while the unavailable space is represented by dark grey. The availability of each unit can be switched by direct clicking, therefore enabling the user to customize the available workspace to suit different applications.

4. Plan the pneumatic circuit: Once the input-output mapping and space constraints are all set, the user can click the “Compile the circuit!" button. The design automation algorithm will then schedule the pneumatic computational circuit to achieve the desired truth table within the space constraints while minimizing the number of air channel layers and air channel lengths. The generated circuit schedule will then be displayed in the user interface, indicating the placements of all logic gates and the air channels. The color of each air channel indicates which

layer it should be placed within. The larger red dots and green dots represent the inputs and outputs of the entire computational circuit, respectively.

5. Generate the ready-to-print CAD files After scheduling the pneumatic circuit, the user can generate the STereoLithography (STL) files for all logic gates and the connection hub with embedded air channels by pressing the “Save STL" button. Pressing the button opens a file explorer where you can specify the path where the STL files should be saved.

7.6.4 Detailed setup when 3D-printing the pneumatic circuit

The pneumatic computational circuit was printed by a Polyjet-based multi-material 3D printer (J735, Stratasys, USA). The printer setup was implemented in its corresponding slicer software (GrabCAD, Stratasys, USA). The connection hub of the pneumatic circuit was set to be printed with Agilus 30 (a rubber-like material with a quoted tensile strength of 2.1-2.6MPa and Shore hardness of 30A). The compliant part in each logic gate, shown as black in Figure 7.2, was set to be printed with Agilus30 as well. The rigid part in each logic gate, shown as white in Figure 7.2, was set to be printed with VeroYellow Vivid (a rigid plastic-like material with a quoted tensile strength of 50-65MPa and Shore hardness of 83-86D). The model finish was set to “Glossy", while the support strength was set to “Lite". Once the printing is finished, the pneumatic circuit was placed in a tank (GEMINI SSR-550) filled with chemical support removal solution (0.02 kg/L Sodium Hydroxide and 0.01 kg/L Sodium Metasilicate) for support removal.

7.6.5 Algorithm for finding the simplest circuit schematic

Algorithm 1 Converting Postfix Logic Expressions to a set of PneuSignal

```
for each character in postfix expressions do
    if character is an operand then
        if character is new then
            Create a new PneuSignal
            PneuSignal.value ← character
            PneuSignal.up ← new input port
            Push PneuSignal into stack
        else if character has been seen then
            Find the PneuSignal such that PneuSignal.value = character
            Push the PneuSignal found into stack
        end if
    else if character is an operator then
        old value ← The value of the last 1 or 2 PneuSignal in stack
        new value ← old value after operated by character
        if new value is new then
            Create a new gate
            The down of the last 1 or 2 PneuSignal in stack ← gate
            Pop the last 1 or 2 PneuSignal from stack
            Create a new PneuSignal
            PneuSignal.value ← new value
            PneuSignal.up ← gate
            Push PneuSignal into stack
        else if new value has been seen then
            Pop the last 1 or 2 PneuSignal from stack
            Find the PneuSignal such that PneuSignal.value = new value
            Push the PneuSignal found into stack
        end if
    end if
end for
```

7.6.6 Algorithm for finding all valid logic gate layout

Algorithm 2 Converting Postfix Logic Expressions to a set of PneuSignal

```
1: function BackTracking()
2:     if all logic gates placed in the workspace then
3:         Record the workspace, return
4:     end if
5:     if workspace is full then
6:         return
7:     end if
8:     for each element in the workspace do
9:         if element is available then
10:            if there is remaining AND gate to be placed then
11:                for each adjacent element which locates beside the element do
12:                    if adjacent element is available then
13:                        Place an AND gate at element and adjacent element
14:                        BackTracking()
15:                        Remove the AND gate from element and adjacent element
16:                    end if
17:                end for
18:            else if there is remaining OR gate to be placed then
19:                for each adjacent element which locates beside the element do
20:                    if adjacent element is available then
21:                        Place an OR gate at element and adjacent element
22:                        BackTracking()
23:                        Remove the OR gate from element and adjacent element
24:                    end if
25:                end for
26:            else if there is remaining NOT gate to be placed then
27:                Place a NOT gate at element
28:                BackTracking()
29:                Remove the NOT gate from element
30:            end if
31:        end if
32:    end for
33: end function
34: BackTracking()
```

8 Conclusions

The thesis covers our solutions to a series of research questions towards integrable pneumatic circuits for onboard computation and control of soft robots. Here we summarise the major research gaps identified through literature study, how our works fill the gaps, and the potential future directions opened up by our works.

As discussed in the literature review, many soft robots are still using traditional pneumatic systems which are bulky, heavy, and rigid. In many cases, the lack of more integrable control devices limits the compliance, mobility, and adaptability of soft robots. Therefore, the vision of this DPhil is to provide the soft robotics community with more simplified and integrable hardware that computes pneumatic signals and correspondingly controls soft pneumatic actuators. After investigating all state-of-the-art works in this field, including microfluidics, bistable silicone-casted valves, CFR-based circuits, 3D-printed circuitry, MR fluids regulator, hand-crafted pneumatic logic devices, and more, we believe that the major research gaps lie in the following aspects: (a) the time-consuming and labour-intensive fabrication of integrable, bistable valves for soft robots; (b) the lack of integrable, proportional valves that accurately modulate the pneumatic pressure in soft robots and; (c) the lack of a generalized guideline for soft roboticists to combine individual valves into pneumatic circuits performing desired computation onboard the soft

robots. To fill these gaps, we conducted five pieces of work, whose details are presented in Chapters 3 - 7.

Chapters 3 and 4 present our works to tackle the first research gap mentioned above, simplifying the fabrication of soft, bistable valves. Chapter 3 presents a 3D-printed, pneumatically-driven bistable valve. The work contributes towards both the onboard computation and onboard control of soft robots. Regarding computation, the bistable valve can be used as a memory device, storing a bit of binary information even after a power reset. Regarding control, the valve can regulate the airflow and therefore control pneumatic actuators with sufficient flowrate and pressure tolerance. By exploiting Multi-material 3D printing, we replaced the complex fabrication process which is the major limitation in previous works. In the work presented in Chapter 4, we enhanced the capability of our 3D-printed bistable valve regarding onboard control. By introducing a set of multi-channel modular units, the valve is now able to control multiple pneumatic actuators simultaneously. This significantly lowers the number of valves required to control multi-chamber soft robots, therefore reducing the system size, weight, cost, and energy consumption. Chapters 5 and 6 present our works to tackle the second research gap mentioned above, which is the lack of integrable proportional valves. Chapter 5 presents a novel proportional valve that exploits magnetorheological elastomer to achieve continuous airflow regulation. Apart from the analogue control capability, the advantages of our MRE valve include structural compliance, the integrability of soft robots, fast response, high durability, and low cost. To control soft robots with multiple soft pneumatic actuators, we also investigated how a large number of MRE valves can be packed into an array efficiently while ensuring their safe, steady and independent operation (see Chapter 6. To address the challenges regarding magnetic interference and overheating, we performed multi-physics FE simulations to find out the optimal layouts of the valve coils and the cooling chamber.

The work detailed in Chapter 7 addresses the last research gap mentioned above. It introduces a highly automated methodology enabling soft roboticists to utilize onboard pneumatic circuits for signal computation. We developed an open-source

software toolbox that automatically designs a 3D-printable pneumatic circuit to achieve a user-defined truth table while adhering to certain space constraints. As the first design automation toolbox in this field that generates fabrication-ready files directly, this work enhances the accessibility of pneumatic computational circuits and unlocks opportunities for embedding higher intelligence into entirely soft and untethered robots.

All works conducted during this DPhil together bring the soft robotics community a more streamlined methodology to achieve both onboard signal computation and pneumatic control. Regarding computation, this DPhil addresses both binary memory devices and digital computation circuits. Regarding control, both digital ON/OFF control and proportional control are addressed. All these functionalities are built upon 3D-printed or silicone structures, which are exactly the two main fabrication techniques used by soft robots. This guarantees that these devices can be integrated into the soft robots without sacrificing their weight, size, compliance, or fabrication complexity. The work in this DPhil not only meets the objective but also opens up several avenues for future development. Many of our works can be combined together to achieve more functionalities. For instance, it would be meaningful to include our 3D-printed bistable valve and multi-channel valves in our design automation toolbox, so that the generated pneumatic circuits not only perform digital computation but also non-volatile memory. Moreover, our MRE-based proportional valves can be combined into our digital computation circuits, so that the output pressures supplied to the soft pneumatic actuators are no longer limited to a binary manner. Lastly, as the community continues to develop new types of 3D-printed pneumatic circuit components, they can also be included in the design automation algorithm.

Another avenue for future development lies closely with the progress of material science and smart manufacturing. The 3D-printing materials used in this DPhil are far from perfect, marked by notable issues such as substantial ageing and high viscoelasticity. These properties significantly limit the performance of our pneumatic circuits, both in terms of computational speed and long-term durability. Therefore,

adapting our methodology with newer 3D printable materials that overcome these limitations would constitute a noteworthy breakthrough.

Appendices

A

List of Supporting Videos

- A video summarizing our 3D printed bistable valve (discussed in Chapter 3) can be found here: `https://youtu.be/40t8UxduZZ8`
- A video summarizing our 3D printed multi-channel valve (discussed in Chapter 4) can be found here: `https://youtu.be/WLF4muOTwRg`
- A video demonstrating our MRE valve (see Chapter 5) regulating airflow in an analogue manner can be found here: `https://youtu.be/talJvx7T-m8`
- A video showing the fabrication procedure of our MRE valve (see Chapter 5) can be found here: `https://youtu.be/LEyd6HjvUxc`
- A video showing the real-time pressure control of a soft pneumatic actuator via the MRE valve (see Chapter 5) can be found here: `https://youtu.be/q4G9t4Rnfnc`
- A video of our MRE valve array controlling multiple pneumatic actuators simultaneously is attached here: `https://youtu.be/FVkGagNZaFI`
- A userguide for our design automation toolbox for pneumatic circuits can be found here: `https://youtu.be/u6U-YVwS2gU`

- A video showing the 1:4 de-multiplexer circuit generated by our design automation toolbox is attached here: `https://youtu.be/YOqJNM9pI1c`

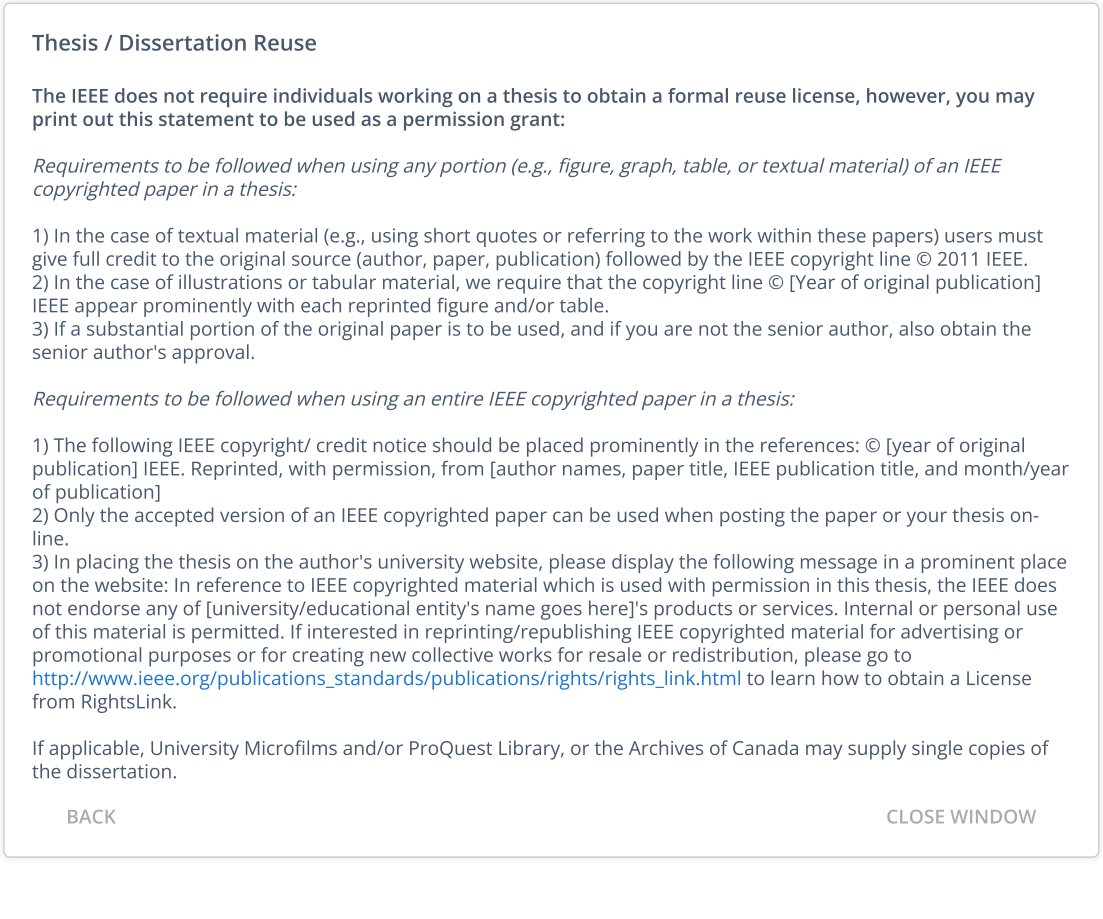
B

Copyright Permissions

The Literature Review chapter reuses figures from several published research articles. Here are the permissions for reusing those figures.

B.1 Permissions of IEEE papers

Here is the permission for papers published by IEEE.



Thesis / Dissertation Reuse

The IEEE does not require individuals working on a thesis to obtain a formal reuse license, however, you may print out this statement to be used as a permission grant:

Requirements to be followed when using any portion (e.g., figure, graph, table, or textual material) of an IEEE copyrighted paper in a thesis:

1) In the case of textual material (e.g., using short quotes or referring to the work within these papers) users must give full credit to the original source (author, paper, publication) followed by the IEEE copyright line © 2011 IEEE.
2) In the case of illustrations or tabular material, we require that the copyright line © [Year of original publication] IEEE appear prominently with each reprinted figure and/or table.
3) If a substantial portion of the original paper is to be used, and if you are not the senior author, also obtain the senior author's approval.

Requirements to be followed when using an entire IEEE copyrighted paper in a thesis:

1) The following IEEE copyright/ credit notice should be placed prominently in the references: © [year of original publication] IEEE. Reprinted, with permission, from [author names, paper title, IEEE publication title, and month/year of publication]
2) Only the accepted version of an IEEE copyrighted paper can be used when posting the paper or your thesis on-line.
3) In placing the thesis on the author's university website, please display the following message in a prominent place on the website: In reference to IEEE copyrighted material which is used with permission in this thesis, the IEEE does not endorse any of [university/educational entity's name goes here]'s products or services. Internal or personal use of this material is permitted. If interested in reprinting/republishing IEEE copyrighted material for advertising or promotional purposes or for creating new collective works for resale or redistribution, please go to http://www.ieee.org/publications_standards/publications/rights/rights_link.html to learn how to obtain a License from RightsLink.

If applicable, University Microfilms and/or ProQuest Library, or the Archives of Canada may supply single copies of the dissertation.

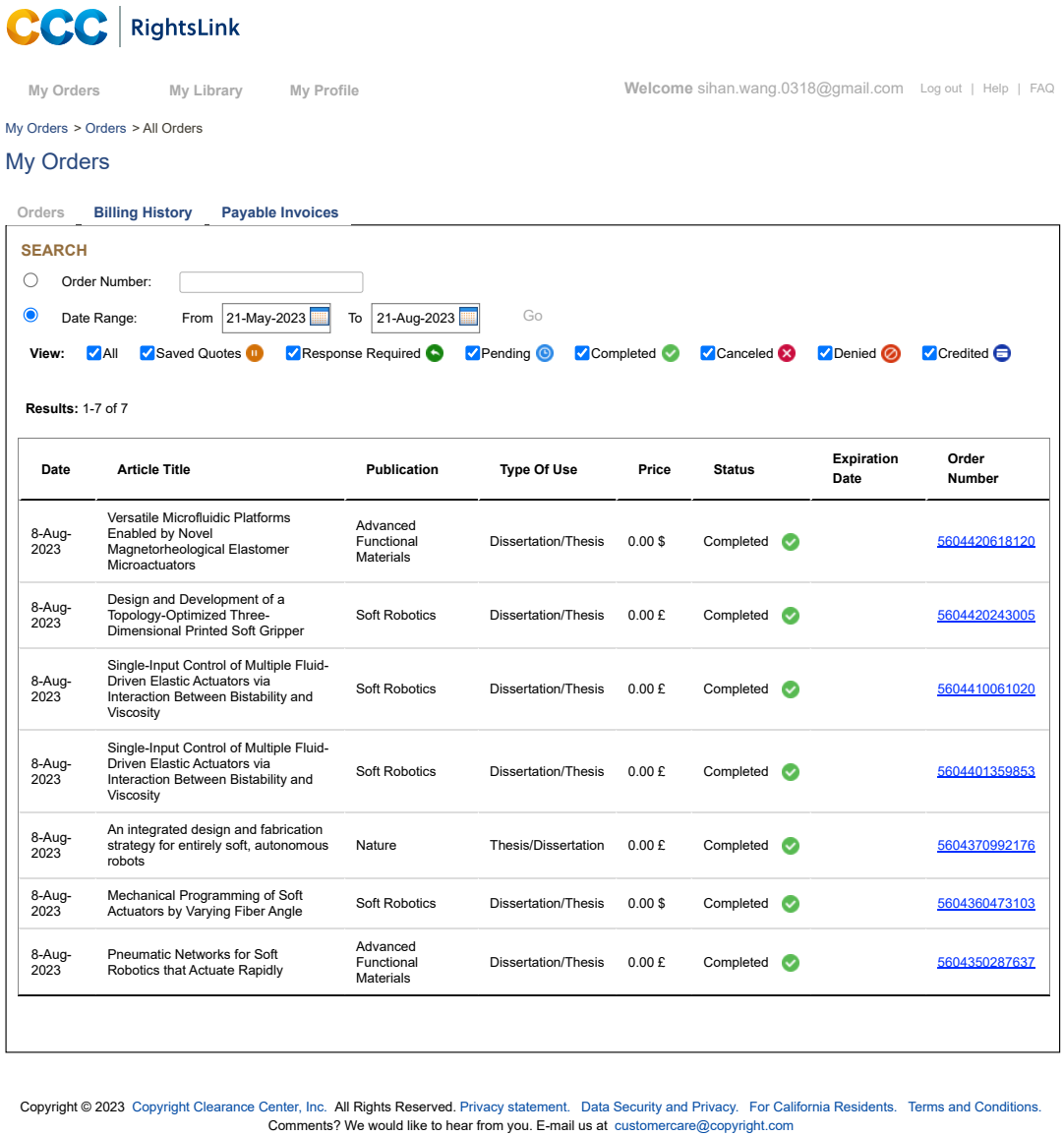
BACK CLOSE WINDOW

© 2023 Copyright - All Rights Reserved | Copyright Clearance Center, Inc. | Privacy statement | Data Security and Privacy | For California Residents | Terms and ConditionsComments? We would like to hear from you. E-mail us at customercare@copyright.com

Figure B.1: Permissions from IEEE for reusing figures for thesis,

B.2 Permissions of other papers

Here are the copyright permissions for other papers via RightsLink.



RightsLink

My Orders My Library My Profile Welcome sihan.wang.0318@gmail.com Log out | Help | FAQ

My Orders > Orders > All Orders

My Orders

Orders Billing History Payable Invoices

SEARCH

Order Number:

Date Range: From 21-May-2023 To 21-Aug-2023 Go

View: All Saved Quotes Response Required Pending Completed Canceled Denied Credited

Results: 1-7 of 7

Date	Article Title	Publication	Type Of Use	Price	Status	Expiration Date	Order Number
8-Aug-2023	Versatile Microfluidic Platforms Enabled by Novel Magnetorheological Elastomer Microactuators	Advanced Functional Materials	Dissertation/Thesis	0.00 $	Completed		5604420618120
8-Aug-2023	Design and Development of a Topology-Optimized Three-Dimensional Printed Soft Gripper	Soft Robotics	Dissertation/Thesis	0.00 £	Completed		5604420243005
8-Aug-2023	Single-Input Control of Multiple Fluid-Driven Elastic Actuators via Interaction Between Bistability and Viscosity	Soft Robotics	Dissertation/Thesis	0.00 £	Completed		5604410061020
8-Aug-2023	Single-Input Control of Multiple Fluid-Driven Elastic Actuators via Interaction Between Bistability and Viscosity	Soft Robotics	Dissertation/Thesis	0.00 £	Completed		5604401359853
8-Aug-2023	An integrated design and fabrication strategy for entirely soft, autonomous robots	Nature	Thesis/Dissertation	0.00 £	Completed		5604370992176
8-Aug-2023	Mechanical Programming of Soft Actuators by Varying Fiber Angle	Soft Robotics	Dissertation/Thesis	0.00 $	Completed		5604360473103
8-Aug-2023	Pneumatic Networks for Soft Robotics that Actuate Rapidly	Advanced Functional Materials	Dissertation/Thesis	0.00 £	Completed		5604350287637

Copyright © 2023 Copyright Clearance Center, Inc. All Rights Reserved. Privacy statement. Data Security and Privacy. For California Residents. Terms and Conditions.
Comments? We would like to hear from you. E-mail us at customercare@copyright.com

Figure B.2: Permissions for other papers via RightsLink

C

Theoretical Model for the Bistability of the 3D Printed Valve

In our work on the 3D-printed bistable valve, a theoretical model was used to prove the bistability of the conical shell and predict the critical pressure under different design parameters. The model is described in detail in our published paper attached in Section 3.5. Here we also attached the annotated Matlab code for building the theoretical model.

```
%% Define all variables and constants
syms S x d_theta p C buckling_y_displacement axial_load y_displacement V
E = 1.6499*1000000;
r = 0.004;
t = 0.001;
slope = 45;
H = 0.004;
R = r + H/tan(slope/180*pi);
L = sqrt(H^2+(R-r)^2);


%% This section is to find out when exactly buckling happens via Rayleigh-Ritz method
delta_L = L-sqrt((H-y_displacement)^2+(R-r)^2); % Find axial compressure via Pythagoras Theorem
I_buckling = (r+x/((R-r)/sqrt(H^2+(R-r)^2)))*d_theta*t^3/12; % Find the second moment of intertia along the beam
A_buckling = (r+x/((R-r)/sqrt(H^2+(R-r)^2)))*d_theta*t; % Find the cross-sectional area along the bean
w = C*(sin(pi*x/L)); % Assumed buckling shape, with unknow value of C
w_1st_derivative = diff(w,x); % find dw/dx
w_2nd_derivative = diff(w_1st_derivative,x); % find the second derivative of w
buckling_load = int(0.5*E*I_buckling*(w_2nd_derivative)^2,x,[0 L])/int(0.5*(w_1st_derivative)^2,x,[0 L]); %Finding the buckling load via Rayleigh-Ritz method
buckling_deformation = int(buckling_load/A_buckling/E,x,[0 L]); % Find the axial compression at buckling
buckling_y_displacement = solve(L-sqrt((H-buckling_y_displacement)^2+(R-r)^2) == buckling_deformation, buckling_y_displacement);% Find the vertical displacement at buckling


%% This section is to find out the elastic strain energy within the conical shell due to buckling
u_F = int(0.5*((diff(w,x))^2),x, [0 L]); % Relationship between local deflection and total axial compression
C = solve(u_F == delta_L, C); % solve the value of C from the total axial deflection
C = C(1);
w = C*(sin(pi*x/L)); % update the local deflection expression
w_1st_derivative = diff(w,x); % update dw/dx
w_2nd_derivative = diff(w_1st_derivative,x); % update d2w/dx2
energy_buckling = int(0.5*E*I_buckling*(w_2nd_derivative)^2, x, [0 L]);
energy_buckling = subs(energy_buckling,d_theta, 2*pi);  % Find the total strain energy due to buckling


%% This section is to find out the elastic strain energy within the conical shell due to axial compression.
axial_deformation = int(axial_load/A_buckling/E,x,[0 L]);
axial_load = solve(L-sqrt((H-y_displacement)^2+(R-r)^2) == axial_deformation, axial_load); %Find the axial lond induced by vertical dispalcement
energy_axial = int(0.5*E*A_buckling*(axial_load/A_buckling/E)^2,x,[0 L]);
energy_axial = subs(energy_axial,d_theta, 2*pi); % Find the total strain energy due
```

```
to axial compression


%% This section is to find out the driving pressure VS y-displacement
V = 1/3*pi*(R^2+r^2+R*r)*(H-y_displacement); % Internal volume of the conical shell
dV_dydisplacement =  diff(V,y_displacement); % 1st deravative of volume against y-displacement
p_buckling = diff(2*energy_buckling,y_displacement)/dV_dydisplacement; % driving pressure within the buckling range
p_axial = diff(2*energy_axial,y_displacement)/dV_dydisplacement; % driving pressure within the axial compression range


%% This section is for data visulization
clr = parula(10);
figure('Position', [300 300 600 400])
subplot(2,1,1);
fplot(y_displacement*1000-4, energy_axial,double([-0.001 buckling_y_displacement(1)]),'-', 'LineWidth',2,'Color',clr(2,:))
hold on
fplot(y_displacement*1000-4, energy_buckling,double([buckling_y_displacement(1) buckling_y_displacement(2)]),'-', 'LineWidth',2,'Color',clr(9,:))
hold on
fplot(y_displacement*1000-4, energy_axial,double([buckling_y_displacement(2) 0.009]),'-', 'LineWidth',2,'Color',clr(2,:))
grid on
box on
xlabel("Vertical Displacement h (mm)")
ylabel("Strain Energy (J)")
subplot(2,1,1,'FontSize', 12);

subplot(2,1,2);
fplot(y_displacement*1000-4, p_axial/1000,double([-0.001 buckling_y_displacement(1)]),'-', 'LineWidth',2,'Color',clr(2,:))
hold on
fplot(y_displacement*1000-4, p_buckling/1000,double([buckling_y_displacement(1) buckling_y_displacement(2)]),'-', 'LineWidth',2,'Color',clr(9,:))
hold on
fplot(y_displacement*1000-4, p_axial/1000,double([buckling_y_displacement(2) 0.009]),'-', 'LineWidth',2,'Color',clr(2,:))
grid on
box on
legend("Axial Deformation Phase","Buckling Phase",'FontSize', 12)
xlabel("Vertical Displacement h (mm)")
ylabel("Critical Pressure (kPa)")
subplot(2,1,2,'FontSize', 12);
```

D

PID Controllers for MRE Valves

In Chapter 5 we presented our MRE-based proportional valve and applied it for real-time flowrate and pressure control. The feedback control was achieved with a PID controller running on a microcontroller (Teensy 4.1). The gains of PID controllers were tuned via the “trial-and-error" method. The detailed setup and parameters of the PID controllers are attached below.

Table D.1: Setup of the PID controller used for flowrate control with “Only PID" control scheme.

Parameter	**Value (Units)**
Controller Input	flowrate error (mL/min)
Controller Output	PWM duty factor
Output Range	0 (fully OFF) to 255 (fully ON, 3A current)
Sampling rate	50 Hz
Bias	given by model
P Gain	0.06
I Gain	0.04
D Gain	0.005
Wind-up limit	±100

Table D.2: Setup of the PID controller used for flowrate control with “PID + Model" control scheme.

Parameter	**Value (Units)**
Controller Input	flowrate error (mL/min)
Controller Output	PWM duty factor
Output Range	0 (fully OFF) to 255 (fully ON)
Sampling rate	50 Hz
Bias	128
P Gain	0.02
I Gain	0.02
D Gain	0.005
Wind-up limit	±100

Table D.3: Setup of the PID controller used for pressure control.

Parameter	**Value (Units)**
Controller Input	pressure error (Pa)
Controller Output	PWM duty factor
Output Range	0 (fully OFF) to 255 (fully ON)
Sampling rate	200 Hz
Bias	128
P Gain	0.07
I Gain	0.001
D Gain	0.02
Wind-up limit	±100

References

[1] Carmel Majidi. "Soft robotics: a perspective—current trends and prospects for the future". In: *Soft robotics* 1.1 (2014), pp. 5–11.

[2] Chiwon Lee et al. "Soft robot review". In: *International Journal of Control, Automation and Systems* 15 (2017), pp. 3–15.

[3] Bobak Mosadegh et al. "Pneumatic networks for soft robotics that actuate rapidly". In: *Advanced functional materials* 24.15 (2014), pp. 2163–2170.

[4] Yuan-Fang Zhang et al. "Fast-response, stiffness-tunable soft actuator by hybrid multimaterial 3D printing". In: *Advanced Functional Materials* 29.15 (2019), p. 1806698.

[5] Ali Zolfagharian et al. "Evolution of 3D printed soft actuators". In: *Sensors and Actuators A: Physical* 250 (2016), pp. 258–272.

[6] Richard Suphapol Diteesawat et al. "High strength bubble artificial muscles for walking assistance". In: *2018 IEEE International Conference on Soft Robotics (RoboSoft)*. IEEE. 2018, pp. 388–393.

[7] Aslan Miriyev, Kenneth Stack, and Hod Lipson. "Soft material for soft actuators". In: *Nature communications* 8.1 (2017), p. 596.

[8] Philipp Rothemund et al. "A soft, bistable valve for autonomous control of soft actuators". In: *Science Robotics* 3.16 (2018), eaar7986.

[9] Panagiotis Polygerinos et al. "Soft robotics: Review of fluid-driven intrinsically soft devices; manufacturing, sensing, control, and applications in human-robot interaction". In: *Advanced Engineering Materials* 19.12 (2017), p. 1700016.

[10] Rafsan Al Shafatul Islam Subad, Liam B Cross, and Kihan Park. "Soft Robotic Hands and Tactile Sensors for Underwater Robotics". In: *Applied Mechanics* 2.2 (2021), pp. 356–382.

[11] Thomas George Thuruthel et al. "Control strategies for soft robotic manipulators: A survey". In: *Soft robotics* 5.2 (2018), pp. 149–163.

[12] George M Whitesides. "Soft robotics". In: *Angewandte Chemie International Edition* 57.16 (2018), pp. 4258–4273.

[13] James Walker et al. "Soft robotics: A review of recent developments of pneumatic soft actuators". In: *Actuators*. Vol. 9. 1. MDPI. 2020, p. 3.

[14] Matheus S Xavier et al. "Soft pneumatic actuators: A review of design, fabrication, modeling, sensing, control and applications". In: *IEEE Access* 10 (2022), pp. 59442–59485.

[15] Hang Su et al. "Pneumatic soft robots: Challenges and benefits". In: *Actuators*. Vol. 11. 3. MDPI. 2022, p. 92.

[16] Yao Yao, Liang He, and Perla Maiolino. "A simulation-based toolbox to expedite the digital design of bellow soft pneumatic actuators". In: *2022 IEEE 5th International Conference on Soft Robotics (RoboSoft)*. IEEE. 2022, pp. 29–34.

[17] URL: `https://softroboticstoolkit.com/book/pneunets-variation-geometry`.

[18] Hao Jiang et al. "Design, control, and applications of a soft robotic arm". In: *arXiv preprint arXiv:2007.04047* (2020).

[19] Lisen Ge et al. "A digital light processing 3D printer for fast and high-precision fabrication of soft pneumatic actuators". In: *Sensors and Actuators A: Physical* 273 (2018), pp. 285–292.

[20] Kevin C Galloway et al. "Mechanically programmable bend radius for fiber-reinforced soft actuators". In: *2013 16th International Conference on Advanced Robotics (ICAR)*. IEEE. 2013, pp. 1–6.

[21] Fionnuala Connolly et al. "Mechanical programming of soft actuators by varying fiber angle". In: *Soft Robotics* 2.1 (2015), pp. 26–32.

[22] Bertrand Tondu. "Modelling of the McKibben artificial muscle: A review". In: *Journal of Intelligent Material Systems and Structures* 23.3 (2012), pp. 225–253.

[23] Joran W Booth et al. "An addressable pneumatic regulator for distributed control of soft robots". In: *2018 IEEE International Conference on Soft Robotics (RoboSoft)*. IEEE. 2018, pp. 25–30.

[24] Yingjun Tian et al. "OpenPneu: Compact platform for pneumatic actuation with multi-channels". In: *arXiv preprint arXiv:2209.11318* (2022).

[25] Ali Shtarbanov. "FlowIO development platform–The pneumatic "raspberry pi" for soft robotics". In: *Extended abstracts of the 2021 CHI conference on human factors in computing systems*. 2021, pp. 1–6.

[26] Taylor R Young et al. "A control and drive system for pneumatic soft robots: Pneusord". In: *2021 IEEE/RSJ International Conference on Intelligent Robots and Systems (IROS)*. IEEE. 2021, pp. 2822–2829.

[27] Jialei Shi et al. "Characterisation and control platform for pneumatically driven soft robots: Design and applications". In: *2023 IEEE International Conference on Soft Robotics (RoboSoft)*. IEEE. 2023, pp. 1–8.

[28] T TolleyMichael et al. "A resilient, untethered soft robot". In: *Soft robotics* (2014).

[29] Kevin McDonald and Tommaso Ranzani. "Hardware methods for onboard control of fluidically actuated soft robots". In: *Frontiers in Robotics and AI* (2021), p. 266.

[30] Andrew D Marchese, Cagdas D Onal, and Daniela Rus. "Autonomous soft robotic fish capable of escape maneuvers using fluidic elastomer actuators". In: *Soft robotics* 1.1 (2014), pp. 75–87.

[31] Tom Kalisky et al. "Differential pressure control of 3D printed soft fluidic actuators". In: *2017 IEEE/RSJ International Conference on Intelligent Robots and Systems (IROS)*. IEEE. 2017, pp. 6207–6213.

[32] Bas Wijnen et al. "Open-source syringe pump library". In: *PloS one* 9.9 (2014), e107216.

[33] Matheus S Xavier, Andrew J Fleming, and Yuen K Yong. "Image-guided locomotion of a pneumatic-driven peristaltic soft robot". In: *2019 IEEE International Conference on Robotics and Biomimetics (ROBIO)*. IEEE. 2019, pp. 2269–2274.

[34] Wenye Ouyang et al. "A Modular Soft Robotic Arm with Embedded Tactile Sensors for Proprioception". In: *2022 IEEE 5th International Conference on Soft Robotics (RoboSoft)*. IEEE. 2022, pp. 919–924.

[35] Shadab Zaidi et al. "Actuation technologies for soft robot grippers and manipulators: A review". In: *Current Robotics Reports* 2.3 (2021), pp. 355–369.

[36] Zhang Xiang et al. "Design and experimental validation of a cable-driven continuum manipulator and soft gripper". In: *2019 IEEE International Conference on Robotics and Biomimetics (ROBIO)*. IEEE. 2019, pp. 1965–1968.

[37] Mingfang Liu et al. "A novel design of shape-memory alloy-based soft robotic gripper with variable stiffness". In: *International journal of advanced robotic systems* 17.1 (2020), p. 1729881420907813.

[38] Liang Xu and Guoying Gu. "Bioinspired Venus flytrap: A dielectric elastomer actuated soft gripper". In: *2017 24th International Conference on Mechatronics and Machine Vision in Practice (M2VIP)*. IEEE. 2017, pp. 1–3.

[39] DI Labs. *Soft Robotics Food Automation Solutions Combing 3D vision, artificial intelligence and soft grasping*. July 2023. URL: `https://www.softroboticsinc.com/`.

[40] Festo. *Bionicsoftarm*. May 2023. URL: `https://www.festo.com/gb/en/e/about-festo/research-and-development/bionic-learning-network/highlights-from-2018-to-2021/bionicsoftarm-id_68209/`.

[41] Yufei Hao et al. "Universal soft pneumatic robotic gripper with variable effective length". In: *2016 35th Chinese control conference (CCC)*. IEEE. 2016, pp. 6109–6114.

[42] Guoliang Zhong, Yangdong Hou, and Weiqiang Dou. "A soft pneumatic dexterous gripper with convertible grasping modes". In: *International Journal of Mechanical Sciences* 153 (2019), pp. 445–456.

[43] Yanqiong Fei, Jiangbei Wang, and Wu Pang. "A novel fabric-based versatile and stiffness-tunable soft gripper integrating soft pneumatic fingers and wrist". In: *Soft robotics* 6.1 (2019), pp. 1–20.

[44] Tomoyuki Nakamura and Hideyuki Tsukagoshi. "Soft pneumatic manipulator capable of sliding under the human body and its application to preventing bedsores". In: *2018 IEEE/ASME International Conference on Advanced Intelligent Mechatronics (AIM)*. IEEE. 2018, pp. 956–961.

[45] Rei Hisatomi et al. "Development of forceps manipulator using pneumatic soft actuator for a bending joint of forceps tip". In: *2019 IEEE/SICE International Symposium on System Integration (SII)*. IEEE. 2019, pp. 695–700.

[46] Iris De Falco, Matteo Cianchetti, and Arianna Menciassi. "A soft multi-module manipulator with variable stiffness for minimally invasive surgery". In: *Bioinspiration & biomimetics* 12.5 (2017), p. 056008.

[47] Dylan Drotman et al. “3D printed soft actuators for a legged robot capable of navigating unstructured terrain”. In: *2017 IEEE International Conference on Robotics and Automation (ICRA)*. IEEE. 2017, pp. 5532–5538.

[48] Yichao Tang et al. “Leveraging elastic instabilities for amplified performance: Spine-inspired high-speed and high-force soft robots”. In: *Science advances* 6.19 (2020), eaaz6912.

[49] Robert F Shepherd et al. “Multigait soft robot”. In: *Proceedings of the national academy of sciences* 108.51 (2011), pp. 20400–20403.

[50] Aniket Joshi, Adwait Kulkarni, and Yonas Tadesse. “FludoJelly: Experimental study on jellyfish-like soft robot enabled by soft pneumatic composite (SPC)”. In: *Robotics* 8.3 (2019), p. 56.

[51] Suranga Seneviratne et al. “A survey of wearable devices and challenges”. In: *IEEE Communications Surveys & Tutorials* 19.4 (2017), pp. 2573–2620.

[52] HaptX. *Haptic Gloves G1 - Gloves for virtual reality and robotics | HaptX — haptx.com*. `https://haptx.com/`. [Accessed 26-07-2023]. 2023.

[53] Meta. *Inside Reality Labs Research: Meet the team that’s working to bring touch to the digital world — tech.facebook.com*. `https://tech.facebook.com/reality-labs/2021/11/inside-reality-labs-meet-the-team-thats-bringing-touch-to-the-digital-world/`. [Accessed 26-07-2023]. 2023.

[54] Panagiotis Polygerinos et al. “Towards a soft pneumatic glove for hand rehabilitation”. In: *2013 IEEE/RSJ International Conference on Intelligent Robots and Systems*. IEEE. 2013, pp. 1512–1517.

[55] Xinbo Chen et al. “Development of a wearable upper limb rehabilitation robot based on reinforced soft pneumatic actuators”. In: *Chinese Journal of Mechanical Engineering* 35.1 (2022), p. 83.

[56] Hong Kai Yap et al. “A soft exoskeleton for hand assistive and rehabilitation application using pneumatic actuators with variable stiffness”. In: *2015 IEEE international conference on robotics and automation (ICRA)*. IEEE. 2015, pp. 4967–4972.

[57] Nikolaos G Tsagarakis and Darwin G Caldwell. “Development and control of a ‘soft-actuated’exoskeleton for use in physiotherapy and training”. In: *Autonomous Robots* 15 (2003), pp. 21–33.

[58] Michael Wehner et al. “An integrated design and fabrication strategy for entirely soft, autonomous robots”. In: *nature* 536.7617 (2016), pp. 451–455.

[59] Elizabeth Gallardo Hevia, Louis De La Rochefoucauld, and Robert J Wood. “Towards a microfluidic microcontroller circuit library for soft robots”. In: *2022 International Conference on Robotics and Automation (ICRA)*. IEEE. 2022, pp. 7138–7144.

[60] Bruce K Gale et al. “A review of current methods in microfluidic device fabrication and future commercialization prospects”. In: *Inventions* 3.3 (2018), p. 60.

[61] Manu Prakash and Neil Gershenfeld. “Microfluidic bubble logic”. In: *Science* 315.5813 (2007), pp. 832–835.

[62] Darwin R Reyes et al. “Glow discharge in microfluidic chips for visible analog computing”. In: *Lab on a Chip* 2.2 (2002), pp. 113–116.

[63] Younan Xia and George M Whitesides. “Soft lithography”. In: *Annual review of materials science* 28.1 (1998), pp. 153–184.

[64] Joshua D Tice, Adam D Lyon, and Rustem F Ismagilov. “Effects of viscosity on droplet formation and mixing in microfluidic channels”. In: *Analytica chimica acta* 507.1 (2004), pp. 73–77.

[65] Daniel J Preston et al. “Digital logic for soft devices”. In: *Proceedings of the National Academy of Sciences* 116.16 (2019), pp. 7750–7759.

[66] Kai Luo et al. “Soft kink valves”. In: *Journal of the Mechanics and Physics of Solids* 131 (2019), pp. 230–239.

[67] Markus P Nemitz et al. “Soft non-volatile memory for non-electronic information storage in soft robots”. In: *2020 3rd IEEE International Conference on Soft Robotics (RoboSoft)*. IEEE. 2020, pp. 7–12.

[68] Dylan Drotman et al. “Electronics-free pneumatic circuits for controlling soft-legged robots”. In: *Science Robotics* 6.51 (2021), eaay2627.

[69] Joshua D Hubbard et al. “Fully 3D-printed soft robots with integrated fluidic circuitry”. In: *Science Advances* 7.29 (2021), eabe5257.

[70] Nicholas W Bartlett et al. “A 3D-printed, functionally graded soft robot powered by combustion”. In: *Science* 349.6244 (2015), pp. 161–165.

[71] Erina B Joyee and Yayue Pan. “A fully three-dimensional printed inchworm-inspired soft robot with magnetic actuation”. In: *Soft robotics* 6.3 (2019), pp. 333–345.

[72] RD Sochol et al. “3D printed microfluidic circuitry via multijet-based additive manufacturing”. In: *Lab on a Chip* 16.4 (2016), pp. 668–678.

[73] Jovanna A Tracz et al. “Tube-Balloon Logic for the Exploration of Fluidic Control Elements”. In: *IEEE Robotics and Automation Letters* 7.2 (2022), pp. 5483–5488.

[74] Colter J Decker et al. “Programmable soft valves for digital and analog control”. In: *Proceedings of the National Academy of Sciences* 119.40 (2022), e2205922119.

[75] Kevin J McDonald et al. “Modulation of magnetorheological fluid flow in soft robots using electropermanent magnets”. In: *IEEE Robotics and Automation Letters* 7.2 (2022), pp. 3914–3921.

[76] Kevin McDonald et al. “Magnetorheological fluid-based flow control for soft robots”. In: *Advanced Intelligent Systems* 2.11 (2020), p. 2000139.

[77] T Leps et al. “A low-power, jamming, magnetorheological valve using electropermanent magnets suitable for distributed control in soft robots”. In: *Smart Materials and Structures* 29.10 (2020), p. 105025.

[78] Siyi Xu et al. “A dynamic electrically driven soft valve for control of soft hydraulic actuators”. In: *Proceedings of the National Academy of Sciences* 118.34 (2021).

[79] Siyi Xu et al. “A compact DEA-based soft peristaltic pump for power and control of fluidic robots”. In: *Science Robotics* 8.79 (2023), eadd4649.

[80] Lucas C van Laake et al. “A fluidic relaxation oscillator for reprogrammable sequential actuation in soft robots”. In: *Matter* 5.9 (2022), pp. 2898–2917.

[81] Eran Ben-Haim et al. “Single-input control of multiple fluid-driven elastic actuators via interaction between bistability and viscosity”. In: *Soft robotics* 7.2 (2020), pp. 259–265.

[82] Benjamin Gorissen et al. “Hardware sequencing of inflatable nonlinear actuators for autonomous soft robots”. In: *Advanced Materials* 31.3 (2019), p. 1804598.

[83] Sihan Wang, Liang He, and Perla Maiolino. “Design and characterization of a 3D-printed pneumatically-driven bistable valve with tunable characteristics”. In: *IEEE Robotics and Automation Letters* 7.1 (2021), pp. 112–119.

[84] Sihan Wang, Liang He, and Perla Maiolino. “A Modular Approach to Design Multi-channel Bistable Valves for Integrated Pneumatically-driven Soft Robots via 3D-printing”. In: *IEEE Robotics and Automation Letters* (2022).

[85] Sihan Wang et al. “A Magnetorheological Elastomer-Based Proportional Valve for Soft Pneumatic Actuators”. In: *Advanced Intelligent Systems* (2022), p. 2200238.

[86] Takuya Umedachi and Barry A Trimmer. “Design of a 3D-printed soft robot with posture and steering control”. In: *2014 IEEE International Conference on Robotics and Automation (ICRA)*. IEEE. 2014, pp. 2874–2879.

[87] Hongying Zhang et al. “Design and development of a topology-optimized three-dimensional printed soft gripper”. In: *Soft robotics* 5.5 (2018), pp. 650–661.

[88] Oliver Shorthose et al. “Design of a 3D-Printed Soft Robotic Hand with Integrated Distributed Tactile Sensing”. In: *IEEE Robotics and Automation Letters* 7.2 (2022), pp. 3945–3952.

[89] Viacheslav Slesarenko and Stephan Rudykh. “Towards mechanical characterization of soft digital materials for multimaterial 3D-printing”. In: *International Journal of Engineering Science* 123 (2018), pp. 62–72.

[90] Elizabeth H Childs et al. “Additive assembly for PolyJet-based multi-material 3D printed microfluidics”. In: *Journal of Microelectromechanical Systems* 29.5 (2020), pp. 1094–1096.

[91] Parth Patpatiya et al. “A review on polyjet 3D printing of polymers and multi-material structures”. In: *Proceedings of the Institution of Mechanical Engineers, Part C: Journal of Mechanical Engineering Science* 236.14 (2022), pp. 7899–7926.

[92] Yun Lu Tee et al. “PolyJet 3D printing of composite materials: experimental and modelling approach”. In: *Jom* 72 (2020), pp. 1105–1117.

[93] Jahan Zeb Gul et al. “3D printing for soft robotics–a review”. In: *Science and technology of advanced materials* 19.1 (2018), pp. 243–262.

[94] Jerzy Bochnia. “A Study of the Mechanical Properties of Naturally Aged Photopolymers Printed Using the PJM Technology”. In: *Materials* 16.1 (2023), p. 400.

[95] Jacob P Moore and Christopher B Williams. “Fatigue properties of parts printed by PolyJet material jetting”. In: *Rapid Prototyping Journal* 21.6 (2015), pp. 675–685.

[96] Adam S Verga et al. "Nonlinear Viscoelastic Properties of 3D-Printed Tissue Mimicking Materials and Metrics to Determine the Best Printed Material Match to Tissue Mechanical Behavior". In: *Frontiers in Mechanical Engineering* 8 (2022), p. 862375.

[97] Anil K Bastola and Mokarram Hossain. "A review on magneto-mechanical characterizations of magnetorheological elastomers". In: *Composites Part B: Engineering* 200 (2020), p. 108348.

[98] Shi-Yang Tang et al. "Versatile microfluidic platforms enabled by novel magnetorheological elastomer microactuators". In: *Advanced Functional Materials* 28.8 (2018), p. 1705484.

[99] Shunta Kashima, Fumikazu Miyasaka, and Katsuhiro Hirata. "Novel soft actuator using magnetorheological elastomer". In: *IEEE Transactions on magnetics* 48.4 (2012), pp. 1649–1652.

[100] Peizhi Zhang et al. "EPM–MRE: Electropermanent magnet–magnetorheological elastomer for soft actuation system and its application to robotic grasping". In: *IEEE Robotics and Automation Letters* 6.4 (2021), pp. 8181–8188.

[101] John M Ginder et al. "Magnetorheological elastomers: properties and applications". In: *Smart Structures and Materials 1999: Smart Materials Technologies*. Vol. 3675. SPIE. 1999, pp. 131–138.

[102] Yancheng Li et al. "A state-of-the-art review on magnetorheological elastomer devices". In: *Smart materials and structures* 23.12 (2014), p. 123001.

[103] Valery P Mikhailov and Alexey M Bazinenkov. "Active vibration isolation platform on base of magnetorheological elastomers". In: *Journal of Magnetism and Magnetic Materials* 431 (2017), pp. 266–268.

[104] Ryan L Harne, Zhangxian Deng, and Marcelo J Dapino. "Adaptive magnetoelastic metamaterials: A new class of magnetorheological elastomers". In: *Journal of Intelligent Material Systems and Structures* 29.2 (2018), pp. 265–278.

[105] Nicholas Bira, Pallavi Dhagat, and Joseph R Davidson. "A review of magnetic elastomers and their role in soft robotics". In: *Frontiers in Robotics and AI* 7 (2020), p. 588391.

[106] Taixiang Liu and Yangguang Xu. "Magnetorheological elastomers: Materials and applications". In: *Smart and functional soft materials* 5 (2019).

[107] Hossein Vatandoost et al. "Dynamic characterization of isotropic and anisotropic magnetorheological elastomers in the oscillatory squeeze mode superimposed on large static pre-strain". In: *Composites Part B: Engineering* 182 (2020), p. 107648.

[108] Holger Böse, Raman Rabindranath, and Johannes Ehrlich. "Soft magnetorheological elastomers as new actuators for valves". In: *Journal of Intelligent Material Systems and Structures* 23.9 (2012), pp. 989–994.

[109] Mohammad Fatahillah, Namsoo Oh, and Hugo Rodrigue. "A novel soft bending actuator using combined positive and negative pressures". In: *Frontiers in Bioengineering and Biotechnology* 8 (2020), p. 472.

[110] Shoue Chen et al. "Soft crawling robots: design, actuation, and locomotion". In: *Advanced Materials Technologies* 5.2 (2020), p. 1900837.

[111] Clark B Teeple et al. "Multi-segment soft robotic fingers enable robust precision grasping". In: *The International Journal of Robotics Research* 39.14 (2020), pp. 1647–1667.

[112] Johannes F Elfferich, Dimitra Dodou, and Cosimo Della Santina. "Soft robotic grippers for crop handling or harvesting: A review". In: *IEEE Access* 10 (2022), pp. 75428–75443.

[113] Alexander Yin et al. "Combining locomotion and grasping functionalities in soft robots". In: *Advanced Intelligent Systems* 1.8 (2019), p. 1900089.

[114] Sunkyu Kong et al. "An investigation of electromagnetic radiated emission and interference from multi-coil wireless power transfer systems using resonant magnetic field coupling". In: *IEEE Transactions on Microwave Theory and Techniques* 63.3 (2015), pp. 833–846.

[115] Giovanni Spiezia et al. "Automatic test bench for measurement of magnetic interference on LVDTs". In: *IEEE Transactions on Instrumentation and Measurement* 60.5 (2011), pp. 1802–1810.

[116] Jun Fu, Zhiwen Ning, and Yang Chang. "Active Compensation Method for Strong Magnetic Interference of MEMS Electronic Compass". In: *IEEE Access* 9 (2021), pp. 48860–48872.

[117] Jun Man et al. "Novel high-speed electromagnetic actuator with permanent-magnet shielding for high-pressure applications". In: *IEEE Transactions on Magnetics* 46.12 (2010), pp. 4030–4033.

[118] Hongseok Kim et al. "Design of magnetic shielding for reduction of magnetic near field from wireless power transfer system for electric vehicle". In: *2014 International Symposium on Electromagnetic Compatibility*. IEEE. 2014, pp. 53–58.

[119] AJE Raaijmakers et al. "Design of a radiative surface coil array element at 7 T: the single-side adapted dipole antenna". In: *Magnetic resonance in medicine* 66.5 (2011), pp. 1488–1497.

[120] Alessandro Lampasi et al. "Final design of the switching network units for the JT-60SA central solenoid". In: *Fusion Engineering and Design* 89.4 (2014), pp. 342–348.

[121] Hassan Azarkish et al. "Self-adaptive microvalve array for energy efficient fluidic cooling in microelectronic systems". In: *2017 16th IEEE Intersociety Conference on Thermal and Thermomechanical Phenomena in Electronic Systems (ITherm)*. IEEE. 2017, pp. 522–529.

[122] L Wang et al. "The helium cooling system and cold mass support system for the MICE coupling solenoid". In: *IEEE Transactions on Applied Superconductivity* 18.2 (2008), pp. 941–944.

[123] VA Kurganov. "Heat transfer coefficient". In: *Thermopedia*. Begel House Inc., 2011.

[124] Festo. *FluidDraw P6*. 2023. URL: `https://www.festo.com/gb/en/app/fluiddraw-p6.html` (visited on 06/27/2023).

[125] Guyue Huang et al. "Machine learning for electronic design automation: A survey". In: *ACM Transactions on Design Automation of Electronic Systems (TODAES)* 26.5 (2021), pp. 1–46.

[126] Daniel Grissom et al. "An open-source compiler and PCB synthesis tool for digital microfluidic biochips". In: *INTEGRATION, the VLSI journal* 51 (2015), pp. 169–193.

[127] Alec AK Nielsen et al. "Genetic circuit design automation". In: *Science* 352.6281 (2016), aac7341.

[128] SMC UK. *Pneumatic circuits drawing*. SMC UK. 2023. URL: https://www.smc.eu/en-gb/products/engineering-tools/pneumatic_circuits_drawing.

[129] Festo. *FluidSIM*. 2023. URL: https://www.festo.com/ae/en/e/technical-education/digital-learning/virtual-simulation-and-modelling/fluidsim-id_1663056/ (visited on 06/27/2023).

[130] Savita V Kendre et al. "The Soft Compiler: A Web-Based Tool for the Design of Modular Pneumatic Circuits for Soft Robots". In: *IEEE Robotics and Automation Letters* 7.3 (2022), pp. 6060–6066.

[131] Philippe Codognet, François Fages, and Thierry Sola. "A Metalevel Compiler of CLP (FD) and Its Combination with Intelligent Backtracking." In: *WCLP*. Citeseer. 1991, pp. 437–456.

[132] Amir Hossein Ashouri et al. "Predictive modeling methodology for compiler phase-ordering". In: *Proceedings of the 7th workshop on parallel programming and run-time management techniques for many-core architectures and the 5th workshop on design tools and architectures for multicore embedded computing platforms*. 2016, pp. 7–12.

[133] János Pach and Micha Sharir. "On vertical visibility in arrangements of segments and the queue size in the Bentley-Ottmann line sweeping algorithm". In: *SIAM Journal on Computing* 20.3 (1991), pp. 460–470.